Synthesis and characterisation of niobium doped TiO_2 semiconducting materials

---

This thesis is submitted in partial fulfilment of the requirements for the Degree of Doctor of Philosophy

Aleksandra J. Gardecka

2016

Supervised by: Professor Ivan P. Parkin, Professor Gopinathan Sankar and Doctor Gregory Goh

Declaration

I, Aleksandra Gardecka confirm that the work presented in this thesis is my own. Where information has been derived from other sources, I confirm that this has been indicated in this thesis.

Abstract

This thesis focuses on synthesis and characterisation of niobium doped TiO_2 materials as thin films, nanorods and nanopowders and their applications as windows coatings, transparent conducting oxide (TCO) materials and anodes for lithium ion batteries.

The first chapter gives an introduction to the TCO materials, TiO_2 characterisation, application and doping methods. It also contains a brief description of the synthesis and analysis methods, used in the thesis.

The second chapter describes the niobium doped anatase form of TiO_2 thin films deposited *via* aerosol assisted chemical vapour deposition (AACVD) on silica coated glass. The as-deposited films were blue, largely transparent in the visible region, reflective in the IR region and electrically conductive. The doping progress and phase segregation propagation were analysed using high resolution transmission electron spectroscopy (HR-TEM) and X-ray absorption spectroscopy (XAS).

In the third chapter, AACVD deposition of TiO_2 and niobium doped TiO_2 over a fluorine doped tin oxide (FTO) substrate in order to achieve the rutile form of TiO_2 by templating the lattice structure is described. Depending on the synthesis precursors and temperatures used, the obtained films consisted of one to four different parts, varying from a metallic continuous tin film, mixture of rutile TiO_2, FTO and metallic tin to layered FTO- anatase TiO_2 thin films.

In order to increase the photocatalytic properties of the anatase thin films described in the second chapter a silver layer was sputtered prior to the AACVD deposition of both pristine and niobium doped TiO_2 thin films. While the Ag:TiO_2 thin films remained electrically insulating, the Ag:$NbTiO_2$ thin film displayed electrical conductivity. For both films the rate of photo degradation of Resazurin dye was lower than that of a Pilkington Activ™ standard.

The fifth chapter describes the hydrothermal synthesis method of both rutile and anatase TiO_2 powders, by changing the pH of the process. The successful substitutional doping of niobium into the TiO_2 lattice was obtained at temperatures as low as 180 °C. The differences in phase segregation in rutile and anatase are described.

Chapter six describes the hydrothermal synthesis of the Nb:TiO_2 rutile free-standing film, 10 μm thick, with rutile rods creating a stable and merged structure, that maintains flexibility and can be shaped within a two minute exposure window to the air.

Acknowledgements

I owe my thanks to Prof Ivan Parkin, my primary supervisor for his patience, guidance, knowledge, advice and enormous amounts of support I have received throughout of these years, both personally and during my attachment in Singapore. Secondly, to Prof Gopinathan Sankar for his time during beam times, his Singaporean visits, and his patience during XAFS explanations. Thirdly, to Dr Gregory Goh Kia Liang for supervision during my attachment in IMRE. I would also like to take this opportunity to thank Dr Andreas Kafizas for accepting a role of a postdoc on this project. Thank you.

No chemistry and material science present in this thesis would be possible without characterisation, therefore I would like to thank the technical support of UCL and IMRE for their time taken in teaching me how to perform the relevant analysis. My special thanks go to Lai Doreen for her exceptional kindness in explaining me what I did wrong and Teo Siew Lang for spending hours with me analysing my samples. I also thank Diamond Light Source for the provision of beam time, Dr Gianntonio Cibin for his assistance with the measurements, Dr Husn-Ubadya Islam for teaching me Athena and Artemis, Dr Penny Carmichael for Casa XPS tutorial and scanning my chapters and Carlos Sotelo-Vazquez for all the help with running XPS.

This thesis wouldn't have been possible without my friends and co-workers, both from UCL and IMRE. You have earned my gratitude for your friendship and help in the scientific field.

The road through my PhD turned into the great adventure thanks to Zarrin Ansari, Dr Richard Chadwick, Dr Nuruzzaman Noor, Shereif Mujahed, Marta Targosz, Dr Sacha Noimark (also for printing, binding and submitting my thesis (sic!), Andrew Breeson, Samwise Fishlock, Mechtild Lübke, Ceilidh Armer (also big thanks for proof reading),

Fiorella Amadei, Will Grimes, Dr Joe Manzi, Dr Christina Pang, Dr Nadia Karim to name few.

This thesis is dedicated to my family, who has supported me through my whole scientific journey, and who do their best to understand what this book is about.

List of Figures

List of Tables

List of Abbreviations

AACVD- aerosol assisted chemical vapour deposition

XRD- X-ray diffraction

XPS- X-ray photoelectron spectroscopy

SEM- scanning electron microscopy

TEM- transmission electron microscopy

EDX- energy dispersive X-ray spectroscopy

XAS- X-ray absorption spectroscopy

EXAFS- extended X-ray absorption fine structure

XANES- X-ray absorption near-edge structure

LCF- linear combination fit

TCO- transparent conductive oxide

UV-vis- ultraviolet- visible

Nb:TiO_2- niobium doped TiO_2

FTO- fluorine doped tin oxide

ITO- indium tin oxide

GZO- gallium doped zinc oxide

AZO- aluminium doped zinc oxide

$Ti(OEt)_4$- titanium (IV) ethoxide

$Ti(OBu)_4$- titanium (IV) buthoxide

$Nb(OEt)_5$- niobium (V) ethoxide

MeOH- methanol

EtOH- ethanol

iPrOH- propan-2-ol, isopropanol

NPs- nanoparticles

FQE- formal quantum efficiency

FQY- formal quantum yield

1. Introduction

1.1. Transparent conducting materials

Transparent conductors (TCs), including transparent conducting oxides (TCOs) are materials which find use in the solar cells, energy storage devices, water splitting technology, opto-electronics and "smart" windows coatings. Due to their metallic property TCs reflect IR and UV, and yet show transparency in the visible region, which is well-defined and can be tailored depending on the user's needs. Also their ability to conduct electricity while allowing the light through makes them ideal materials for photovoltaic and display devices.[1]

The first transparent conductive material was synthesised by Badeker in 1907, who observed that an oxidised cadmium film remained transparent, while maintaining its conductivity.[2] Today a wide variety of TCs are available starting from thin metallic films; TCOs, both crystalline and amorphous and carbon based materials, such as graphene and carbon nanotube films.

The most commonly used ones in industry are metallic thin films and TCOs. Metallic films, such as gold, silver, copper or platinum maintain their transparency, due to the deposition on the substrate *via* physical vapour deposition (PVD) technique (transmittance in visible of 6 nm thin silver film is reaches to 65%, gold 70%, platinum 60%).[3]

TCOs owe their transparency over the visible wavelengths combined with electrical conductivity to the fact that the binary metal oxides they are based on have a large band gap (≥ 3.2 eV). TCOs are mostly *n*-type due to their ability to form oxygen vacancies (see paragraph 1.2.2). Industry today is dominated by crystalline indium, tin, zinc, cadmium and gallium based TCOs, such as indium tin oxide (ITO) displaying

optical transmittance of 85% at 550 nm, resistivity of 7.5 x 10^{-4} Ω cm and an optical band gap of 4.2 eV,[4, 5] FTO- transmittance of 80% at 550 nm, resistivity of 4 x 10^{-4} Ω cm and optical band gap of 4.1 eV.[6, 7] Doping ZnO (band gap of 3.3 eV)[8] results in: GZO (gallium doped ZnO) with transmittance above 90% at 550 nm and resistivity of 8 x 10^{-5} Ω cm,[9] AZO (aluminium doped ZnO) with transmittance about 90% at 550 nm and resistivity of 4.7 x 10^{-4} Ω cm[10, 11] or IZO (indium doped ZnO) with transmittance at 87% at 550 nm and resistivity of 9 x 10^{-4} Ω cm.[12]

Another group of TCOs are amorphous films (a-IZO and a-IGZO), which can reach comparable electrical and optical properties to traditional, crystalline materials, but have advantages of very smooth surfaces and low temperature of deposition, allowing application on plastic and electronic substrates.[13-15]

Graphene coatings are not only one atom thick, displaying transmittance from 80 to 95%, but also demonstrate outstanding performance while operating under bending conditions at up to 138 °, while exhibiting only few hundreds Ωcm resistivity than ITO thin films.[16] Alternatively graphene sheets can be folded into the carbon nanotubes, displaying either metallic or semiconducting properties, depending on the chiral vector of folding.[17]

1.2. Titanium dioxide

Titanium dioxide is one of the most investigated system in material science.[18] The wide range of application, chemical and biological inertness, low cost, eligibility for many experimental techniques and possibility of tailoring its properties are the driving forces for pursuing research on TiO_2. There are four polymorphs occurring in nature: rutile, anatase, brookite and TiO_2 (B) (monoclinic).[19] It is used in heterogeneous catalysis, as a photocatalyst, a white pigment (51% of total TiO_2 worldwide production) in all kinds of paints, in paper and cosmetics, antireflection coatings in

silicon solar cells and thin film optical devices, as well as an anti-corrosion protective coating. TiO_2 is also used in ceramics, as a biocompatible component of bone implants, gas sensor, as a metal-oxide semiconductor field-effect transistor (MOSFET) due to its dielectric gate, spacer material in magnetic spin-valve system. It can also be used as an anode material for Li-ion batteries[19-24] and for photoinduced water splitting.[25]

1.2.1. TiO_2 polymorphs

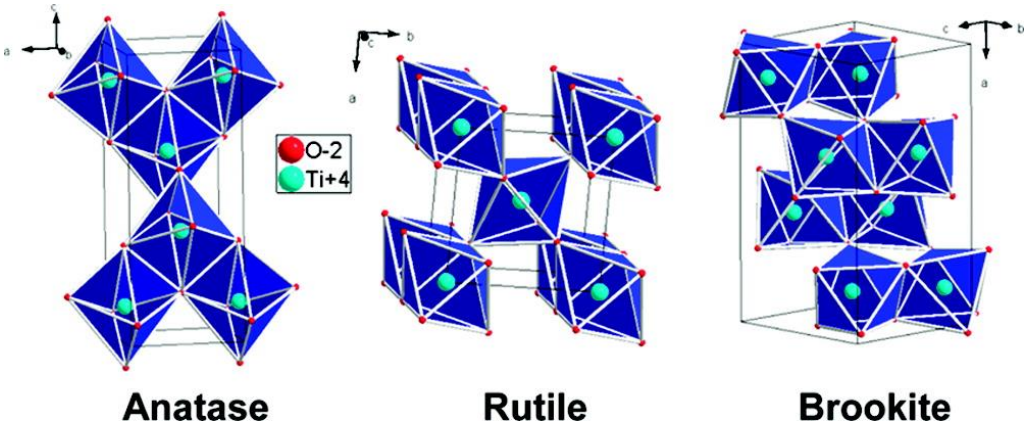

Fig. 1. 1 Diagram of crystal structures of (a) anatase, (b) rutile and (c) brookite. Adapted with permission from Dambournet *et al.*[26]. Copyright 2010 American Chemical Society.

Most commonly used polymorphs of TiO_2 in the industry are anatase (tetragonal, $D_{4h}^{19} - I4/amd$, $a = b = 3.782$ Å, $c = 9.502$ Å), rutile (tetragonal, $D_{4h}^{14} - P4_2/mnm$, $a = b = 4.584$ Å, $c = 2.953$ Å), brookite (orthorhombic, $D_{2h}^{15} - Pbca$, a = 5.436 Å, b = 9.166 Å, c = 5.135 Å)[27, 28] or a mixture of them. Their structure consists of a Ti atom surrounded by 6 oxygens (TiO_2^{-6}) in a more or less distorted configuration. The octahedra in anatase are connected by their edges, forming a (0 0 1) plane, in rutile, by the vertices, forming (1 1 0) plane and in brookite by both edges and vertices[20]. Rutile is thermodynamically the most stable of all the polymorphs, by 1.2 – 2.8 kcal / mol over anatase[29, 30]. However the particle size may affect the stability due to surface-energy effects. That makes anatase most stable at a particle size below 11 nm, brookite, between 11 and 35 nm

and rutile over 35 nm.[31, 32] The transition between anatase to rutile phase of TiO_2 occurs only at temperatures above 600 °C.[33] At room temperature this process is so slow, that practically it does not occur. The phase determination and conversion is an important factor, as it determines the use of TiO_2 as a photocatalyst (addition of rutile (30 – 35%) to the anatase (70 – 75%) phase of TiO_2 increases the photocatalytic performance),[34-36] as catalyst, ceramic membrane material, TCO or an anode for Li-ion batteries. Tang *et al.*[37] showed the differences in the electrical and optical properties between anatase and rutile crystalline films, reporting on the insulator-metal transition in a donor band in anatase thin films with high donor concentration, while such effect does not occur in rutile thin films with comparable donor concentration, showing semiconductor behaviour. This is caused by the larger effective Bohr radii of donor electrons, therefore smaller electron effective mass in anatase than in rutile phase of TiO_2.[38] As an effect of smaller e^- effective mass, anatase crystals have higher charge mobility.

1.2.2. Doping and carrier formation

In the pure, defect free materials at 0 K, all the electrons occupy their ground state energy levels. This can be changed either by a thermal (entropy driven) or external (doping) introduction of defects such as vacancies or interstitials. Introducing either various transition metals or non-metal ions may lead to enhancing either photocatalytical or electrical properties of the titania. There are two ways of doping elements into TiO_2. Substitutional doping occurs when either oxygen or titanium are replaced within the lattice. Interstitial doping occurs when the dopant fits in the empty space created in between the TiO_2 lattice. This process can be described by Kröger-Vink equation:[39]

$$(null)O_O^x \rightarrow \frac{1}{2}O_2(g) + V_O^{\bullet\bullet} + 2e' \quad (1)$$

As a result a non-stoichiometric material is obtained. If due to the oxygen vacancies (*V)* free carriers (*e'*) are generated, the equation constant can be written as:

$$K = [V_O^{\bullet\bullet}][e']^2 p_{O_2}^{\frac{1}{2}} \quad (2)$$

where $V_O^{\bullet\bullet}$ are oxygen vacancies, e' are free electrons and $p_{O_2}$is the partial oxygen pressure. If $[V_O^{\bullet\bullet}]$= ½ $[e']$, then free electron concentration can be given by equation:

$$n = [e'] = (2K)^{\frac{1}{3}} p_{O_2}^{-\frac{1}{6}} \propto \sigma \quad (3)$$

Where σ is electrical conductivity, inversely propotional to the oxygen partial pressure.

1.2.3. Electrical properties

1.2.3.1. Hall effect

To properly determine the electrical properties of semiconductors the charge carrier mobility μ (cm^2 / Vs), charge carrier density n (cm^{-3}) and bulk resistivity ρ (Ω cm) is needed. It can be measured using the Hall effect, through the basic principle of the Lorentz force (**Fig. 1. 2**). If the magnetic B (*y*-axis) and the electric E (*x*-axis) fields are simultaneously applied across the material there will be current drift along the *x*-axis, deflected parallel to the *z*- axis, which results with an excess of negative charge on one side of the sample. This results in the Hall voltage V_H, described as a drop of the potential across two sides of the sample. Knowing current density I, magnetic field B, sample's thickness d, Hall voltage V_H, charge carrier concentration n in semiconductor can be calculated according to the equation:

$$|V_H| = \frac{IB}{nqd} \quad (4)$$

where q (1.602 x 10^{-19} C) is an elementary charge. If the Hall voltage is negative then semiconductor is *n*-type, if positive *p*-type.

In order to determine bulk resistivity ρ and charge carrier mobility μ, the sheet resistance R_S is needed and can be obtained using the van der Pauw resistivity measurement technique.[40]

$$\mu = \frac{|V_H|}{R_S I B} \tag{5}$$

where μ is charge carrier mobility, R_s is sheet resistance, V_H is Hall voltage, I is a current and B is magnetic field.

$$\rho = R_S d \tag{6}$$

where ρ is a bulk resistivity, R_S is sheet resistance and d is thickness of the sample.[41-43]

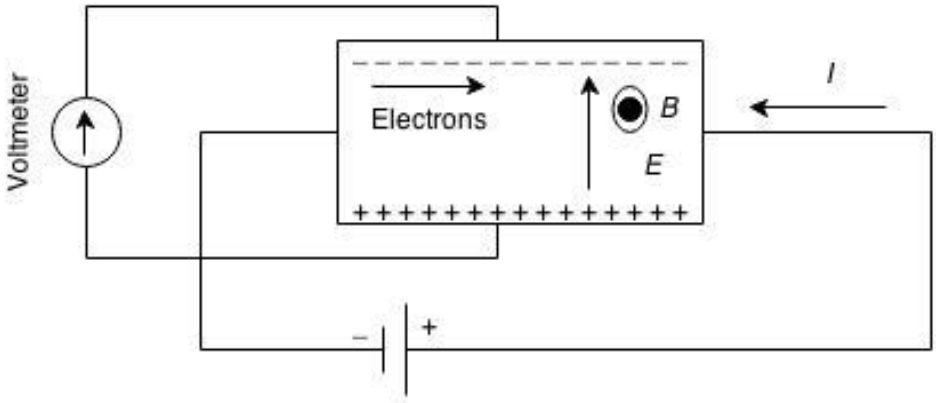

Fig. 1. 2 Schematic illustration of the Hall effect.[41]

1.2.3.2. Band gap

The band theory of solids states that during formation of the crystal, discrete electronic energies of single atoms merge into energy bands, representing allowed electrons transitions.[44] These energy bands can be separated by forbidden gaps. The size of the gap (energy band gap (E_g), distance between maximum energy in the valence band and the minimum energy in the conduction band, given in eV) determines the optical and electrical properties of the solid. Materials will have electronic properties if

electrons are partially spread between one or more bands. If electrons entirely fill one or more bands then the material is an insulator, as electrons in the filled bands make no contribution to the conductivity (**Fig. 1. 3**). Insulators can become a semiconductor if T > 0 K, when some electrons are thermally excited and fill in the lowest empty band. This kind of conduction is characteristic for intrinsic semiconductors.[45]

Measuring and calculating the band gap energy can distinguish the type of conductivity in a solid. If the material is a semiconductor, its E_g will vary between 0 and 4 eV, and for insulators E_g is considered large and exceeds 4 eV. In metals the conduction and valence bands overlap.[46]

The band gap energy is a function of temperature. When the temperature rises, E_g decreases, which results in increased amounts of electrons excited into the conduction band and can be described by Varshni's equation[47]:

$$E_g(T) = E_g(0) - \frac{\alpha T^2}{T + \beta} \qquad (7)$$

where $E_g(0)$, α and β are fitting parameters characteristic of a material.

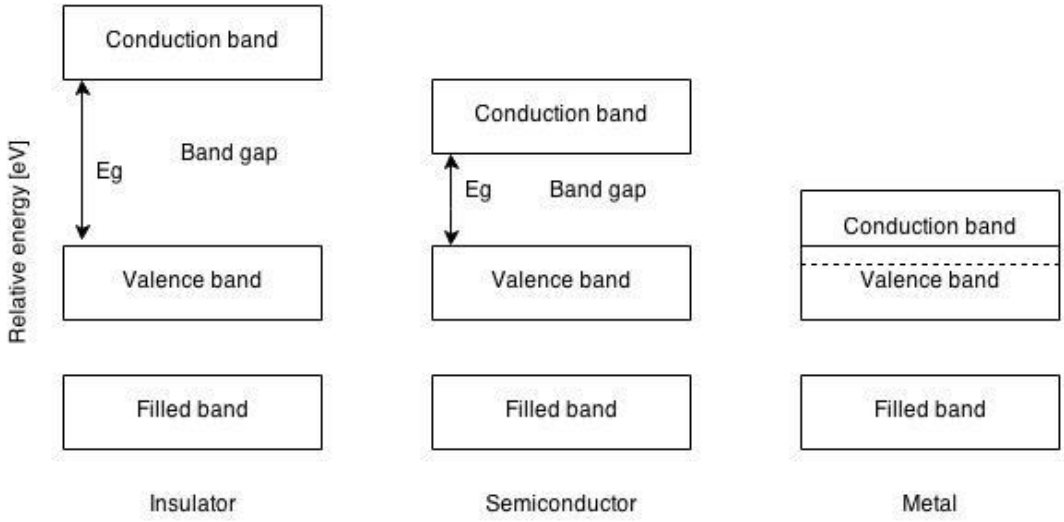

Fig. 1. 3 Schematic illustration of energy bands in solids.

1.2.4. Photocatalytical properties

Photocatalytical reaction is defined as a photochemical process occurring at the surface of a solid material, usually a semiconductor. In principle, this definition applies to the combination of chemical, photochemical and electrochemical reactions taking place in the semiconducting material and on its surface. This includes simultaneous occurrence of oxidation reactions initiated by photogenerated holes, and reduction reaction, initiated by photogenerated electrons.[48-51]

In 1972 Fujihima and Honda discovered that TiO_2 could be used to make electrodes that can photocatalytically split water.[52] This has inspired research about TiO_2 based photocatalysts for environmental cleanup of polluted air and wastewaters, water-splitting, window coatings with self-cleaning properties and selective oxidation reactions in organic chemistry.[53, 54] Small additions of TiO_2 into metal-based catalysts can improve their performance in a profound way.

The photocatalytic phenomenon is induced by the absorption of the photon by the semiconducting TiO_2. If the photon has high enough energy it leads to charge separation caused by the promotion of an electron e^- into the conduction band and generation of the hole h^+ in the valence band (**Fig. 1. 4**).[55] This is possible because unlike in metals, valence and conduction bands in semiconductors are separated, therefore the electron – hole (e^-/ h^+) pair recombination can have sufficient life time to promote redox reactions on the surface of the catalyst.[56] In the case of TiO_2, the band gap depends on the crystal structure, which has an impact on the densities and electronic band structures. The value of a band gap for anatase form of TiO_2 is 3.2 eV, rutile 3.02 eV and brookite 3.22 eV.[43, 57-59] If the surface of the material is clean, and there is no scavenger present the (e^-/ h^+) pair can take part in redox process within TiO_2. Although if the surface is contaminated, the scavenger can trap either electron or hole, preventing them from recombination, by reacting with donors and acceptors

adsorbed on the surface. The presence of water and oxygen is essential for photocatalytic reaction to occur. No molecule can be decomposed in the absence of either.[20, 60, 61]

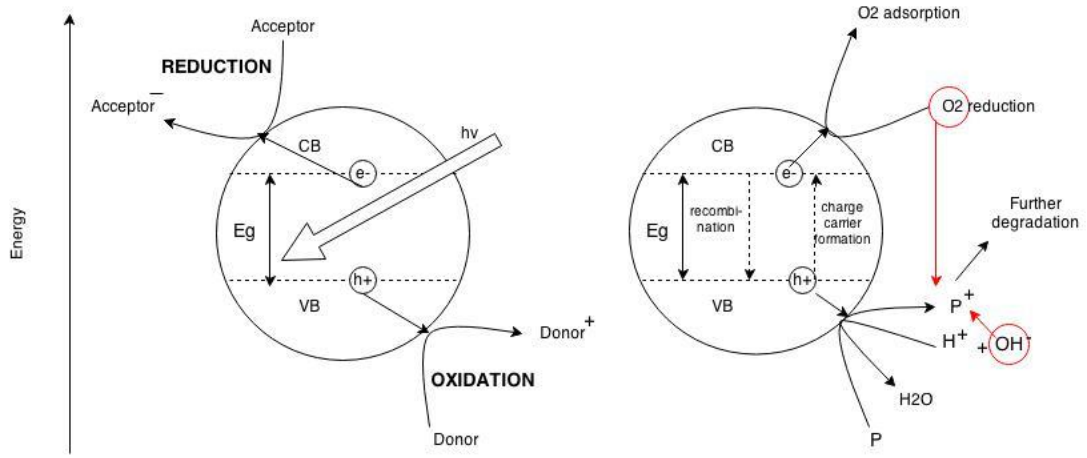

Fig. 1. 4 Schematic illustration of photocatalytic process of degradation of pollutant (P).

The most common way of determining the photocatalytic properties of a material is by observation of reduction of an organic "pollutant" applied on the surface. In this report to determine photocatalytic properties of niobium doped titania thin films Resazurin dye[62] was used. The mixture of dye comprising of redox dye Resazurin and the sacrificial electron donor glycerol within an aqueous hydroxy ethyl cellulose (HEC) polymer media is evenly sprayed on the sample and industrial standard and then its reduction is induced by a 365 nm lamp. Progress of the reduction is monitored by measuring absorbance spectra of the dye. As a result of a photocatalytic reaction on the surface of the material, the blue Resazurin (R_z), with absorbance maximum at 608 nm is reduced to pink Resafurin (R_f), with absorbance maximum at 580 nm. This process is illustrated in the **Fig. 1. 5**.

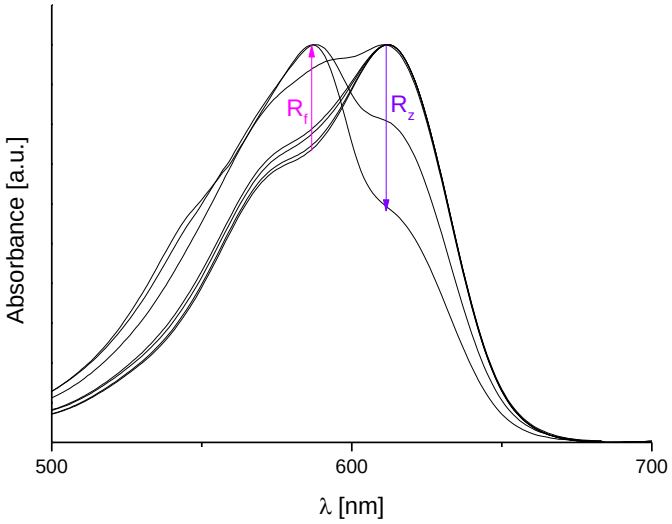

Fig. 1. 5 Illustration of change in Resazurin dye absorption spectrum.

1.3. Low-emissivity glass

Low-emissivity glass is a type of glass that has a high transparency index in the visible range as well as high reflectance in the infrared. These two parameters play key roles in a building's energy use and the comfort of its occupants. Visible transmittance of glass depends on the coating type. Uncoated glass transmits around 90% of incident light and for coated, highly reflective glass transmittance is about 10%. The higher reflectance- the lower emissivity of a window, which means that heat transferred by infrared energy, is reflected from the window instead of being absorbed by the glass and transmitted into the building. Uncoated windows have an emittance index around 0.84 over the IR spectrum, which means that only 16% of the IR waves are reflected. In comparison new low- emissivity windows coatings have an emittance index as low as 0.04.[63] Windows, which were covered with such a glazing, transfer only 4% of the IR heat that reaches its surface.

The reflectivity, emissivity and transmittance can be manipulated by using different materials. Therefore designing a window which would optimize the relationship between solar heating, cooling and transmittance of daylight is possible.[64]

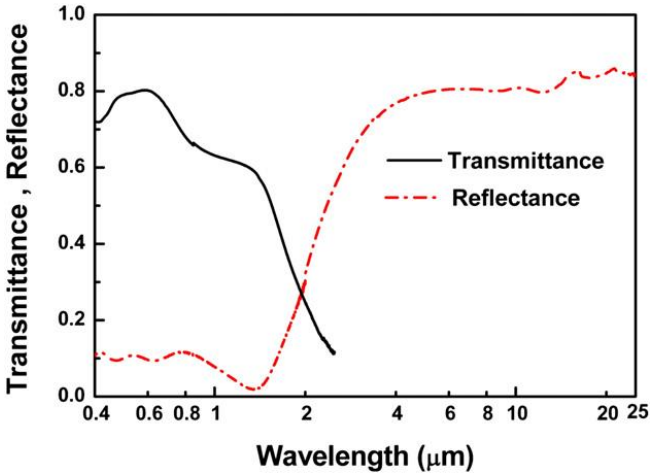

Fig. 1. 6 Transmittance and reflectance spectra of low-e glass (adapted from reference[65]).

1.4. Titanium dioxide based semiconductors

Titanium dioxide (TiO_2) is commonly known for its *UV-vis* enhanced photocatalytic and self-cleaning properties. Mechanical and chemical durability, transparency in the visible range, as well as high refractive index,[66] relatively low cost, high dielectric constant, resistance to photo-corrosion,[67] high photo-activity and photo-induced super-hydrophilicity make titania thin films a desirable product for glass enamel, optical coating and protective layer for integrated circuits.[68-70] TiO_2 is also a great material for use in gas sensors, as reactions occurring at its surface are easily reversible and the material has stable chemical and thermal properties over prolonged use.[71]

While displaying the aforementioned properties, the intrinsic band gap of TiO_2 is 3.2 eV and 3.0 eV respectively for anatase and rutile, the two most common crystalline forms of titania, and a resistivity of about 1 x 10^6 Ω cm; therefore TiO_2 is classified as an insulator.[37] Absorbance of a photon, energy of which matches or exceeds this band

gaps, promotes an electron from the valence band into the conductiving band, leaving the hole in the valence band.[43] This phenomenon is responsible for the process of photo-oxidation and photo-reduction reactions, but are limited by the fact, that the band gap energy corresponds only to *UV* light (< 400 nm), which only comprises about 4% of sunlight.[72] The functional properties of titania, can be improved by maximization of the utilization of visible light, by introducing aliovalent cations that form donors and acceptors and modify the electronic structure, as well as by changing its oxygen sub-stoichiometry.

1.4.1. TiO_2 in batteries

Titanium dioxide has been proposed as a suitable candidate as a negative electrode material due to its low cost, environmental inertness, lithium ion storage capability, flat operational potential, long cycle life and durability.[68, 73] The lithium insertion / deinsertion of rutile TiO_2 is highly anisotropic into the 1D channels. Along the *c*-axis the lithium diffusion is fast while it proceeds very slow in the *ab*-plane [74]. Experimental and simulation studies showed that the lithium ion diffusion along the *c*-axis was about 10^{-6} $cm^2\ s^{-2}$ whereas it was only 10^{-15} $cm^2\ s^{-2}$ in the *ab*-plane (see **Fig. 1. 1**).[75-78] Furthermore, in micron-sized rutile the very slow diffusion in the *ab*-plane hinder the lithium ions to access the thermodynamically favorable octahedral sites and comparable to lithium iron phosphate (LFP) lithium ion pairs can block the *c*-channels and stop further lithiation because of the poor diffusion in the *ab*-plane.[75, 79] It has been shown that the amount of stored lithium-ions in the rutile host is related to the particle characteristic. For bulk rutile TiO_2, only 0.03 mol of lithium-ions (*ca.* 30 mAh g^{-1}) can be stored at an applied current of 30 mA g^{-1} (*ca.* 11 h), whereas nanosizing can drastically increase the amount.[80, 81] Therefore, the main strategy for optimized electrochemical performance of rutile TiO_2 is to drastically decrease the particle size along the *c*-axis in the direction of

the electrolyte. This can be obtained by doping TiO_2 with niobium into the structure, as Nb – O distances increase, therefore expand the whole unit cell volume, as Nb has larger atomic radius than titanium (0.0640 nm and 0.0603 nm, respectively).[82] Successful doping of Nb into the TiO_2 lattice results in improving other properties useful in lithium ion batteries, such as increased electrical conductivity, while maintaining a wide band gap (from 3.20 eV for anatase and 3.03 eV for rutile[83]) and smaller crystal sizes with higher surface area than in pristine material, yet similar high mechanical and chemical stability.[84]

1.4.2. Niobium doping

Niobium doped titanium dioxide films have recently been found to offer promising competition for ZnO films doped with gallium or aluminum as well as indium tin oxide (ITO) for application as transparent conducting oxides (TCOs) as windows and contact layers for thin films solar cells, optoelectronics applications[85, 86] and flat panel displays.[87] Both materials exhibit great transparency and conductivity, but the high price of indium along with its limited availability[88] and zinc oxide susceptibility to moisture,[89] demonstrates the need for a durable, robust, corrosion stable and cheap analogue material. Metal doped titania is a viable option as a TCO for optoelectronics application, since its durability is greater than most commercially available TCO's. Promising candidates including niobium doped titania films with the required low resistivity, have been formed by pulsed laser deposition (PLD) by Furubayashi *et al*.[85]. The contribution of ~1 electron per each niobium atom substituted into the TiO_2 lattice at the low doping level (up to 6%) resulted in obtaining high transmission (97% at 550 nm, with film thickness of 40 nm) thin films with charge carrier concentration in a range of 10^{19} to 2 x 10^{21} cm^{-3} and resistivity of 2 – 3 x 10^{-4} Ω cm. In the titania lattice niobium doping forms donor-type centers. The charge carrier compensation in Nb:TiO_2

in both reducing and oxidizing environments is controlled by the electronic and ionic charge compensation, respectively. Also reducing environment increases significantly the electrical conductivity of Nb doped TiO_2.[90] Although it sometimes leads to the reduction of the Nb^{5+} to Nb^{4+} or Nb^{3+} and coloring the film blue or purple respectively and causing substantial decrease in electrical conductivity due to the charge carrier compensation.[16] The effect that Nb has on the properties of titania can be explained by concentration of Ti vacancies, created during incorporation of the former into the TiO_2 lattice[91] as shown in following equilibria[67, 92]:

$$2\ Nb_2O_5 \leftrightarrow 4Nb_{Ti}^{\bullet} + V_{Ti}^{\bullet\bullet\bullet\bullet} + 10\ O_O^x \quad (8)$$

$$[Nb_{Ti}^{\bullet}] - [V_{Ti}^{\bullet\bullet\bullet\bullet}] \quad (9)$$

where $V_{Ti}^{\bullet\bullet\bullet\bullet}$ are titanium vacancies, $Nb_{Ti}^{\bullet}$ are niobium atoms occupying Ti site in TiO_2 lattice and • relates to the electronic charge of the species corresponding to the occupied site. The charge of the species is calculated by the deduction the charge on the original site from the charge of the current site.[39]

So far Nb:TiO_2 with electrical properties comparable with the industrial standards were obtained by PVD or PLD deposition onto single crystal substrates ($SrTiO_3$ and $LaAlO_3$), which are not practical for the commercial applications, as TCOs should be deposited onto less expensive substrates such as glass or polymers.[93] Another two methods of overcoming this problem are to deposit an anatase seed layer at high oxygen partial pressure and then apply low oxygen partial pressure or to deposit amorphous titania and anneal it in a hydrogen atmosphere to obtain the desirable crystallinity and phase orientation.[16, 93-95] Yamada *et al.* have reported on the TCO properties of Nb:TiO_2 thin films formed by using a seed layer of $Ca_2Nb_3O_3$ nanosheets, which were RF magnetron sputtered on glass. Films obtained this way were uniaxially oriented with the resistivity of 7.6 x 10^{-4} Ω cm, further annealing in H_2 atmosphere has led to a reduced resistivity of 4 x 10^{-4} Ω cm.

Okazaki on the other hand has obtained Nb:TiO_2 with TCO properties *via* crystallisation of an amorphous $Ti_{0.94}Nb_{0.04}O_2$ thin film under N_2 atmosphere at 350 °C for 20 min. Prior to the heat treatment films were RF magnetron sputtered onto the glass substrate. Obtained films were polycrystalline with resistivity of 8.4 x 10^{-4} Ωcm and absorbance of 6% at a wavelength of 460 nm. Using a similar method, but higher annealing temperature (500 °C) Hitosugi *et al.* have obtained films with resistivities of 4.6 x 10^{-4} Ω cm and transmittance of 60 – 80% in the visible region. Annealing RF magnetron sputtered amorphous Nb:TiO_2 thin films in an Ar plasma at 350 °C resulted in films with resistivity of 1.5 x 10^{-3} Ω cm and transparency of approximately 80% in the visible region.[96] Also post-deposition annealing in vacuum at 450 °C for 30 min of Nb doped TiO_2 amorphous films prepared on glass *via* RF magnetron sputtering resulted in films displaying resistivity of 3.6 x 10^{-3} Ω cm and transparency of 80%.[97, 98] Niobium doped TiO_2 thin films deposited *via* AACVD technique without further annealing resulted in blue coloured films with resistivity of 1.3 x 10^{-3} Ω cm and the lowest transparency from all the methods mentioned above of 50% at a wavelength of 500 nm.[99]

Niobium doped TiO_2 find application also in dye- and quantum dot-sensitised solar cells, in photocatalysis and as anode materials (see **1.4.1**). Doping of niobium into the TiO_2 lattice was introduced to improve the efficiency of the photocatalytic activity by extending the absorption into the visible region, thereby enhancing the activation of the film by sunlight[100]. Nb doped titania thin films prepared *via* the sol – gel method and annealed in the air degraded 97.3 % of methylene blue in 2 h of UV irradiation[82, 101]. Sol – gel and hydrothermal processes can be also used for the synthesis of Nb:TiO_2 on FTO glass used as a contact layer. Such prepared films enhance carrier transport properties in dye- and quantum dot-sensitised solar cells.[102-104]

1.5. Silver- TiO_2 composites

Silver nanoparticles and nanoclusters are thermodynamically unstable in water, [105] that is why immobilizing them on the solid substrate has a huge impact on improving the photocatalytical properties of the silver used as a catalyst in many current industrial processes.[106-108] Decorating TiO_2 with silver nanocomposite electrodes, enhances its photo-electrochemical response. Silver particles act as electron reservoirs suppressing (e^-/ h^+) recombination, therefore extending (e^-/ h^+) life for more efficient *red/ox* reaction (see **1.2.4**).[109-111] Methods of decorating silver onto TiO_2 vary from wetting-thermal decomposition of saturated solution of silver acetylacetonate using spin-coater for even distribution,[109] combining hydrothermal synthesis of TiO_2 particles with silver mirror reaction.[110] In order to introduce robustness into their Ag/TiO_2 nanocomposite Gao *et al.* immobilized them on the substrate by the use of hydrophilic (heptafluoro-1,1,2,2-tetradecyl)-trimethoxysilane, which not only improves water repellency but also does not affects the photocatalytic properties. Sun *et al.* report a liquid phase deposition (LPD) method of co-depositing durable Ag/SiO_2- TiO_2 composites, where Ag NPs are trapped between a SiO_2- TiO_2 matrix[112] and Yu *et al.* used a LPD method to deposit either Ag doped anatase TiO_2 or composites of Ag NPs and anatase/ rutile/ brookite mixed phases of TiO_2 by changing the concentration of $AgNO_3$ in the starting solution.[113] Similar results were obtained by Zhang *et al.* and Daniel *et al. via* the sol-gel method.[106, 114] Liu *et al.* introduced silver nanoparticles by soaking TiO_2 mesoporous films in aqueous ammoniacal silver nitrate solution, which further spontaneously reduce and aggregate into NPs.[115] Hajivaliei[116] used an electrical arc discharge method to decorate Ag onto TiO_2 NPs and Ponja[117] overdeposited silver film from the water-methanol silver nitrate solution on the top of a TiO_2 thin film *via* an AACVD technique. Although different methods were used for all of the mentioned cases

of Ag decorating in each case it improved the photocatalytical properties of the material.

1.6. Epitaxial growth of TiO_2

Epitaxial growth of single crystal TiO_2 structures has attracted interest due to its direct electrical pathways for photogenerated electrons and increased electron transport rate, this has led to improved performance of ordered hybrid bulk heterojunctions and dye- and quantum-dot-sensitised solar cells.[118-120] Growing single-crystalline TiO_2 films is difficult due to its crystal structure and the symmetry of anatase and rutile phases. A solution to this problem is an epitaxial relationship between the templating substrate and the desirable TiO_2 phase. This plays a key role in driving the nucleation and growth of single-crystalline orienteted structures. Literature examples of such growth are presented below.

Liu and Aydil described growth of oriented single-crystalline rutile TiO_2 nanorods on FTO glass, where small lattice mismatch (2%) promotes the epitaxial nucleation and growth of rutile TiO_2 nanorods. This is possible as both FTO and rutile has tetragonal structure (FTO *a = b = 4.687 Å*[121] and rutile TiO_2 *a = b = 4.594 Å*).[122] Nanorods synthesised this way were successfully applied to dye-sensitised solar cells and obtained 3% light-to-electricity conversion efficiency.

A commonly used single crystal substrate for growing rutile TiO_2 thin films is sapphire α-Al_2O_3 (0 1 2), with a lattice mismatch of 3.57% to the rutile (1 0 1) TiO_2 (α-Al_2O_3 *a = b = 4.759* Å).[123, 124]

Chambers *et al.*[125] have used lattice mismatch of 3.1% between cubic $SrTiO_3$ (0 0 1) and tetragonal anatase phase of TiO_2 in order to grow Co doped TiO_2 well-crystalline thin films, with ferromagnetic properties at and above room temperature ($SrTiO_3$ *a = b = 3.905* Å[126] and anatase TiO_2 *a = b = 3.782* Å).[28]

Another single crystal substrate with an epitaxy to antase TiO_2 is $LaAlO_3$, with the lattice mismatch of – 0.1%[36] ($LaAlO_3$ $a = b = 3.78$ Å).[127] The TiO_2 thin film grown on $LaAlO_3$ (0 0 1) crystallises by matching with the (0 0 4) plane of anatase.

1.7. Film deposition techniques

There are many techniques of thin film deposition, both chemical and physical, which have developed many variations in order to balance advantages and disadvantages of various strategies based on the requirements of film purity, structural quality, growth rate, temperature limitations, precursors' availability and other factors.[128]

Physical deposition processes comprise of evaporation, sublimation or ionic impingement on a target, allowing the transfer of atoms from a solid or molten source onto a substrate, usually under vacuum. Most commonly used types of physical deposition are evaporation, such as molecular beam deposition and sputtering, such as RF magnetron sputtering.[128-130]

Chemical deposition techniques can be divided into two main groups: chemical vapour deposition (CVD) and wet processes.

CVD of films and coatings involves the chemical reactions such as dissociation and thermal decomposition of gaseous reactants on or in the proximity of a activated substrate either by heat, light or plasma followed by the formation of a stable solid product.[131] Evaporation and transport of the precursors can be done either by sonification of the solution, heat treatment or pressure reduction.[132] Also depending on the type of the process the atmosphere in which reaction takes place can be vacuum, air or inert gas. A non-exhaustive list of commonly used CVD techniques is as follows: atomic-layer CVD, photo-assisted/initiated CVD, atmospheric pressure CVD, aerosol

assisted CVD, metalorganic CVD, thermal spray CVD, direct liquid injection CVD, plasma enhanced CVD, ultrahigh vacuum CVD etc. [129, 133-135]

Wet film deposition processes can be divided into the chemical bath and *sol-gel* techniques. Preparation of the film by *sol-gel* can be broadly described as composing a colloid suspension of either dispersed phase that would be later applied on the substrate and the solvent would be evaporated, or colloid suspension of precursors, that would be later applied on the substrate and annealed in order to evaporate a solvent and decompose precursors leading to the ceramic film.[136] Popular means of applying colloidal suspension on the substrate are spin-coating, dip-coating or doctor-blade technique.[137, 138] Chemical bath deposition is a term describing deposition of the films on the substrates, which are immersed in the solution containing metal ions and source of hydroxide, sulfide or selenide ions.[139] Two most common types are hydrothermal synthesis (see **1.7.2**) and LPD. LPD is purely based on the hydrolysis process of metal-fluoro complex, taking place in the aqueous solution, therefore by changing the scavenger of the F^- ratio and therefore controlling the hydrolysis rate, growth of the dense film can be executed even at the room temperatures. Another big advantage of the aqueous medium is environmental friendliness of the process. Because the deposition takes place in the low temperatures the variety of substrates, including complex morphologies, can be used, from polymers to glass and single crystals. The only limitation of the process is the size of the container able to fit in desired surface, as the substrates have to be fully emerged in the solution.[112, 140, 141]

Aerosol assisted CVD (AACVD) technique is used for deposition of niobium doped titania films in the 2nd, 3rd and 4th chapter of this thesis and uses a liquid aerosol to transport the mixture of precursors in a solution to the reactor chamber where they are deposited onto the substrate.

AACVD uses an ultrasonic humidifier to create the mist, which is transferred to the reaction chamber; therefore it eliminates the need of high vacuum or high temperature

to vaporize the precursors, this makes this method suitable for a variety of precursors, including thermally unstable ones. Other advantages of the AACVD process are that it allows performing single-step, *in situ* reactions, so precursors can be mixed together before entering the reaction chamber, which decreases the complexity of equipment needed for deposition. Films obtained by this method show good chemical homogeneity and can be easily reproduced with accurate control of the structure.[142]

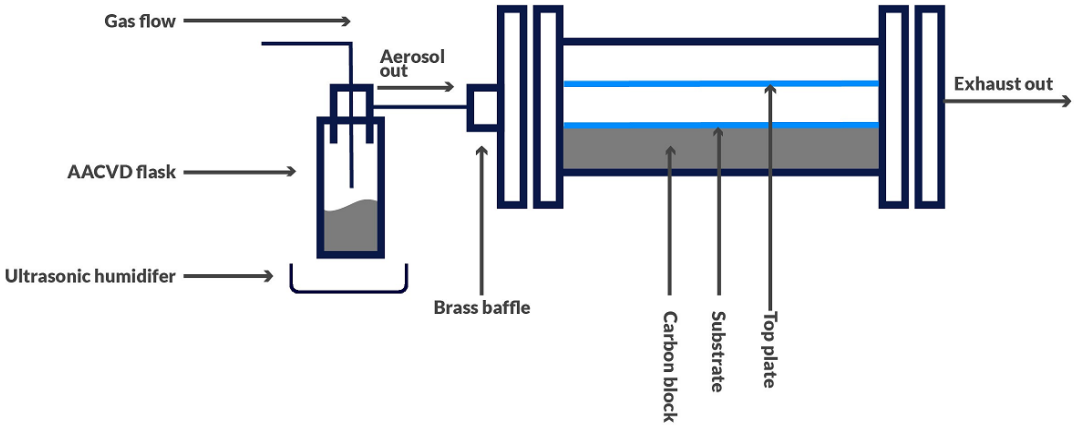

Fig. 1. 7 Schematic drawing of AACVD rig.

Fig. 1. 7 shows a schematic drawing of a cold-walled horizontal bed CVD reactor used in the AACVD process. Films are deposited on the bottom plate, with 50 nm silica coated barrier, to prevent cation migration. The top plate, also silica coated glass (dimension of both 145 x 45 x 5 mm), positioned 8 mm above bottom plate, and is used to ensure laminar flow of the precursors. The substrate is heated by carbon block with a thermocouple, to ensure constant and even temperature of the bottom plate. The complete assembly is enclosed inside a quartz tube. The aerosol of the precursors' solution is generated by ultrasonic humidifier and moved to the reactor using N_2 gas flow *via* a brass baffle, which allows control of uniformity of the mist. At the high

temperature above the substrate the solvent aerosol evaporates and the precursors, still in a gas phase, absorb onto the substrate, react and grow films on the substrate. The waste gas and by-products leave reactor *via* the exhaust.

1.7.1. Growth of a thin film via AACVD

A thin film is epitaxial if the atoms in the film are aligned with the substrate as in a single crystal lattice match to substrate. Such a technology is used in the deposition of films for micro- and optoelectronic devices and offers advantages that are not available for other methods, such as PVD or sol-gel, without further processing. It allows extremely good crystallinity of the films, which are chemically compatible to the substrate. It also gives an opportunity of tuning materials' properties, according to desirable applications.[128]

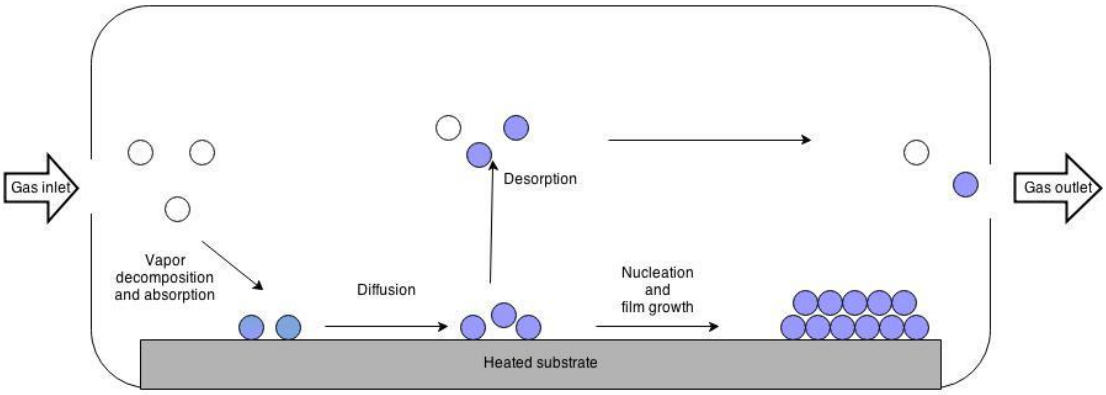

Fig. 1. 8 Schematic illustration of film growth by CVD process.

Even though epitaxial growth is the most desirable one, films deposited from vapors can have an enormous variety of structures, such as single crystalline, polycrystalline with columnar or equiaxed grains, crystalline mixed with amorphous or be simply amorphous. The final microstructure depends not only on the method, but also on materials used for deposition, solvents and temperature of the process.[133]

The process of the film formation (see **Fig. 1. 8**) begins with heating up precursors in order to produce vapor trust, at the temperature T_v, being transported into the reactor, where they decompose on contact of the gas phase reactants with the clean substrate, which is at temperature T_s. To form the film, atoms of the film material must arrive at the substrate and adhere to it. To obtain crystalline films, atoms should settle into the equilibrium position, while to form amorphous structures, they must avoid equilibrium positions. After absorption, which is a physical process, surface diffusion occurs which leads to chemisorption and formation of substrate – molecule and molecule – molecule bonds or desorption. Both physical and chemical processes have to be overcome including local energy barriers, as described by Arrhenius law:

$$k = A\ exp(\frac{E_a}{RT}) \tag{10}$$

where k is the film growth rate, A is a constant, E_a is the activation energy, R is the gas constant and T is the temperature of the process. The next step is nucleation followed by formation of microstructure. Nucleation is dependent on two parameters: temperature of the substrate (higher temperature- fewer, larger nuclei) and deposition rate (high rate- smaller nuclei). The last step of film formation is diffusion and grain growth. The diffusion rate increases with the temperature and its length can be defined as:

$$\Lambda = a\sqrt{k_s t} \tag{11}$$

where k_s is the diffusion rate, t is the diffusion time and a is the hop distance.

According to the Frank van der Merwe model of film growth (2 dimensional or layer-by-layer), if the surface energy between vapor and the substrate is larger than the other two combined, then the film created is atomically smooth, formed of layers.[143] The Volmer-Weber model shows creation of islands (3D islands), islands occur when the energy between vapor and substrate is lower than the total surface energy of the film and material tends to form islands to minimize the interface with the substrate. Growth of such a film is uneven.[144] Third, the Stranski- Krastanov model describes

mixed growth initialized by layer growth, followed by island growth after a few monolayers.[145]

1.7.2. Hydrothermal synthesis

Hydrothermal reaction can be defined as a process of synthesising ceramic materials directly from homogenous or heterogeneous solution at elevated temperature (T > 25 °C) and pressure (p > 1 atm). If solvent other than water is used then the term solvothermal synthesis should be used.[146]

In this thesis the hydrothermal technique is used to synthesise niobium doped TiO_2 powders as well as to grow thin films directly from aqueous solutions on the various substrates, as described in the 5th chapter of this thesis.

Hydrothermal method allows syntheses at autogenous pressure, which correlates to the saturated vapour pressure at a certain temperature and chemical composition of the reaction mixture. Current development and understanding of the hydrothermal process provides a tool of synthesising materials at temperatures less than 250 °C and pressures below 100 MPa. Hydrothermal synthesis takes place in a sealed autoclave (**Fig. 1. 10 (a)**). By increasing the temperature and pressure, the solvent or a mixture of solvents used in a process are brought to the temperature above the boiling point. Pressure and therefore the parameters of the reaction will depend on the composition of the reaction mixture, temperature of the reaction and the fill factor, which is the ratio between the volume of the reaction mixture in the vessel and its total volume. Simply by changing one of those parameters the reaction's outcome can be changed. **Fig. 1. 9 (a)** shows the importance of the autoclave's filling factor for the generated pressure inside.[147] The dotted line from starting point to the critical temperature point represents the moment when the liquid and gaseous phases are in the equilibrium state. Below the line liquid phase is not present and gaseous vapour is not saturated.

Above the line, the only existing phase is liquid, filling in the whole volume of the vessel. Solid lines represent the pressure inside the vessel initially only partially filled with water.[147, 148]

(a) (b)

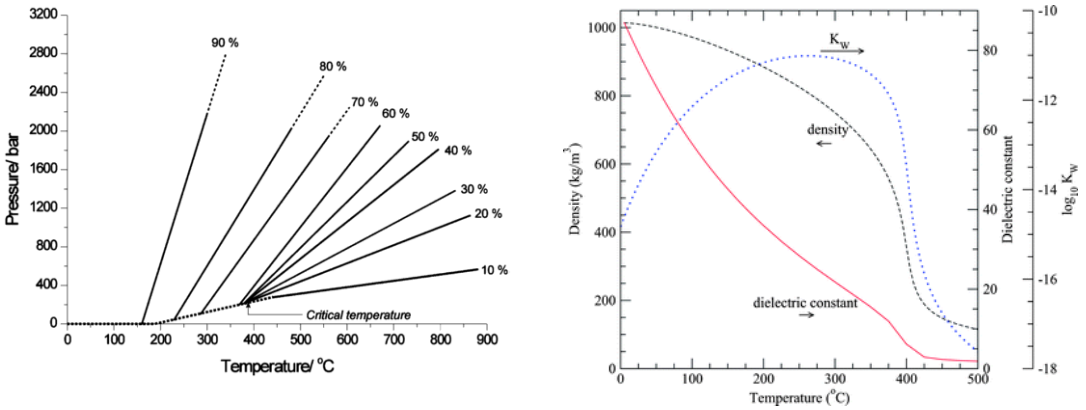

Fig. 1. 9 (a) dependence of pressure in the function of temperature of water for different degrees of vessel filling during the hydrothermal synthesis (reproduced from Walton[147] with permission from The Royal Society of Chemistry), (b) density, dielectric constant and ionic product of water at 30 MPa as a function of temperature (reproduced from Peterson[149] with permission from The Royal Society of Chemistry).

Because of the increased temperature and pressure in the system, the density, ionic product, dielectric constant and viscosity of solvents are prone to change.[149] **Fig. 1. 9 (b)** shows how the density, dielectric constant and ionic product (K_w) of water change with temperature (pressure is set constant at 30 MPa).[149] Water's density decreases with the increase of the temperature, while the density of the gaseous phase increases. When the parameters reach the critical temperature point (for water 374 °C, 218 atm), the difference in between the liquid and gas phase disappear and the solvent exists as a supercritical fluid. As for the dielectric constant of water, it decreases with the increase of the temperature and moves towards values characteristic for non-polar solvents, allowing dissolution of non-polar precursors. That causes higher reactivity, solubility and diffusivity of the reactants, which in many cases would be either insoluble or unreactive. In consequence, many inorganic materials can be made at

lower temperatures and using less harmful solvents than those corresponding to the traditional solid state chemistry.[150, 151]

(a) (b)

Fig. 1. 10 Picture of (a) Parr reactor including PTFE cup[152], (b) Savillex PFA digestion vessel[153] with a PTFE sample holder.

Hydrothermal synthesis (**Fig. 1. 11**) offers many others advantages over the conventional solid state chemistry. By adjusting reaction conditions many forms of ceramic materials can be prepared such as powders, fibers, nanoparticles, single crystals or thin films. It also allows regulating the rate and uniformity of the nucleation, growth and aging processes, which leads to the improved size and morphology control, as well as reduces aggregation levels. Materials prepared *via* hydrothermal method are characterised often by very high purity, often higher than that of the starting materials. This is due to the fact that the hydrothermal crystallization is a self-purifying process, in the course of which the forming crystals tend not to incorporate the impurities present in the solution, but are washed away from the system after the synthesis along with other residues.[146, 154]

Because hydrothermal synthesis takes place in the sealed container the volatilization of the solvents used in the process is minimal or even negligible, which

allows for excellent stoichiometry control but also facilitates ease of waste disposal or recycling.[155]

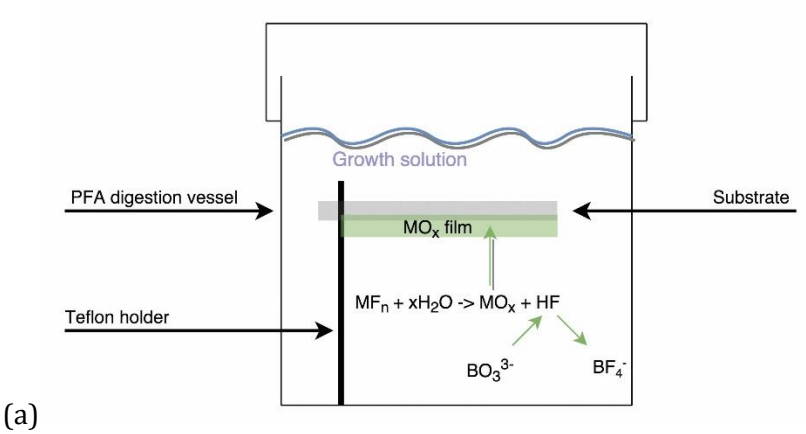

(a)

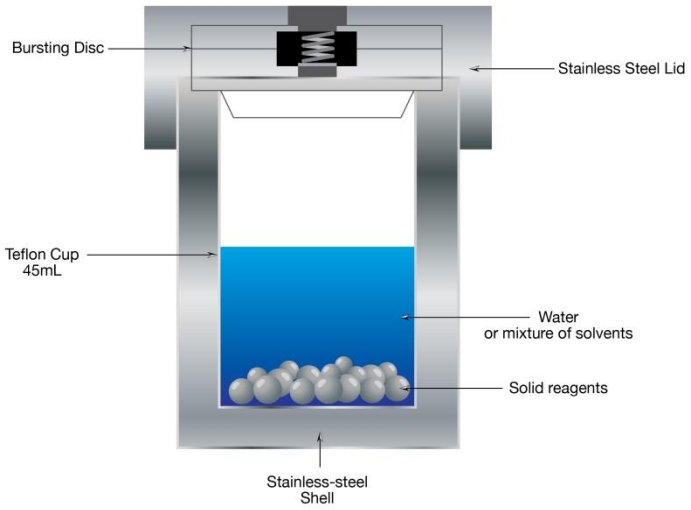

(b)

Fig. 1. 11 Schematic illustration of (a) film growth by hydrothermal process with the particular example of formation of metal oxide in the reaction of boric acid and metal fluoro-complex (b) autoclave for hydrothermal synthesis.

1.8. Basis of XAFS characterisation

1.8.1. XAS theory

In the X-ray absorption spectroscopy (XAS) a sample is bombarded by an X-ray beam of a definite energy. X-rays are absorbed by the atoms of a material and if energy of a photon matches or exceeds the binding energy of an electron, then the energy is given to the photo-electron which is ejected from the core. The absorption can be determined either by measuring and comparing the intensity of incident and transmitted beam, by measuring the fluorescence of excited atoms or by measuring the Auger electrons. Fluorescence is more likely to occur in the hard X-ray regime (> 2 keV), while Auger emission dominates in a soft x-ray regime (< 2keV). Each of these techniques can be used to calculate the absorption coefficient μ, which is necessary to obtain X-ray absorption fine structure (XAFS). X-ray undergoes Beer's law[156-158]:

$$I = I_0 e^{-\mu t} \tag{12}$$

where I is an intensity of a beam transmitted through the sample, I_0 is an intensity of an incident x-ray, t is a sample's thickness.

A XAFS spectrum is a product of absorption coefficient μ in the function of incident X-ray energy of the specific core level of a specific atom. Since the binding energies of core electrons in every atom are well known, XAS gives an opportunity to choose element to probe, by selecting the X-ray energy specific to an absorption edge.[156-158]

$$\mu(E) = \log\left(\frac{I_0}{I}\right) \tag{13}$$

or

$$\mu(E) \propto \frac{I_f}{I_0} \tag{14}$$

where I is an intensity of a beam transmitted through the sample, I_0 is an intensity of an incident x-ray and I_f is an intensity of the fluorescence or electron emission.

XAFS is element specific and is dependent on the formal oxidation state, coordination chemistry, distances between selected atom and its neighbor-atoms and the local atomic structure. Because XAFS probes the atom it is one of the few methods of determining the structure of material that does not require the crystal structure of a material, therefore amorphous and highly disordered materials as well as solutions can be investigated.[156-158]

A XAFS spectrum consists of 4 parts:

1. Pre-edge, which is a trend at the lower X-ray energies than the electron binding energies.
2. Edge, sharp rise, which occurs when energy of X-ray photons matches or exceeds electron binding energy.
3. X-ray absorption near-edge structure (XANES) – peaks that appear near or on the edge, usually within 30 eV of the edge.
4. Extended X-ray absorption fine structure (EXAFS), which is the oscillation above the edge, which is proportional to the amplitude of the scattered photo-electron at the absorbing atom.

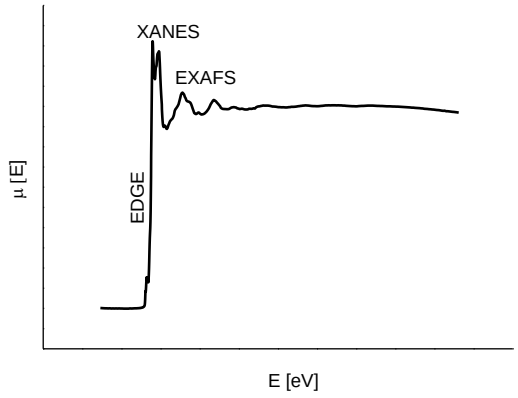

Fig. 1. 12 XAFS μ(E) for TiO_2 anatase with edge, XANES and EXAFS regions identified.

1.8.2. XANES

XANES is called a finger print of a material. Simply by comparing normalized XANES of an investigated material and the standard the sample and its structure can be identified. From XANES allows determining formal valence state, ligand type and the coordination environment, as the edge position and its shape depend on those parameters. Analysis technique called linear composition fit (LCF) based on linear combinations of known spectra from standard compounds allows quantification of ratios of valence states and/or phases. XANES can be collected at much lower concentrations than EXAFS, because it has much larger signal intensity. But its quantitative accuracy is much lower than that obtained from EXAFS.[156-158] **Fig. 1. 13** shows two XANES plots of two different phases of titania.

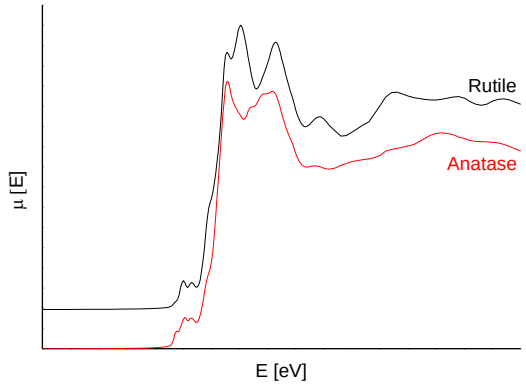

Fig. 1. 13 Ti K-edge of XANES of two TiO_2 phases- anatase and rutile.

1.8.3. EXAFS

A photon ejected from an atom interacts with core electrons of neighboring atoms constructive interference occurs. Those interferences lead to oscillations in energies above XANES and are defined as EXAFS, which can be described as a function $\chi(E)$.

$$\chi(E) = \frac{\mu(E) - \mu_0(E)}{\Delta\mu_0(E)} \tag{15}$$

where $\mu_0(E)$ is a background absorption coefficient of an isolated atom, $\mu(E)$ is the measured absorption coefficient and $\Delta\mu_0(E)$ is a difference measured at the threshold energy E_0.

If we assume that the ejected photoelectron is plane wave, then we can convert the X-ray energy to wavelength vector k, defined as:

$$k \equiv \frac{2\pi}{\lambda} \tag{16}$$

$$k = \frac{1}{\hbar}\sqrt{2m_e(E - E_0)} \tag{17}$$

where ħ is Plank's constant divided by 2 π, m_e is a mass of an ejected electron, E is a binding energy of the electron and E_0 is the threshold energy.

Because different neighbor atoms occur at different distances form the investigated atom, therefore they cause different frequencies in oscillations in $\chi(k)$. This phenomenon can be modelled according to the EXAFS equation, from which we can obtain distances, coordination number and the species of the neighboring atoms (18).

$$\chi(k) = \sum_j \frac{N_j f_j(k) e^{-2k^2\sigma_j{}^2}}{kR_j{}^2} \sin\left[2kR_j + \delta_j(k)\right] \tag{18}$$

where N is coordination number, $\delta(k)$ is a phase shift, $f(k)$ is the scattering amplitude, R is the distance between investigated atom and its neighbors, σ^2 is a disorder in the neighbor distance and j are the different scattering possibilities. Knowing the scattering amplitude $f(k)$ and the phase shift $\delta(k)$ allows the determination of N, R and σ^2. In order to fit the empirical data to the theoretical standards final state rule is applied where the calculations predict that the photoelectron had been removed from the absorbing atom and as a result ion is

allowed to reach a relaxed state but with the hole corresponding to the missing electron still present.[156-158]

Since EXAFS are the oscillations present above the XANES region, and not gradual trends, the analysis requires particular mathematical transformation first. In the case of XANES it is enough to normalize the data, for EXAFS further subtraction of the background results in obtaining χ in the function of energy $\chi(E)$. Next step is conversion of $\chi(E)$ to $\chi(k)$ using equation 17, resulting in the line resembling modulated sinusoid (**Fig. 1. 14**).

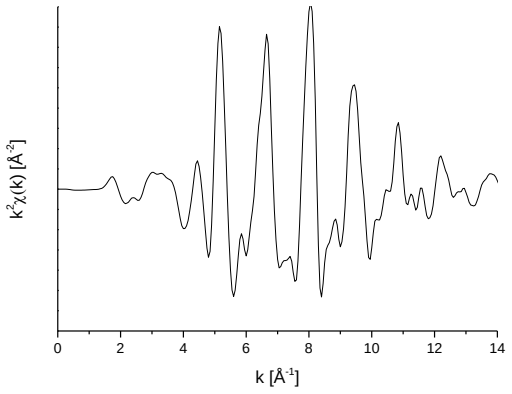

Fig. 1. 14 *$k^2\chi(k)$* for an iron metal foil.

The more disordered substance yields a less modulated sinusoid. **Fig. 1. 14** presents the $\chi(k)$ of highly oriented iron foil therefore the sinusoid is highly modulated. It happens as in an ordered crystal every atom has almost identical surroundings, not only in the near neighbor environment but also next-nearest neighbor and next-next-nearest neighbor and so on. As, according to the EXAFS equation (18), each individual term is a sinusoid, added the multiple sine waves of various amplitudes, phases and periods, the result resembles modulated sinusoid.

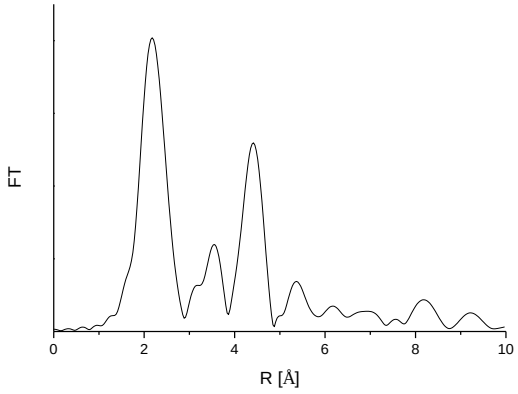

Fig. 1. 15 Magnitude of the Fourier transform of the data from figure 1.14.

Fig. 1. 15 shows the magnitude of Fourier transform of the data from **Fig. 1. 14**. As there are several shells of scattering atoms of metal foils that occur at well-defined distances they will have transforms possessing multiple peaks. The same process applied to the highly disordered material would yield a Fourier transform magnitude with one main peak. Fitting the peaks allows defining the precise distances between the investigated atom and its neighbours.

2. Synthesis and characterisation of niobium doped TiO_2 thin films by AACVD; photo-catalytic and transparent conducting oxide properties

2.1. Introduction

Niobium doped titania thin films are promising replacement of indium, tin and zinc based TCO's as described in **1.4.2**. Nb:TiO_2 with the required low resistivity to function as TCO material have been formed by pulsed laser deposition (PLD).[85] Theoretical studies have also indicated that niobium doped titania should be a good candidate for a TCO material. Bhachu *et al.*[99] have previously reported synthesis of niobium doped TiO_2 thin films *via* AACVD using titanium(IV) ethoxide and niobium(V) ethoxide as precursors and toluene as a solvent. Films described by them combined four functional properties (photocatalysis, electrical conductivity, optical transparency and blue colouration) within the same layer, making them a promising alternative to conventional TCO materials.[99] Although, in order to make this material compatible with the industrial scale glass manufacturing technology, the change of solvent is required. This chapter, describes synthesis of Nb:TiO_2 *via* AACVD using same precursors as described by Bhachu *et al.* but changing the solvent to hexane, and investigating its impact on TCO properties of material. In addition to traditional characterisation methods, XAFS studies on the different levels of niobium doped titania thin films and the effect of phase segregation on the electrical and optical properties of thin films are presented. The processing method employed included making an aerosol of precursors dispersed in a hexane mist. Such a solvent system is compatible with commercial glass manufacture. Furthermore the XAFS studies surprisingly show a presence of Nb_2O_5

component, confirmed by high resolution TEM analysis. The presence of this was undetectable by common characterisation techniques, including XRD and Raman. This work calls into question the actual solubility limit, reported in literature as 40% by mole fraction[68, 159, 160] of Nb in the anatase titanium dioxide lattice, at least as prepared by AACVD.

2.2. Experimental

2.2.1. Chemicals and substrates

All chemicals used in this experiment were purchased from Sigma Aldrich Chemical Co. and used without further purification; 2 g of technical grade titanium(IV) ethoxide, (0-10 atom.% Nb:Ti) 99.95% niobium(V) ethoxide, 25 mL of hexane. Nitrogen (oxygen free) was provided by BOC. The precursor flow was kept at 0.6 l/min. Deposition was carried on a 15 cm x 3.5 cm x 0.3 cm standard float glass coated with a 50 nm layer of SiO_2 to prevent ion migration from the glass[161] supplied by Pilkington NSG Group.

2.2.2. Material synthesis

Films were deposited in a cold wall reactor in the N_2 atmosphere, the temperature of the substrate was 500 °C during the entire deposition, and then cooled to room temperature.

2.2.3. Material characterisation

For identification of the crystal structure and preferred orientation growth of the film X-ray diffraction (XRD) was used. This was carried out on a *Bruker GADDS D8* diffractometer with a Cu Kα X-ray source and readings were taken over the $10° < 2\theta < 66°$ range. To confirm the phase of the film a *Reinshaw 1000 Invia* Raman spectrometer was used under ambient conditions with an Ar laser source (514.5 nm) over the 100-1500 cm^{-1} wavelength range. XAS spectra of as-deposited samples at the Nb (18990 eV) *K*-edges were taken at the B18 beamline of the Diamond Light Source. Obtained data was normalized and fitted using Athena and Artemis software and were calculated on the basis of anatase TiO_2 and Nb_2O_5 structures. Linear combination fit (LCF) of normalized XANES spectra was calculated with $Ti_{0.97}Nb_{0.03}O_2$ thin film and Nb_2O_5, as reference materials. To determine the structural parameters of investigated samples related to the niobium site, multiple shell fitting was carried out at the *k*-range 2.8 – 12.1 $Å^{-1}$, *R*-range 1.3 – 4 Å and *k*-weight equals 2. Transmittance- Reflectance (T-R) spectra were taken against an air background using a *Perkin Elmer Fourier Transform Lambda 950 UV-vis* spectrometer at a wavelength range of 200-2500 nm. Film thickness was derived from the transmittance spectrum *via Swanepoel's* method. Energy dispersive X-ray spectroscopy (EDX- obtained by using a *JEOL JSM-6301F Field Emission SEM*) was used to determine the Nb:Ti atomic ratio on the C-coated samples. Lattice structural information and EDX mapping were examined with *JEOL 2100 TEM*. Measurements of surface composition and the state of elements were carried out using a *Thermo Scientific K-Alpha* X-ray photoelectron spectrometer (XPS) with a monochromatic Al-Kα source. Results were then fitted using *CasaXPS* software with the binding energies suited to carbon (285 eV). *UV-vis* transmittance spectra were taken after irradiation with 365 nm light until complete decomposition of the dye. Charge carrier concentration (n /cm^{-3}), charge carrier mobility (μ /$cm^2\ V^{-1}\ s^{-1}$), bulk resistivity

(ρ /Ω cm) and sheet resistance (R_{sh} /Ω □$^{-1}$) were measured at room temperature on an *Escopia HMS-3000* set up in the Van der Pauw configuration. Measurements were carried out using a current of 1 μA and a 0.58 T permanent magnet on ≈ 1 x 1 cm squares with silver paint (Agar Scientific) used as ohmic contacts, integrity of which was tested prior to measurements.

2.2.4. Results

Aerosol assisted chemical vapour deposition (AACVD) of Nb-doped TiO_2 films was achieved on glass substrates from a mix of $Ti(OEt)_4$ and $Nb(OEt)_5$ in hexane at 500 °C. The as-deposited films were blue in colour and the intensity of the colour increased with niobium incorporation (**Fig. 2. 1**). All the films deposited uniformly on the glass plate, were adherent to the substrate, passing the Scotch tape test, were insoluble in common solvents and were stable in air for over a year.

$Ti_{0.97}Nb_{0.03}O_2$ $Ti_{0.92}Nb_{0.08}O_2$ $Ti_{0.77}Nb_{0.23}O_2$

Fig. 2. 1 Images showing niobium doped titania thin films deposited by AACVD image size is ca 2 cm by 3 cm. The photograph was taken against white background.

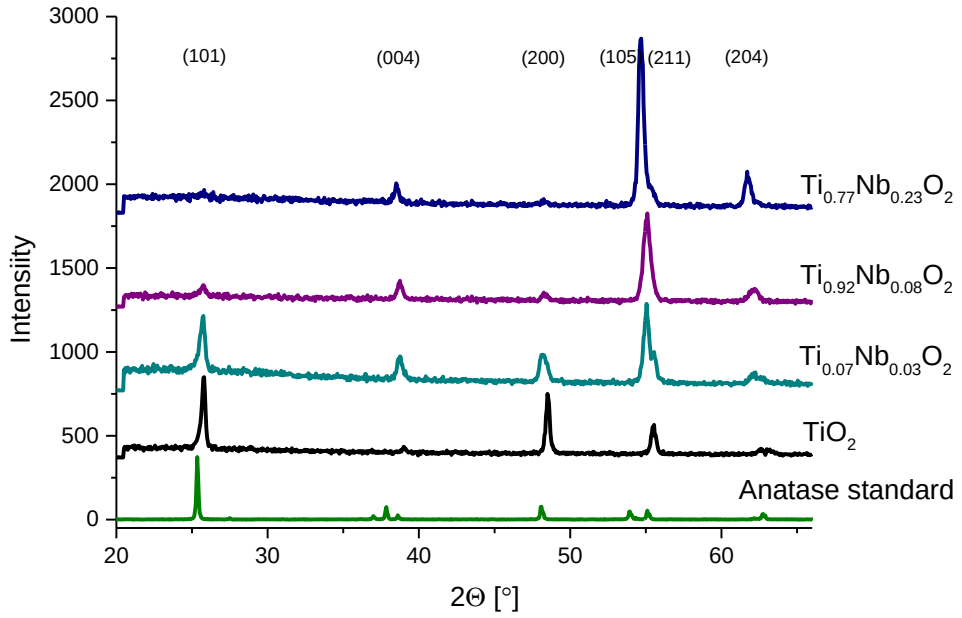

Fig. 2. 2 XRD pattern of Nb doped titania films prepared by AACVD at 500 °C on silica coated glass. The anatase reflection positions with appropriate values *(h k l)* are shown in brackets.

X-ray diffraction (**Fig. 2. 2**) showed that the only crystalline phase present in all the films is the anatase form of TiO_2. Surprisingly the XRD patterns reveal strong preferred orientation within the deposited films. In 0% Nb:TiO_2 the most intense reflection corresponds to the (1 0 1) plane, which decreases in intensity with niobium concentration in the initial starting solution. The apparent niobium concentration in the films also correlates with an increase in intensity of the (1 0 5) reflection. No other titania phases (brookite, rutile) were found neither could niobium oxide be observed in the XRD pattern or in the Raman spectrum (**Fig. 2. 3**). The Raman patterns were fully consistent with the formation of only the anatase form of TiO_2. Notably the peak at 143 cm^{-1} in pure anatase was shifted to higher energy with niobium doping (**Fig. 2. 4**), which was also observed by Fehse *et al.*[162] and was attributed to the change in O – Ti – O bending vibration. This is also consistent with previous studies based on W-doping into TiO_2.[163] In accordance with the work of Sheppard *et al.*[164] the titania lattice expands in direct proportion with the amount of niobium concentration in the film. The Raman

pattern peaks tend to become broader with niobium content. Despite this broadening, no niobium oxide phase could be detected by Raman.[165, 166]

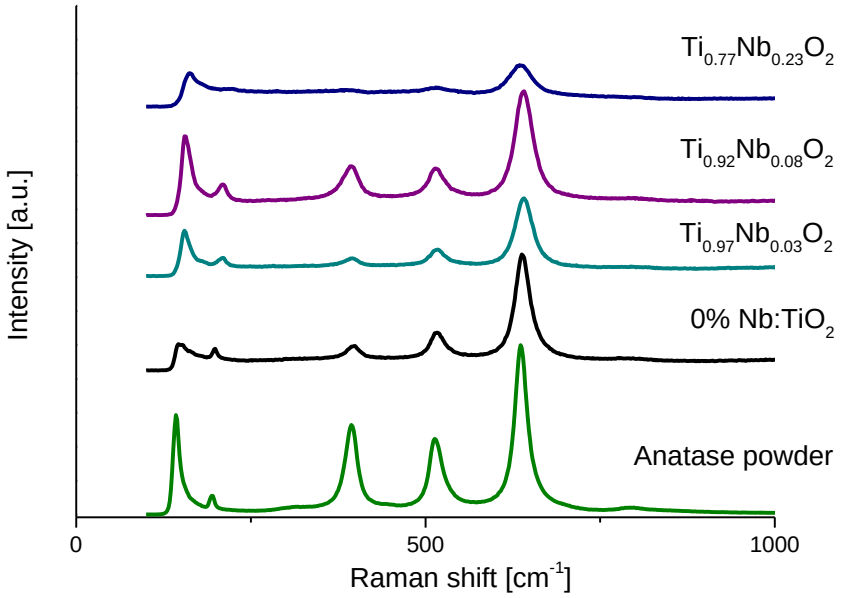

Fig. 2. 3 Raman spectra of anatase powder and as-deposited Nb doped titania films on silica coated glass.

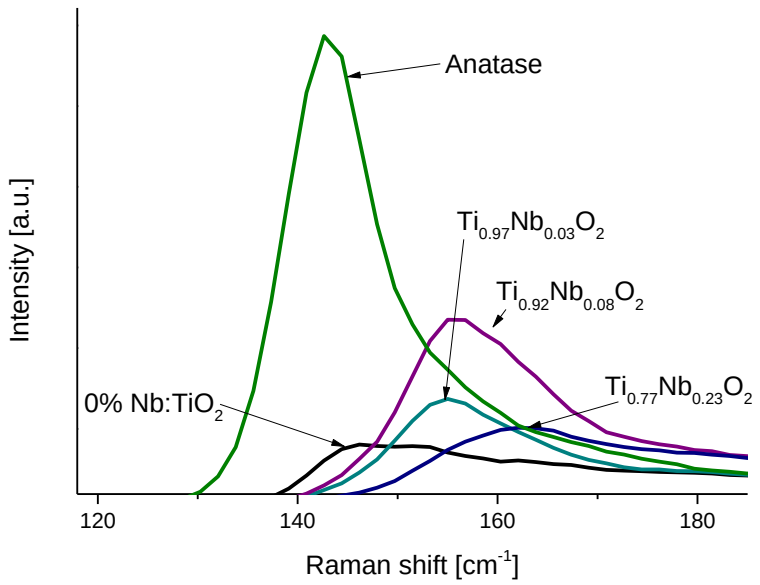

Fig. 2. 4 Shift of E_g band of niobium doped TiO_2 and pristine titania films formed from the AACVD compared to anatase powder.

Close TEM examination of each crystallites show that the d-spacing of most of them is consistent with anatase, except small nanocrystallites with d-spacing 3.08 ± 0.01 Å in the $Ti_{0.77}Nb_{0.23}O_2$ sample, which can be attributed to Nb_2O_5 (2 0 0). STEM elemental mapping (**Fig. 2. 5**) of both $Ti_{0.77}Nb_{0.23}O_2$ and $Ti_{0.97}Nb_{0.03}O_2$ show that niobium is mostly evenly distributed in the titania lattice and creates a solid solution. The fact that the Nb_2O_5 crystallites cannot be distinguished by XRD neither can be seen in the STEM elemental mapping might be due to their small size (sub 4 nm).

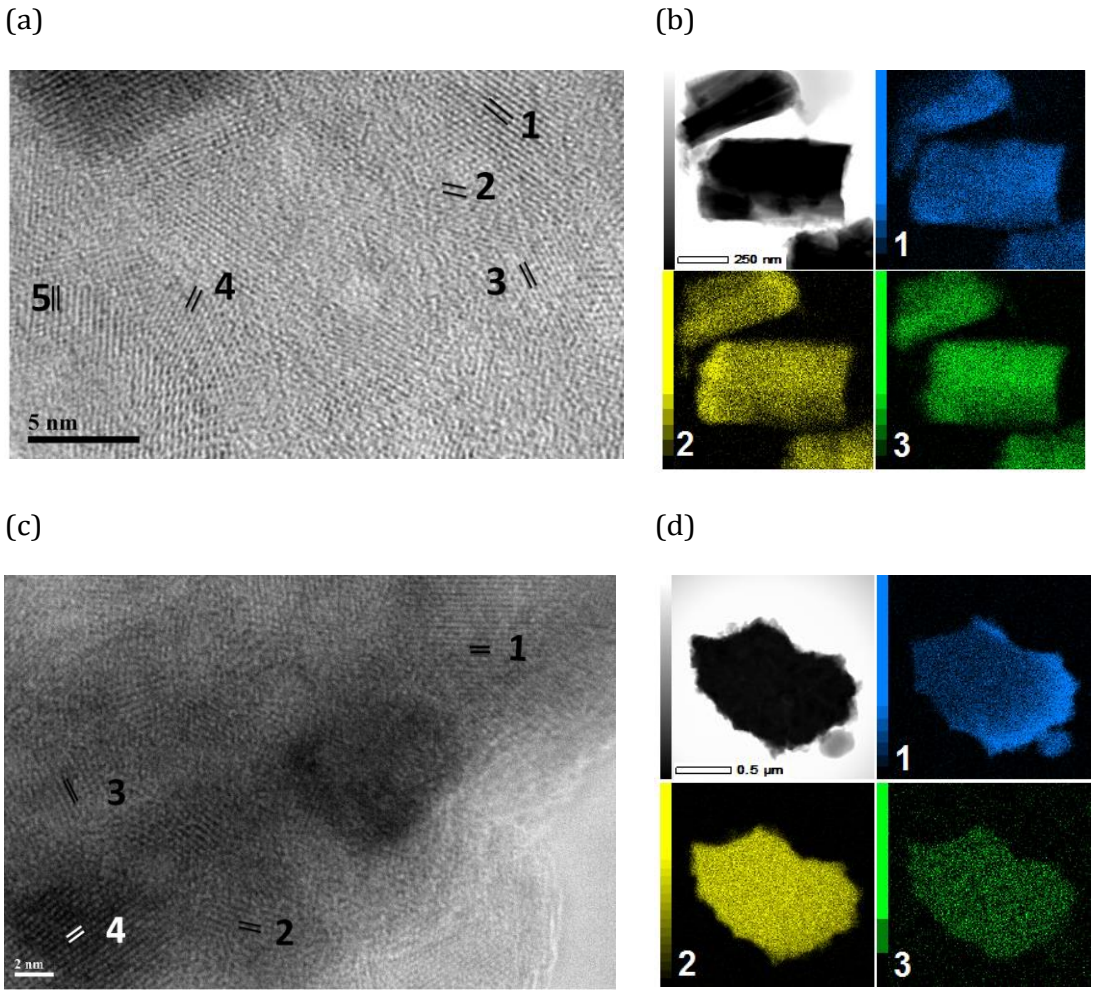

Fig. 2. 5 TEM picture of (a) $Ti_{0.77}Nb_{0.23}O_2$ (number 1 correlates to TiO_2 d_{101} = 3.55±0.01Å, 2- d_{112} = 2.34±0.02Å, 3- d_{004} = 2.38±0.01Å, 4- d_{103} = 2.43±0.01Å and 5 for Nb_2O_5 d_{200} = 3.08±0.01Å) (c) $Ti_{0.07}Nb_{0.03}O_2$ (number 1 correlates to TiO_2 d_{101}=3.55±0.01Å, 2- d_{112}=2.34±0.02Å, 3- d_{004}=2.38±0.01Å, 4- d_{105}=1.69±0.01Å), (b,d) corresponding elemental mapping of O-K (1), Ti-K (2) and Nb-L (3).

X-ray photoelectron spectroscopy was performed on all 4 samples (0, 1, 5, 10 mol.% Nb:TiO_2), both as surface scans and as depth profiles. For each sample the binding energy for the Ti $2p_{3/2}$ excitation varied between 458.7 and 459.4 eV, which corresponds with Ti^{4+} in TiO_2.[167] Niobium was detected at all levels in all samples. The binding energy for the Nb $3d_{5/2}$ excitation in all samples varied between 207.3 and 207.9 eV, which is representative of Nb^{5+} formation. The blue colouration of the as-deposited films suggests the presence of Ti^{3+} and Nb^{4+}, though the concentration of reduced species in all the samples was below the detection limit of XPS (*ca* 0-1 atom.%). Notably the XPS which was based on surface scans only showed one titanium and one niobium environment.

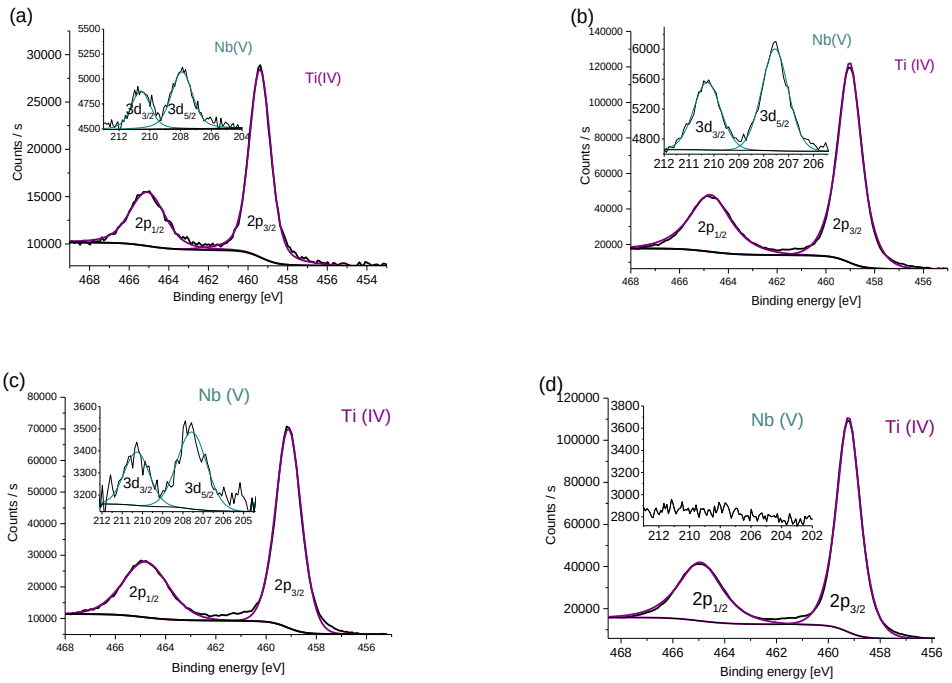

Fig. 2. 6 XPS spectra of as deposited (a) $Ti_{0.97}Nb_{0.03}O_2$ (b) $Ti_{0.92}Nb_{0.08}O_2$ (c) $Ti_{0.77}Nb_{0.23}O_2$ (d) pristine TiO_2 thin films in the titanium 2p region (inserts show niobium 3d region).

Nb K-edge XANES data are shown in **Fig. 2. 7**. Comparison of the XANES data of the films with Nb_2O_5 reveals that, while the edge positions are similar, the overall features appear to be different to that of Nb_2O_5. This suggests that niobium is in the 5+ oxidation state and possibly in two different coordination environments. The Nb K-

edge XANES spectra of $Ti_{0.97}Nb_{0.03}O_2$ and $Ti_{0.92}Nb_{0.08}O_2$ appears to be closely similar to the one reported earlier by Bhachu *et al.*[99] However, the features of the film containing higher amounts of Nb, in particular the shoulder at *ca* 18,985 and 19,019 eV were found to be between the low concentration samples and Nb_2O_5. This suggests that the attempt to increase the amount of Nb in the sample resulted, probably, in two phases with some amount of Nb_2O_5 present in the system. In order to estimate the amount of Nb_2O_5 in the samples, a LCF analysis procedure was used.

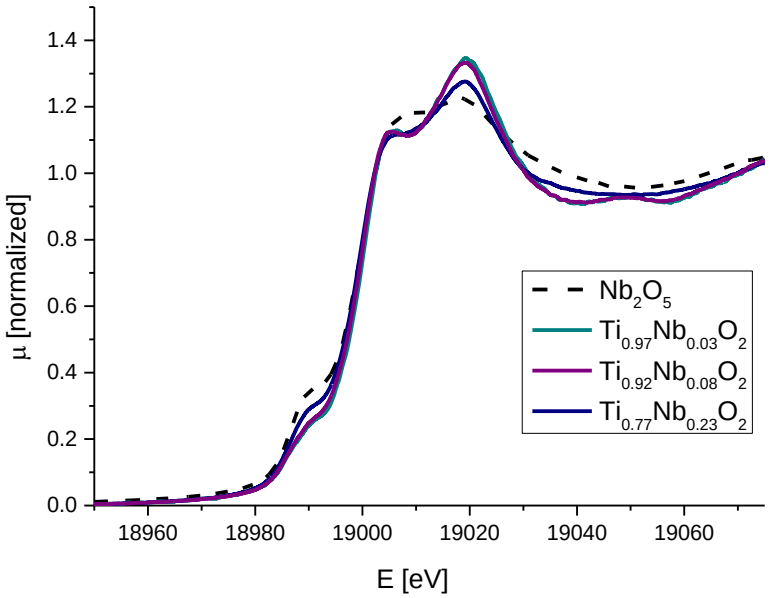

Fig. 2. 7 Normalised XANES Nb_2O_5, $Ti_{0.97}Nb_{0.03}O_2$, $Ti_{0.92}Nb_{0.08}O_2$ and $Ti_{0.77}Nb_{0.23}O_2$ thin films.

As there were no commercially available standard for niobium doped titania material it was assumed that $Ti_{0.97}Nb_{0.03}O_2$ is a complete solid solution (further proof for this can be seen in the analysis of the EXAFS data) and this therefore was used as one of the reference material and the other was the Nb_2O_5 standard.

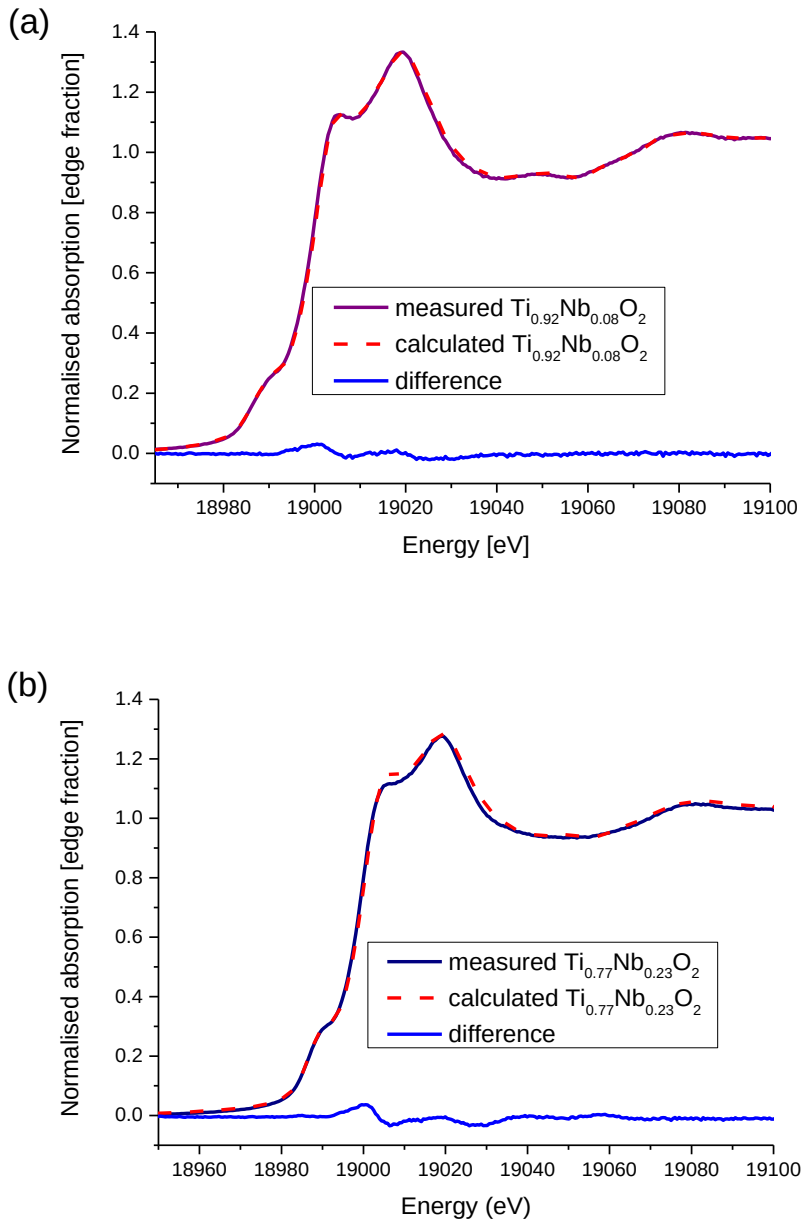

Fig. 2. 8 Normalised XANES spectrum along with linear combination of a) $Ti_{0.92}Nb_{0.08}O_2$ sample containing: 10.8 % Nb_2O_5 and 89.2 % as-deposited $Ti_{0.97}Nb_{0.03}O_2$ sample and b) $Ti_{0.77}Nb_{0.23}O_2$ sample containing: 48.4% of Nb_2O_5 and 51.6 % of as-deposited $Ti_{0.97}Nb_{0.03}O_2$ sample.

Results from XANES LCF (**Fig. 2. 8**) indicate the presence of two different phases in the as-deposited films. Both $Ti_{0.92}Nb_{0.08}O_2$ and $Ti_{0.77}Nb_{0.23}O_2$ films contain niobium doped anatase TiO_2 as well as Nb_2O_5. In the $Ti_{0.92}Nb_{0.08}O_2$ thin film 10.8% of the niobium doped in a form of Nb_2O_5. In $Ti_{0.77}Nb_{0.23}O_2$ thin film there is significantly more niobium(V) oxide phase and is estimated to be ca 48.6% of the niobium content.

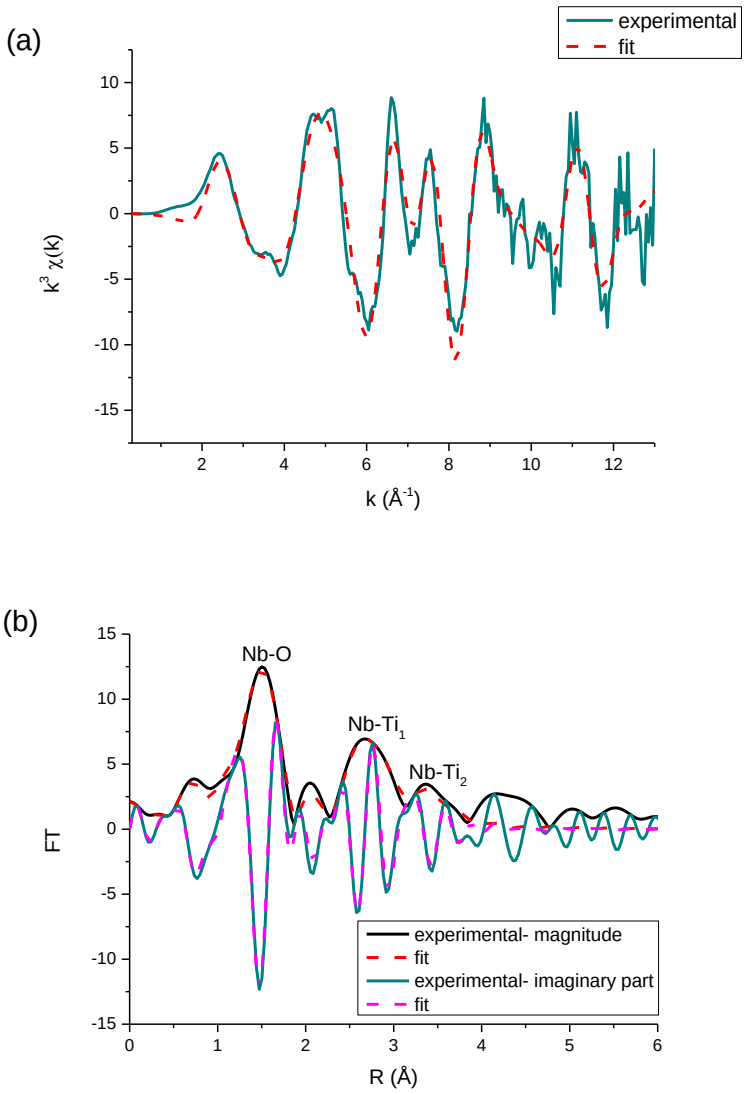

Fig. 2. 9 Nb K-edge EXAFS of $Ti_{0.97}Nb_{0.03}O_2$ thin film a) plot showing the $k^3\chi(k)$ b) plot showing the magnitude and imaginary part of the Fourier transform of the Nb K-edge EXAFS data of the $Ti_{0.97}Nb_{0.03}O_2$ thin film.

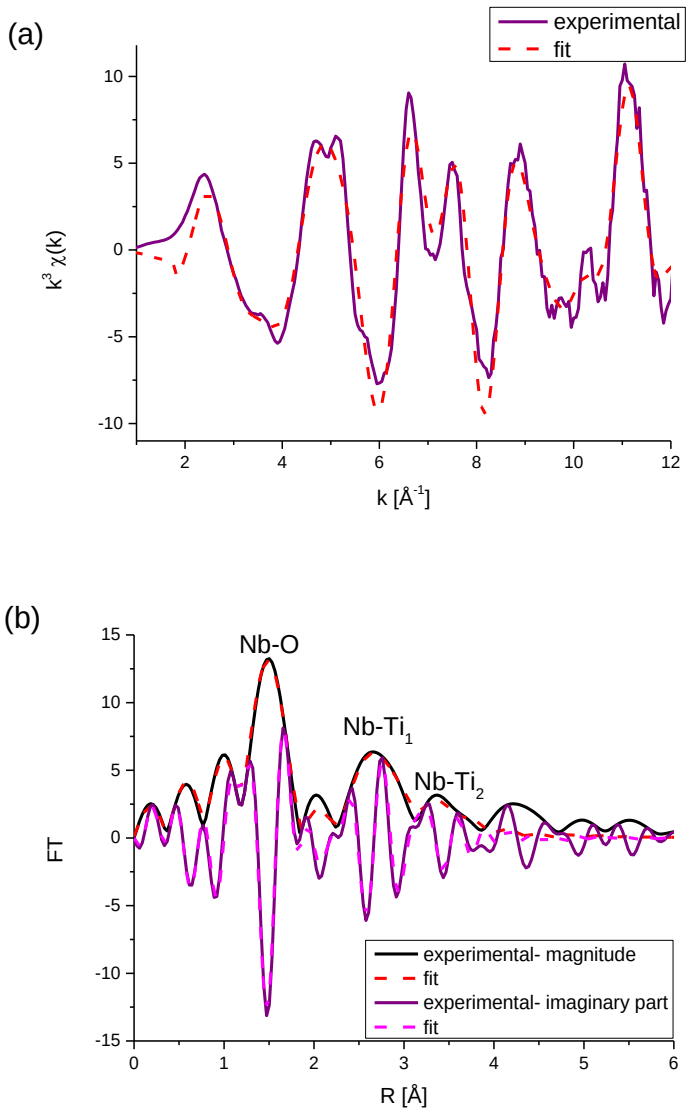

Fig. 2. 10 Nb K-edge EXAFS of $Ti_{0.92}Nb_{0.08}O_2$ thin film a) plot showing the $k^3\chi(k)$ b) plot showing the magnitude and imaginary part of the Fourier transform of the Nb K-edge EXAFS data of the $Ti_{0.92}Nb_{0.08}O_2$ thin film.

Table 1 Results of Nb *K*-edge EXAFS analysis. R-factor for $Ti_{0.97}Nb_{0.03}O_2$ = 0.0198, for $Ti_{0.92}Nb_{0.08}O_2$ = 0.0078 (N- coordination number, R- interatomic distance, σ^2- mean square relative displacement).

Sample	Nb O			Nb Ti_1			Nb Ti_2		
	R [Å]	N	σ^2 [Å]	R [Å]	N	σ^2 [Å]	R [Å]	N	σ^2 [Å]
$Ti_{0.97}Nb_{0.03}O_2$	1.98	2	0.001	3.13	4	0.004	3.85	4	0.007
$Ti_{0.92}Nb_{0.08}O_2$	1.99	2	0.001	3.13	4	0.005	3.86	4	0.009

In order to further establish the substitution of Nb in the Ti site, a detailed analysis was carried out of the EXAFS data. In pure anatase average interatomic distances of first, second and third neighbours around Ti ions are as follows: Ti–O 1.95 Å, Ti–Ti_1 3.04 Å and Ti–Ti_2 3.78 Å.[168] Similarly, in pure niobium (V) oxide the average distances of first, second and third neighbours around Nb ions are as follows: Nb–O 2.01 Å, Nb–Nb_1 3.39 Å and Nb–Nb_2 3.60 Å.[169] When niobium is incorporated into the anatase structure the Nb–O distances increase, as niobium has a larger ionic radius (0.064 nm) than titanium (0.0603 nm).[170] Nb K-edge EXAFS data were analysed to yield information about the first, second and third neighbours and they are presented in **Table 1**. For the first two samples ($Ti_{0.97}Nb_{0.03}O_2$ and $Ti_{0.92}Nb_{0.08}O_2$) distances the Nb–O distances are slightly larger compared to average Ti–O distance in Anatase TiO_2 (1.95 Å) and are Nb–O_1 1.98 Å for $Ti_{0.97}Nb_{0.03}O_2$ thin film and Nb–O_1 1.99 Å, for $Ti_{0.92}Nb_{0.08}O_2$ thin film. More importantly, the analysis resulted in Nb–Ti distances for the second and third neighbours of *ca* 3.13 Å and 3.85 Å for the two Nb doped TiO_2 films which are significantly different when compared with the structure of Nb_2O_5, which has second neighbour distances of *ca* 3.39 and 3.6 Å. Thus, the slight increase in Nb–O distances and short and long Nb–Ti second neighbour distances (which are similar to the one observed in TiO_2 anatase structure) suggest Nb ions occupy the Ti site in the anatase TiO_2 lattice; niobium is known to be highly soluble in titania[171] therefore it is expected to be evenly spread within the material. These distances are marked in the Fourier transform **Fig. 2. 9** and **Fig. 2. 10** (the data presented is not corrected for the phase shift, but the values given in the **Table 1** are phase-shift corrected).

Table 2 Comparison of % of niobium and titanium in the solution and in the film structure measured by EDX, XANES and XPS. (*note that in the absence of any Nb substituted TiO_2 as a model compound, $Ti_{0.97}Nb_{0.03}O_2$ was used as a reference)

Sample	$Ti_{0.97}Nb_{0.03}O_2$	$Ti_{0.92}Nb_{0.08}O_2$	$Ti_{0.77}Nb_{0.23}O_2$
At. % of Nb in the solution	1	5	10
At. % of Nb in the film (EDX)	3	8	23
At. % of Ti in the film (EDX)	97	92	77
At. % of Nb in the film (XPS)	0.7	1.5	1.0
At. % of Nb doped in the film, that turned into Nb_2O_5 (XANES)	-*	10.8	48.4

EDX analysis (**Table 2**) shows that the amount of niobium in the film is higher than the amount added to the solution. For 1 atom.% niobium in a solution, the amount incorporated into the film is 3 times higher and is 3 atom.%. For 5 atom.% niobium in the solution it is 1.5 times higher (8% niobium in a film structure) and for 10 atom.% niobium in a solution it is 23 atom.% of niobium in the film. The increase in niobium concentration in the films in comparison with its concentration in solution can be explained by the fact that during film formation, the molecules that undergo diffusion and desorption process are mostly associated with titania. While, the desorption and incorporation rate for titanium is higher, the incorporation rate for niobium species exceeds that of titania, mainly due to the creation of separate, Nb_2O_5 phase. The fact that XPS shows very low amounts of niobium on the surface of the film compared to EDX analysis confirms that most niobium is in the bulk and the Nb_2O_5 phase occurs mostly not on the surface but in between the doped titania crystals.

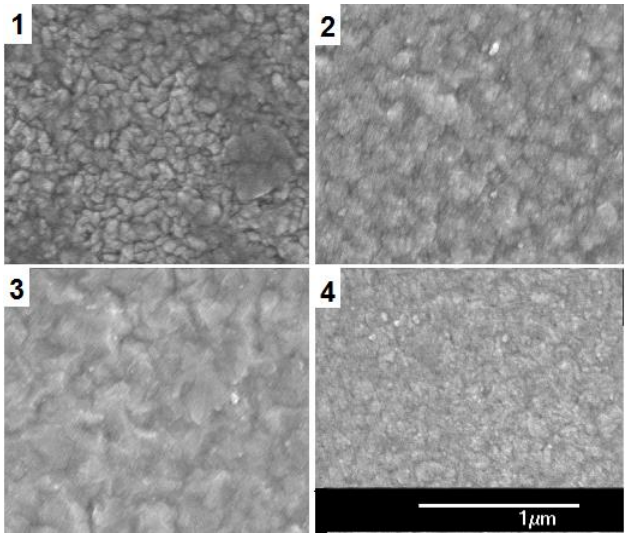

Fig. 2. 11 SEM picture of Nb:TiO_2 as-deposited thin films (1) $Ti_{0.97}Nb_{0.03}O_2$, (2) $Ti_{0.92}Nb_{0.08}O_2$, (3) $Ti_{0.77}Nb_{0.23}O_2$, (4) pristine TiO_2.

The morphology of the film surface changes with the niobium incorporation into the titania lattice (**Fig. 2. 11**). The surface of pristine TiO_2 thin films is an irregular aggregation of small, approximately 10 nm size units. The surface of as-deposited $Ti_{0.97}Nb_{0.03}O_2$ thin films is made of cone-like formations between 50 nm and 150 nm. $Ti_{0.92}Nb_{0.08}O_2$ thin film surface has much broader crystals than $Ti_{0.97}Nb_{0.03}O_2$ film (from about 200 nm to 500 nm) and the cones bases are joined. Further doping of titania with niobium causes a change of the surface structure and the as-deposited $Ti_{0.77}Nb_{0.23}O_2$ film loses its pointed structure for cauliflower like uneven agglomerations of size from about 200 nm to 400 nm made of 20 nm small units.

The thickness of the as-deposited films was derived from the oscillations in the *UV-vis* spectra by applying the *Swanepoel's* method,[172] which was possible due to the oscillations visible in a **Fig. 2. 12**. Thickness of the deposited films is consistent and varies between 1 and 1.5 μm.

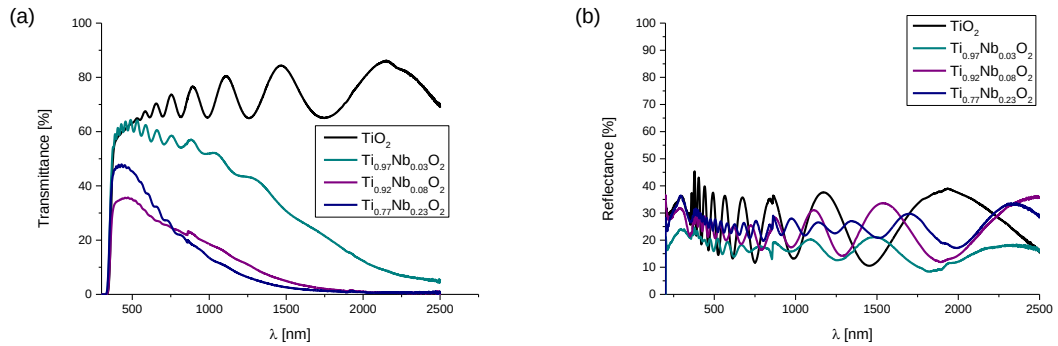

Fig. 2. 12 (a) transmittance and (b) reflectance (%) plot of as-deposited niobium doped titania thin films over the *UV-vis*-IR range.

From the *UV-vis* transmittance and reflectance data it can be seen that the transmittance of as-deposited films decreased in the visible region with dopant. Sample $Ti_{0.97}Nb_{0.03}O_2$ had 60% transmittance in *UV-vis* region and reached 0 % around 2500 nm, while $Ti_{0.92}Nb_{0.08}O_2$ and $Ti_{0.77}Nb_{0.23}O_2$ as- deposited films had respectively 35 and 47% transmittance in *UV-vis* region and reached 0% around 1500 nm. The reflectance profiles of all the investigated samples were similar and steady throughout all the spectrum at 20%. It should be noted that the blue films showed no change in colour appearance on *UV-vis* spectra after 6 months in air. The loss of colour requires heating to elevated temperatures (> 350 °C).

Indirect band gap for each film was determined via the Tauc plot using the $(\alpha h\nu)^{1/2}$ relation. The results increased from 3.19 eV for pristine anatase TiO_2, to 3.26 eV for $Ti_{0.97}Nb_{0.03}O_2$, 3.35 eV for $Ti_{0.77}Nb_{0.23}O_2$ and 3.36 eV for the $Ti_{0.92}Nb_{0.08}O_2$ thin film.

Table 3 Electrical properties of as-deposited niobium doped titanium dioxide thin films.

Sample	Charge carrier concentration [cm^{-3}]	Charge carrier mobility [$cm^2/V\ s$]	Bulk resistivity [Ω cm]	Resistance [kΩ/□]	Film thickness [μm]
$Ti_{0.97}Nb_{0.03}O_2$	4.59×10^{19}	3.01	0.12	0.84	1.1±0.2
$Ti_{0.92}Nb_{0.08}O_2$	1.23×10^{19}	10.3	0.06	0.12	1.5±0.3
$Ti_{0.77}Nb_{0.23}O_2$	2.84×10^{18}	18.9	0.15	0.24	1.1±0.2

The Hall effect studies (**Table 3**) on doped films showed that they display *n-type* conductivity as electrons are the prominent type of carrier species. 3 atom.% niobium doping into titania lowers sheet resistance to 0.84 kΩ/□, with the highest charge carrier concentration of all films (4.6×10^{19} cm^{-3}) but the lowest charge carrier mobility (3 cm^3/Vs). Sheet resistance and bulk resistivity were lowest for 8 % niobium doped films and were 0.16 kΩ/□ and 0.06 Ωcm respectively. Increasing the doping level to 23 % did not lead to a more conductive film, instead the charge carrier concentration was lowest of all the samples examined.

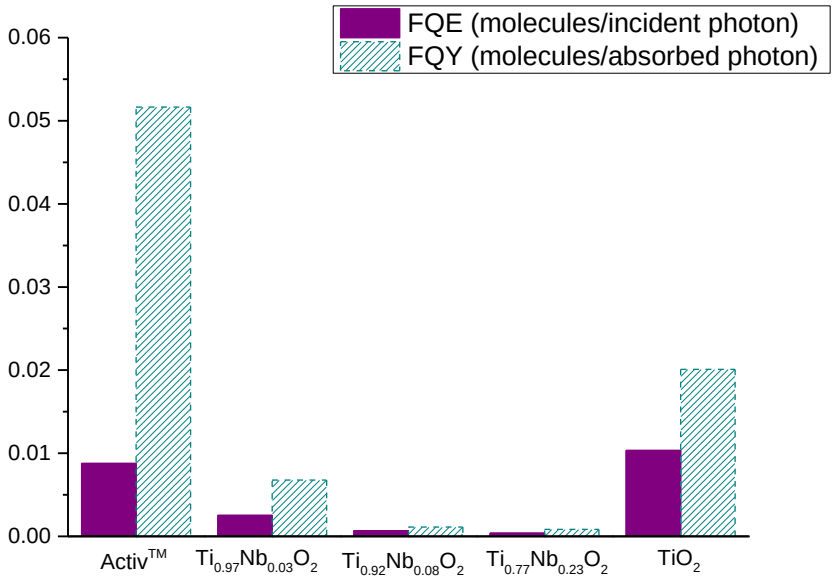

Fig. 2. 13 Comparison of formal quantum efficiency (FQE) and formal quantum yield (FQY) of as-deposited niobium doped TiO_2 thin films with Activ™.

The photo-catalytic properties of all the as-deposited samples were investigated using Rezazurin dye and the results were compared with the industry standard Pilkington Activ™. Photo-reduction of the dye was incited by the irradiation of the samples with 365 nm UV lamp with photon flux of 4.4 x 10^{14} photons cm^{-2} s^{-1} and checked using *UV-vis* spectroscopy over the range between 400 and 800 nm. Photo-reduction of the dye molecules was highest for pristine TiO_2 films prepared in this study at the rate of 3.9 x 10^{12} dye molecules cm^{-2} s^{-1}, followed by Activ™ (3.3 x 10^{12} dye molecules cm^{-2} s^{-1}. Degradation of the dye molecules on the as-deposited films was one order of magnitude lower than for the pristine TiO_2 thin film, showing a reduction with the increase of niobium concentration in the film at 9.6 x 10^{11}, 2.6 x 10^{11} and 1.5 x 10^{11} dye molecules cm^{-2} s^{-1} respectively for successively doped TiO_2.

Considering the UVA photon flux and photon absorption for all the samples the formal quantum efficiency (the FQE) – the number of molecules destroyed per incident photon, and formal quantum yield (the FQY) – the number of molecules destroyed per absorbed photon, were calculated. The best FQE was found in pristine TiO_2 (1.0 x 10^{-2} dye molecules per incident photon) followed by Activ™ (8.8 x 10^{-3} dye molecules per incident photon). Formal quantum yield was highest for pristine titania thin film (2.0 x 10^{-2} dye molecules per absorbed photon) but these measurements are still 2.5 times lower than for Activ™. The lowest photo-catalytic activity was demonstrated by both as-deposited $Ti_{0.92}Nb_{0.08}O_2$ and $Ti_{0.77}Nb_{0.23}O_2$ thin films.

2.2.5. Discussion

No previous work reports phase segregation in the bulk of as-synthetized Nb:TiO_2 material. As shown in the work of De Trizio *et al.*[165] there is no evidence of Ti^{3+} which is often present in reduced TiO_2.[171, 173, 174] The presence of niobium oxide as a second phase was detected on the surface of niobium doped titania as-synthetized

nanocrystals[175, 176] and on the surface and near-surface of the air annealed niobium doped titania thin films prepared by the sol-gel method[20] which was caused by a so called "self-purification" process occurring in most of the doped oxides during the post-treatment due to the mismatch in size of the metal cations.[175-177]

Both XRD and Raman analysis revealed the presence of only the anatase phase of TiO_2 which agrees with the work of Kafizas *et al.*[178] and Bhachu *et al.*[99] and confirms Hitosugi *et al's*[94] theory that the presence of niobium atoms as a dopant stabilises the anatase system and inhibits the growth of rutile.[176] Change of the preferred orientation agrees with the work of Bhachu *et al.* though the majority of publications report unchanged orientation with doping,[167, 168, 179] which suggests that preferred orientation of thin films depends not only on the amount of doping but also on the method of deposition. Annealing for 12 h in air at 500 °C results in largely insulating films, which is consistent with existing publications.[178, 180, 181]

The change in the surface morphology visible in SEM pictures was not previously reported, therefore it might be associated with change in the phase ratio, other than with the amount of niobium incorporated into the lattice.

A comparison of the results presented in this chapter with the work of Bhachu *et al.*[99] suggest that the impact of the structure lies not just between different methods of preparation as LPD, CVD or magnetron sputtering, but the influence on doped titanium dioxide's conductivity also have parameters such as temperature and solvents used for synthesis. Ok *et al.*[182] suggest that the reason for the higher than expected resistivity is that the grain boundaries in the titania lattice act as the charge carrier traps creating larger shifts in voltage thresholds for bias stress.

Niobium atoms should be evenly distributed within the TiO_2 lattice in order to obtain the highest possible electrical conductivity,[173] and as STEM elemental mapping shows niobium is largely homogenously dispersed in the titania particles as big as 0.25-0.5 μm. It was reported in the literature that the titania lattice can incorporate up to 20

atom.% of niobium ions[170, 180] and within that range forms a solid solution with anatase TiO_2, while the results obtained from XANES analysis (**Table 2**) prove that phase segregation occurs with much smaller amounts of dopant (for 5% Nb in the starting solution there is 10.8% of niobium(V) oxide in the bulk of the film). An alternative explanation is that the deposition by AACVD is under kinetic control and that two pathways exist – one that forms a Nb doped TiO_2 and another that forms a Nb_2O_5 phase with randomly dispersed crystals with size up to 5 nm, which are not detectable by standard resolution XRD nor Raman, but can be only seen on TEM pictures and after close EXAFS analysis. The temperature of the deposition might not be high enough for the diffusion of the niobium oxide into the titania lattice.

Incorporation of niobium into the lattice results in an increase of electrical conductivity, which is a result of extrinsic doping of the niobium ions into the titania. Substituting Ti^{4+} by aliovalent Nb^{5+} results in introducing additional charge carriers, that improve the bulk conductivity of titania. At the same time increasing phase segregation in the bulk therefore increasing the amount of Nb_2O_5 impedes any improvement in conductivity achieved by introducing niobium ions into the lattice (**Table 3**). This can be also seen in the bang gap correlations. Due to the Burstein-Moss effect electrons populate the conduction band, causing the optical bandgap to increase.[183, 184] The fluctuations in the band gap match variations in the electrical conductivity.

The increased amount of Nb_2O_5 is visible also in transmittance data. Both TiO_2 and Nb_2O_5 thin films are transparent and colourless. With Nb doping into the lattice, TiO_2 thin films become blue and loose transparency both in *UV-vis* and IR range. Though the transparency of $Ti_{0.92}Nb_{0.08}O_2$ is lower than $Ti_{0.77}Nb_{0.23}O_2$which suggest an increasing amount of Nb_2O_5 as a second phase present in the film, which also agrees with the results of the Hall effect measurements, EXAFS and TEM.

The results obtained from EXAFS and XANES spectra for $Ti_{0.97}Nb_{0.03}O_2$ and $Ti_{0.92}Nb_{0.08}O_2$ thin films are consistent with results published by Sacerdoti *et al.*[185] in their study about niobium doped titania thin films deposited by sol-gel and Arbiol *et al.*[177] in their study about niobium doped titania thin films deposited by induced laser pyrolysis. As both groups show in their study niobium in the titanium dioxide anatase lattice is in the 5^+ oxidation state, occupying distorted octahedral sites, indicated both by the EXAFS analysis and the main edge position in the XANES spectra, which is shifted towards higher energies with the respect to the absorption threshold of niobium foil.[185, 186]

2.2.6. Conclusion

Structural properties of niobium doped titanium dioxide films and their impact on electrical and optical properties were investigated. Films were deposited on silica coated glass substrates using aerosol assisted chemical vapour deposition at 500 °C. No visible phase segregation was found in XRD nor in Raman, though analysis of the Nb k-edge XANES and EXAFS as well at TEM pictures revealed the presence of niobium both incorporated into the titanium dioxide lattice as well as present in the form of the Nb_2O_5, which has an impact on the optical and electrical properties as the presence of niobium(V) oxide nanocrystals within titania ones increases resistivity of the film and increases its optical transparency. Since hexane as a carrier solvent in AACVD is compatible with industrial glass manufacture therefore the system we have developed could be used on an industrial scale. The XANES studies suggest that previous literature assignments of niobium doped TiO_2 should be treated with caution.

3. Structural and morphological changes in the Nb doped and undoped TiO_2 thin films deposited on FTO substrate *via* AACVD on FTO glass via AACVD.

3.1. Introduction

As shown in the chapter 2, deposition of niobium doped TiO_2 thin films on glass results in obtaining films of anatase phase. This chapter investigates the possibility of substitutional niobium doping into the rutile phase TiO_2 thin films and their properties. The epitaxial relationship between FTO and rutile phase of TiO_2 with a small lattice mismatch allows the nucleation and growth of the rutile phase of TiO_2 thin films as shown by Liu and Aydil.[118] Edusi,[187, 188] showed that using methanol in the AACVD synthesis has a controllable impact on the deposition chemistry and on the anatase/rutile TiO_2 ratio. By increasing the temperature of deposition from 400 °C to 550 °C the films changed from anatase at 400 °C to rutile with the minor presence of anatase at 550 °C. This chapter looks at combining both of the methods of growing rutile TiO_2 thin films order to obtain pristine and niobium doped rutile TiO_2 thin films. FTO glass was used as a substrate and MeOH or hexane were used as solvents in order to explore the influence of both substrate and solvent on the formation of the undoped and niobium doped TiO_2 thin films. As a result films with different morphologies and phase content were obtained, showing both the effect of FTO and MeOH or hexane on the chemistry of the film formation.

3.2. Experimental

3.2.1. Chemicals and substrates

All chemicals used in this experiment were purchased from Sigma Aldrich Chemical Co. and used without further purification; 1.2 g of technical grade titanium(IV) ethoxide or 1 g of technical grade titanium(IV) butoxide, (0-5 atom.% Nb:Ti) 99.95 % niobium(V) ethoxide, 20 ml of hexane or 20 ml of anyhydrous, 99.8 % methanol. Nitrogen (oxygen free) was provided by BOC. The precursor flow was kept at 0.6 l min^{-1}. Deposition was carried on 15 cm x 3.5 cm x 0.18 cm F: SnO_2 TEC Glass™ (13 Ω/□) supplied by Pilkington NSG group.

3.2.2. Material synthesis

Deposition of pristine and niobium doped TiO_2 thin films was carried out in the AACVD reactor. Films were deposited in a cold wall reactor in the N_2 atmosphere. The temperature of the substrate was either 500 or 550 °C during the entire deposition, and then cooled to room temperature.

3.2.3. Material characterisation

For identification of the crystal structure and any preferred orientation growth of the film X-ray diffraction (XRD) was carried out on the *Bruker GADDS D8* diffractometer with a Cu Kα X-ray source and readings were taken over the $10° < 2\theta < 66°$ range. Transmittance- Reflectance (T-R) spectra were taken against an air background using a SHIMADZU UV-3101PC *UV-vis-NIR* spectrometer at a wavelength range of 200-2500 nm. Film thickness was measured with *Scanning Electron Microscopy* (SEM) side images

of the films using a *JEOL JSM-6301F Field Emission SEM* at accelerating voltage of 5 keV, on Au-coated samples. SEM imaging was also used to determine film morphology. Energy dispersive X-ray (EDX) was used to determine the Sn:Nb:Ti atomic ratio on the C-coated samples. Measurements of surface composition and the state of the elements were carried out using a *Thermo Scientific K-Alpha* X-ray photoelectron spectrometer (XPS) with a monochromatic Al-Kα source. Results were then fitted using CasaXPS software with the binding energies calibrated to carbon (285 eV). Charge carrier concentration (n /cm^{-3}), charge carrier mobility (μ /cm^2 V^{-1} s^{-1}) and sheet resistance (R_{sh} /Ω □$^{-1}$) were measured at room temperature on an *Escopia HMS-3000* set up in the Van der Pauw configuration. Measurements were carried out using a current of 1 μA and 0.58 T permanent magnet on ≈ 1 x 1 cm squares with the silver paint (Agar Scientific) used as ohmic contacts, where integrity was tested in prior measurements.

3.3. Results

Several films were obtained and this chapter focuses on characterisation of 5 films, described by the precursor, solvent and temperature used in the synthesis:

- $Ti(OBu)_4$ – MeOH – 550 °C – 1 g of titanium(IV) butoxide in 20 mL of methanol deposited over FTO glass at 550 °C,
- $Ti(OBu)_4$ – MeOH – 500 °C – 1 g of titanium(IV) butoxide in 20 mL of methanol deposited over FTO glass at 500 °C,
- $Ti(OBu)_4$ – $Nb(OEt)_5$ – MeOH – 550 °C – 1 g of titanium(IV) butoxide and 5 atom.% of niobium(V) ethoxide in 20 mL of methanol deposited over FTO glass at 550 °C,
- $Ti(OEt)_4$ – hex – 500 °C – 1.2 g of titanium(IV) ethoxide in 20 mL of hexane deposited over FTO glass at 500 °C,
- $Ti(OEt)_4$ – $Nb(OEt)_5$ – hex – 500 °C – 1.2 g of titanium(IV) ethoxide and 5 atom.% of niobium(V) ethoxide in 20 mL of hexane deposited over FTO glass at 500 °C.

3.3.1. $Ti(OBu)_4$-MeOH-550 °C

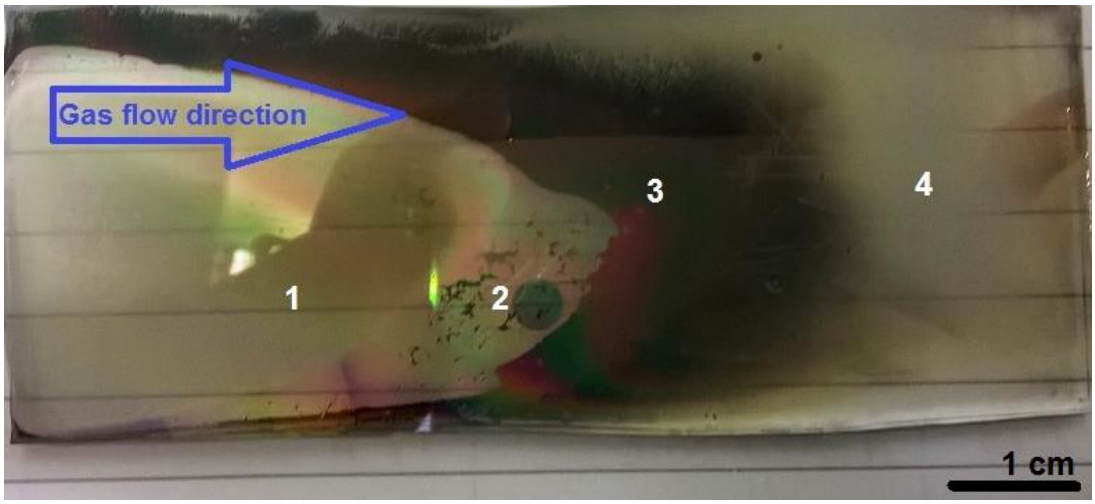

Fig. 3. 1 Picture of a film formed by AACVD of $Ti(OBu)_4$-MeOH at 550 °C.

AACVD deposition of $Ti(OBu)_4$ dissolved in MeOH at 550 °C resulted in a film with 4 distinctive parts (marked 1, 2, 3 and 4 on **Fig. 3. 1**). While parts 1 and 4 were robust and passed the Scotch tape test, parts 2 and 3 could be easily scratched or wiped. Turning the substrate 180° revealed that under the black surface of part 3 there was a metallic continuous film.

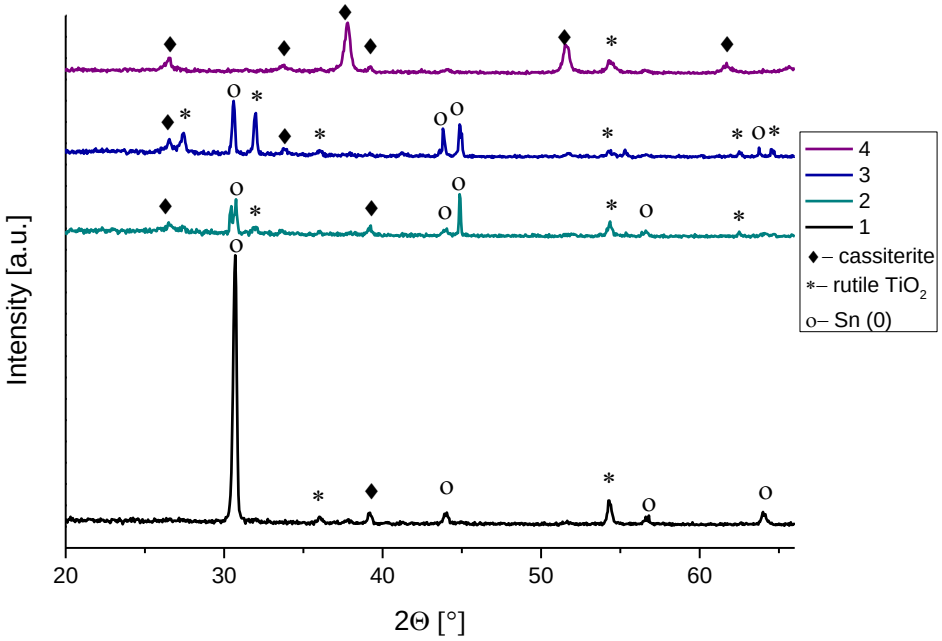

Fig. 3. 2 XRD patterns of the four parts of the thin film formed by AACVD of $Ti(OBu)_4$-MeOH at 550 °C. The rutile phase of TiO_2, cassiterite phase of SnO_2 and Sn(0) phases were marked.

X-ray diffraction showed that each of the parts contained mixed phase of metallic tin (β-Sn), cassiterite phase of SnO_2 and the rutile phase of TiO_2. Parts 1, 2 and 3 consisted of all 3 phases of varying intensities of the relevant peaks, suggesting a change both in the phase ratio as well as in the preferred orientation. The XRD pattern of part 4 matched the pattern of FTO film used as a substrate, with only a minor presence of rutile TiO_2.

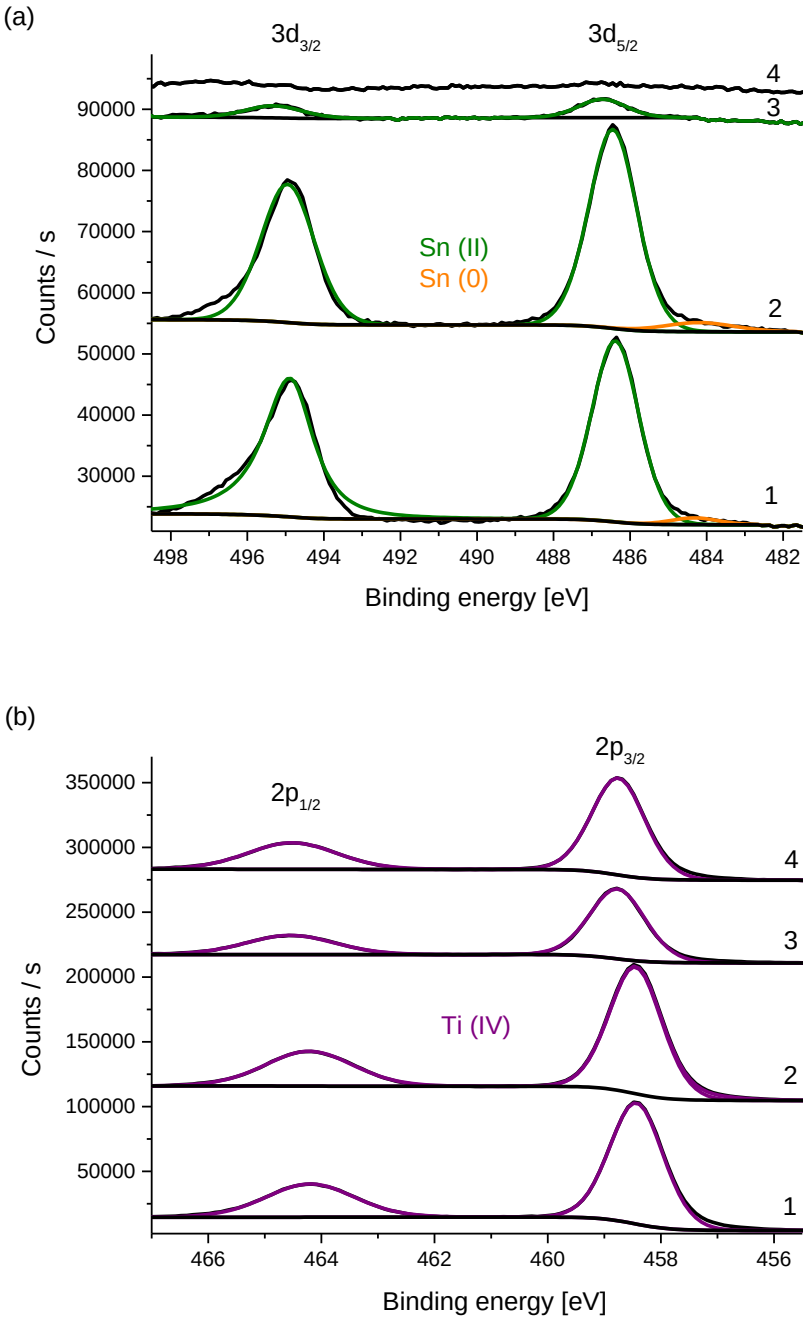

Fig. 3. 3 XPS spectra of film formed by AACVD of $Ti(OBu)_4$-MeOH at 550 °C showing (a) tin in the 3d region (b) titanium in the 2p region.

XPS surface scans were performed on all of the parts. In all of the scans Sn(IV) and Ti(IV) were detected (binding energies for Sn $3d_{5/2}$ and Ti $2p_{3/2}$ excitation are shown in the **Table 4**). The presence of tin in the surface scan can be explained by the cation migration during the CVD process. Tin at 0 oxidation state was detected only in parts 1 and 2. **Fig. 3. 3** shows a decrease in the amount of tin in the surface, even though the

amount of titanium was similar in parts 1, 2 and 4 and decreased in the part 3. The almost full decrease of tin in part 4 suggests coverage of FTO glass with rutile TiO_2 film. The fluorine was not detected in any of the scans.

Table 4 Results of the XPS analysis, showing the binding energies of Ti, Sn and Nb, electrical properties, atomic % ratio measured by EDX and film thickness of the thin film formed by AACVD of $Ti(OBu)_4$-MeOH at 550 °C.

	Binding energy [eV]			Hall effect measurements			EDX atomic % ratio		Film thickness [μm]
	Ti^{4+} $2p_{3/2}$	Sn $3d_{5/2}$		Charge carrier concentration [cm^{-3}]	Charge carrier mobility [$cm^2\ V^{-2}\ s^{-1}$]	Resistance [$\Omega\ \square^{-1}$]	Ti	Sn	
		Sn^{4+}	Sn^0						
1	458.4	486.6	484.3			> 1 M	1	7	0.6 ± 0.05
2	458.7	486.6	484.3			> 1 M	1	6	0.15 ± 0.02
3	458.8	486.7	-	1.3×10^{17}	854	0.6	1	1	1 ± 0.1
4	458.8	-	-			> 1 M	1	5	2.5 ± 0.1

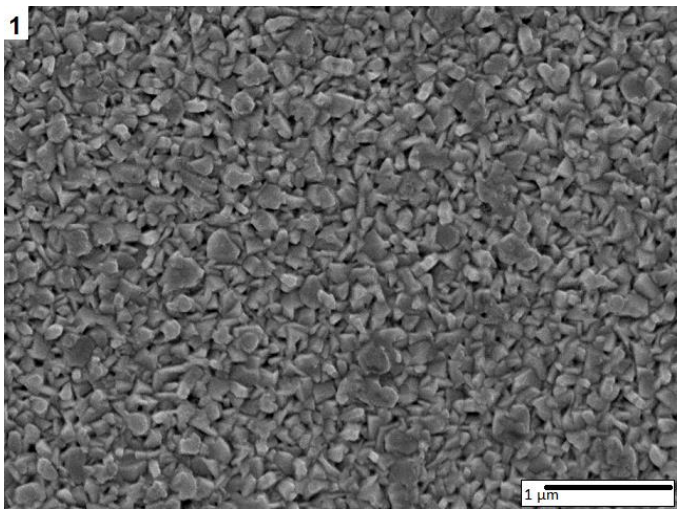

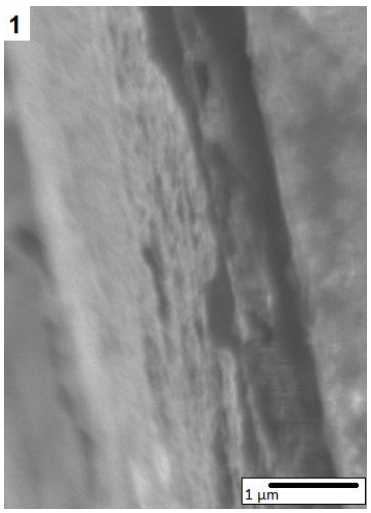

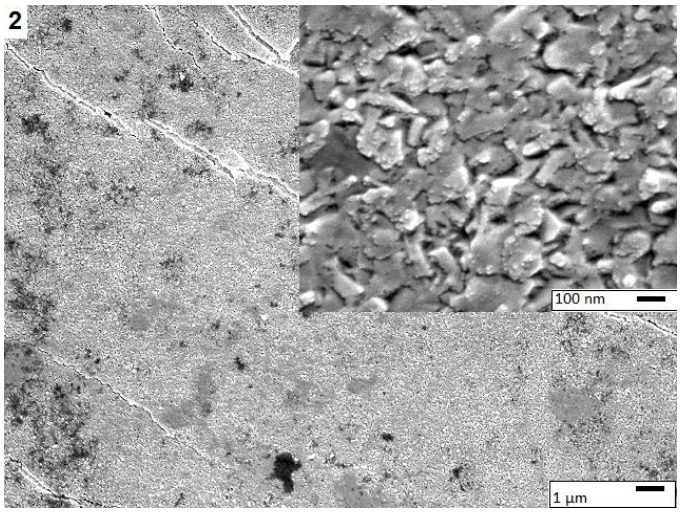

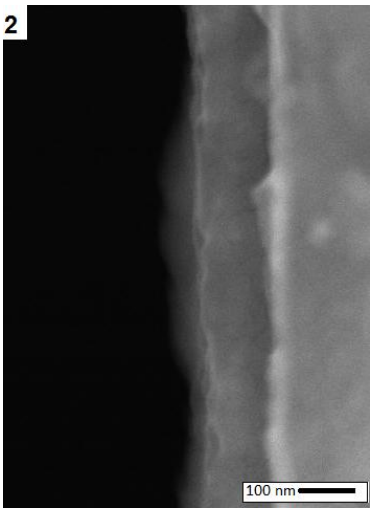

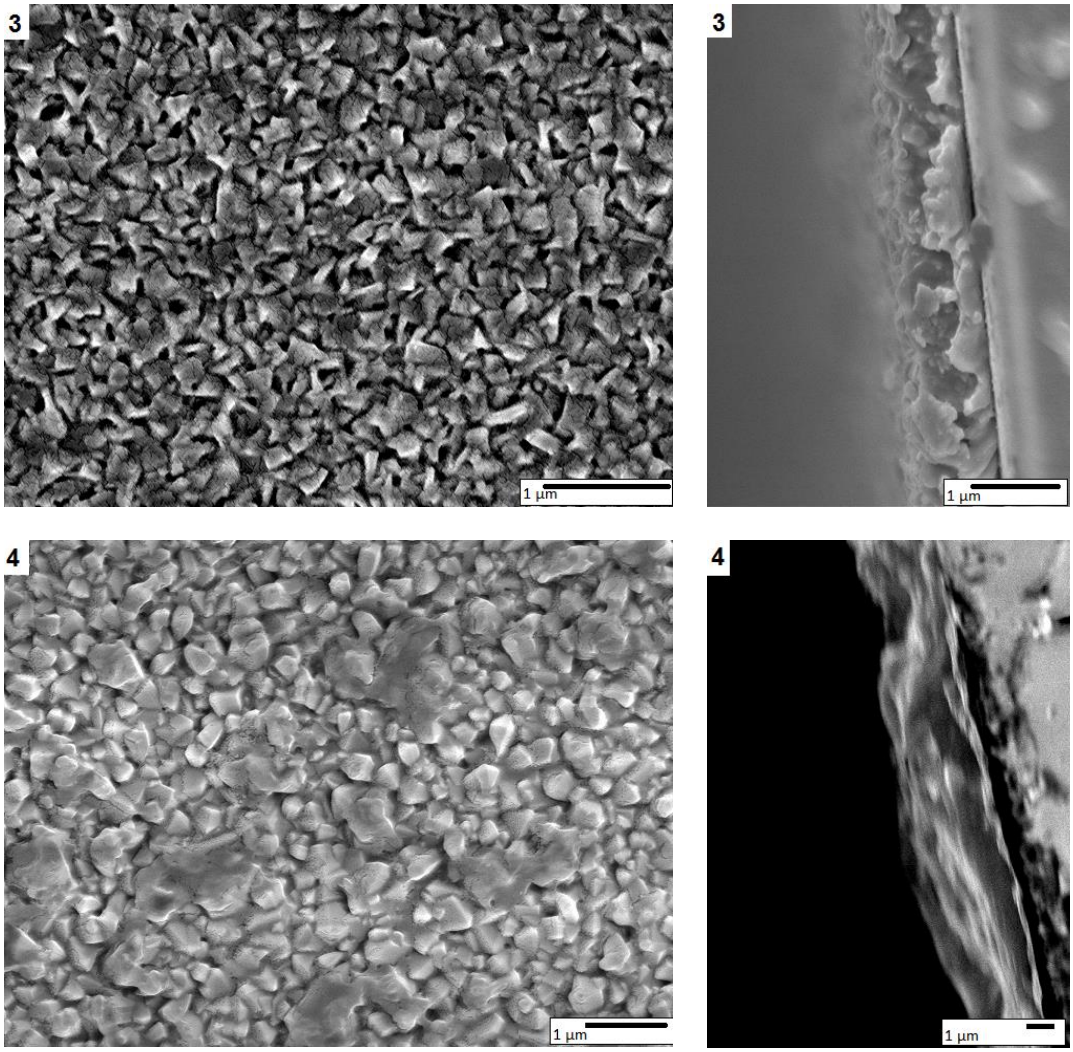

Fig. 3. 4 SEM pictures showing changes in the morphologies of the different parts of the thin film formed by AACVD of $Ti(OBu)_4$-MeOH at 550 °C. Numbers refer to those marked in **Fig. 3. 1**.

SEM micrographs of all 4 parts show variation in the film morphology progressing along with the changes in the deposition. The morphology of parts 1 and 4 was similar to the TiO_2 morphology reported by Mills *et al.* and Ponja *et al.*[189, 190] consisting of similar shaped particles of *ca.* 30-50 nm. This indicates that film is uniformly coated by the TiO_2 phase with the tin acting as either a dopant or a secondary phase, as identified by the EDX (Sn:Ti atomic ratio in part 1 is 1:6 and in part 4 1:5). The SEM side-on pictures show that films are uniform and polycrystalline, instead of the expected two distinctive layers of first FTO and then TiO_2. SEM of the part two shows how easily scratched and damaged the surface is, and the morphology of the particles indicates

that they are in the nucleating state, confirmed by the film thickness of 150 nm. The Sn:Ti atomic ratio of part two is 1:6. The 3rd part of the film is uniformly covered by the 1 μm thick film composed of mixed oxide with the atomic ratio Sn:Ti 1:1. Both side and top pictures indicate that this part is also polycrystalline with only one layer of film, composed of irregular, sharp facets.

UV-vis spectra of all the 4 parts are shown in the **Fig. 3. 5** and each part was compared with the *UV-vis* profile of the host FTO substrate used for this synthesis (solid lines show data of a sample, dotted lines show *UV-vis* profile of FTO glass). The reflectance profile of all the four parts looked similar in the 200 – 1000 nm region matched the FTO profile, then rises to 50% in the 1200 – 2000 nm region. Parts 1 and 4 were not transitive in the 200 – 500 nm region, after which the transmittance raised to 45% in the 700 – 1500 nm region, followed by the steady fall in the far IR region. Transmittance of part 2 grew from 300 nm up to 50% and remained around this level throughout the whole measured spectrum. Part 3 did not transmit light, most likely due to the metallic nature of the film.

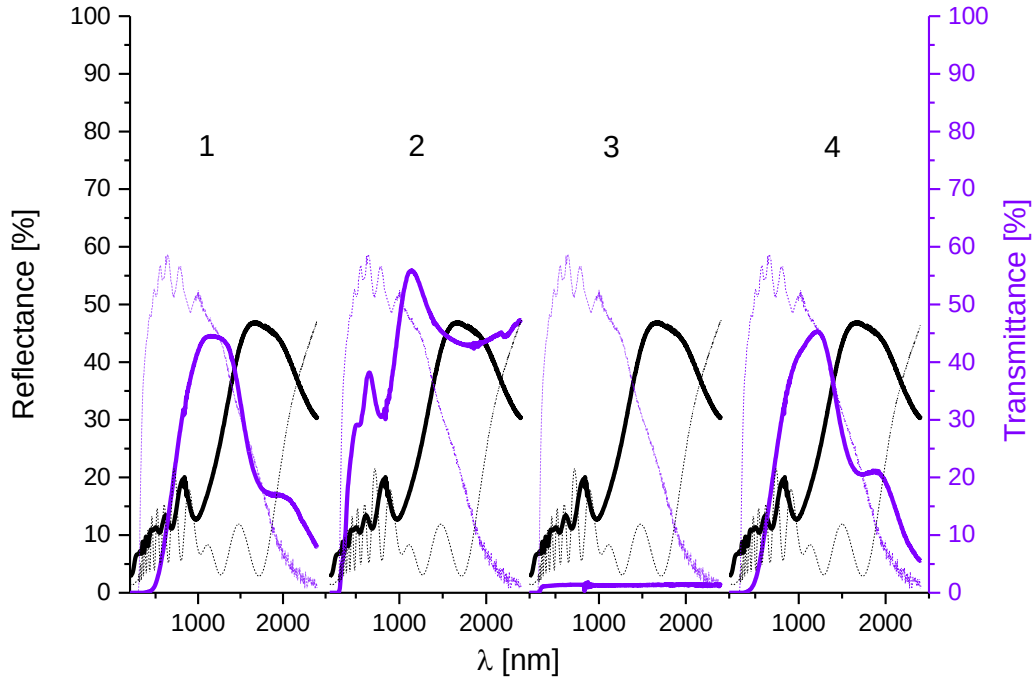

Fig. 3. 5 *UV-vis* spectra of the thin film formed by AACVD of $Ti(OBu)_4$-MeOH at 550 °C. Dotted lines show spectra of FTO glass.

Hall effect measurements confirmed that in part 3 of the film FTO was reduced to the metallic tin and formed a metallic continuous film as the resistance of 0.6 Ω/□ and charge carrier mobility of 854 cm^2/V s are characteristic values for metals.[191] The remaining parts showed conductivity above 1 MΩ, which does not allow for Hall Effect measurements.

3.3.2. $Ti(OBu)_4$-MeOH-500 °C

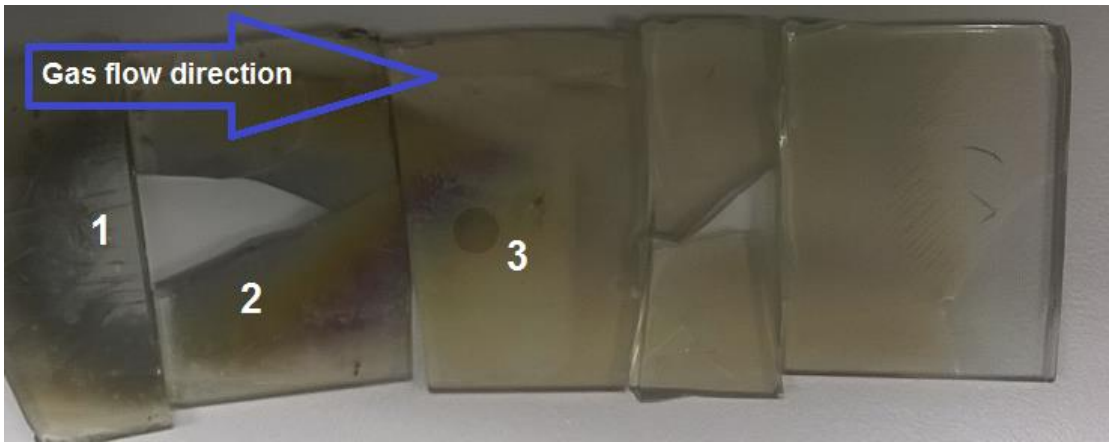

Fig. 3. 6 Picture of a film formed by AACVD of $Ti(OBu)_4$-MeOH at 500 °C.

Decreasing the deposition temperature by 50 °C resulted in the film consisting of 3 different parts (**Fig. 3. 6**). Part 1 revealed a mirror like metallic continuous film similar to part 3 of $Ti(OBu)_4$ – MeOH – 550 °C thin film, which was also soft and easily scratched and wiped. Parts 2 and 3 passed the Scotch tape test.

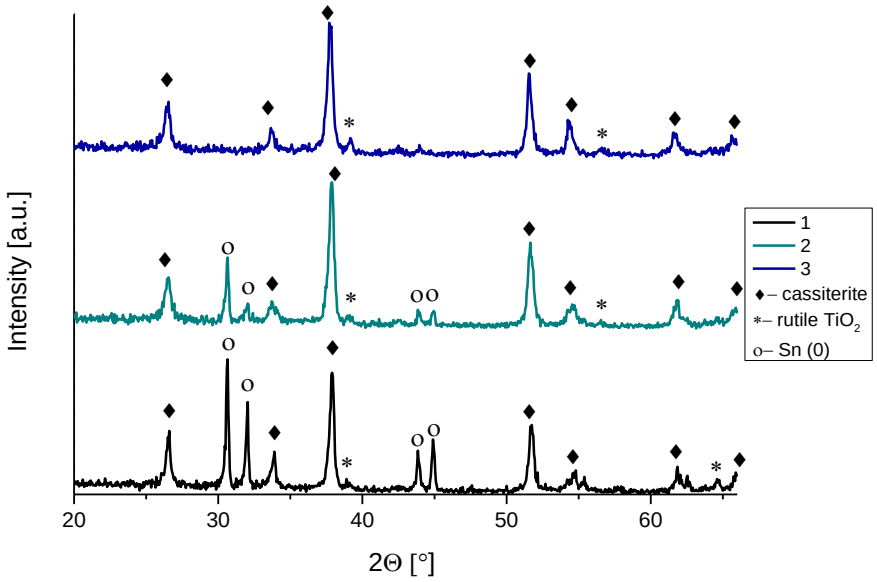

Fig. 3. 7 XRD patterns of the three parts of a film formed by AACVD of $Ti(OBu)_4$-MeOH at 500 °C. The rutile phase of TiO_2, cassiterite phase of SnO_2 and Sn(0) phases are marked.

XRD analysis showed that parts 1 and 2 consisted of both metallic tin and cassiterite phase of SnO_2 phases, while the pattern of part 3 matched the cassiterite phase of SnO_2. All 3 parts showed minor presence of the rutile phase of TiO_2.

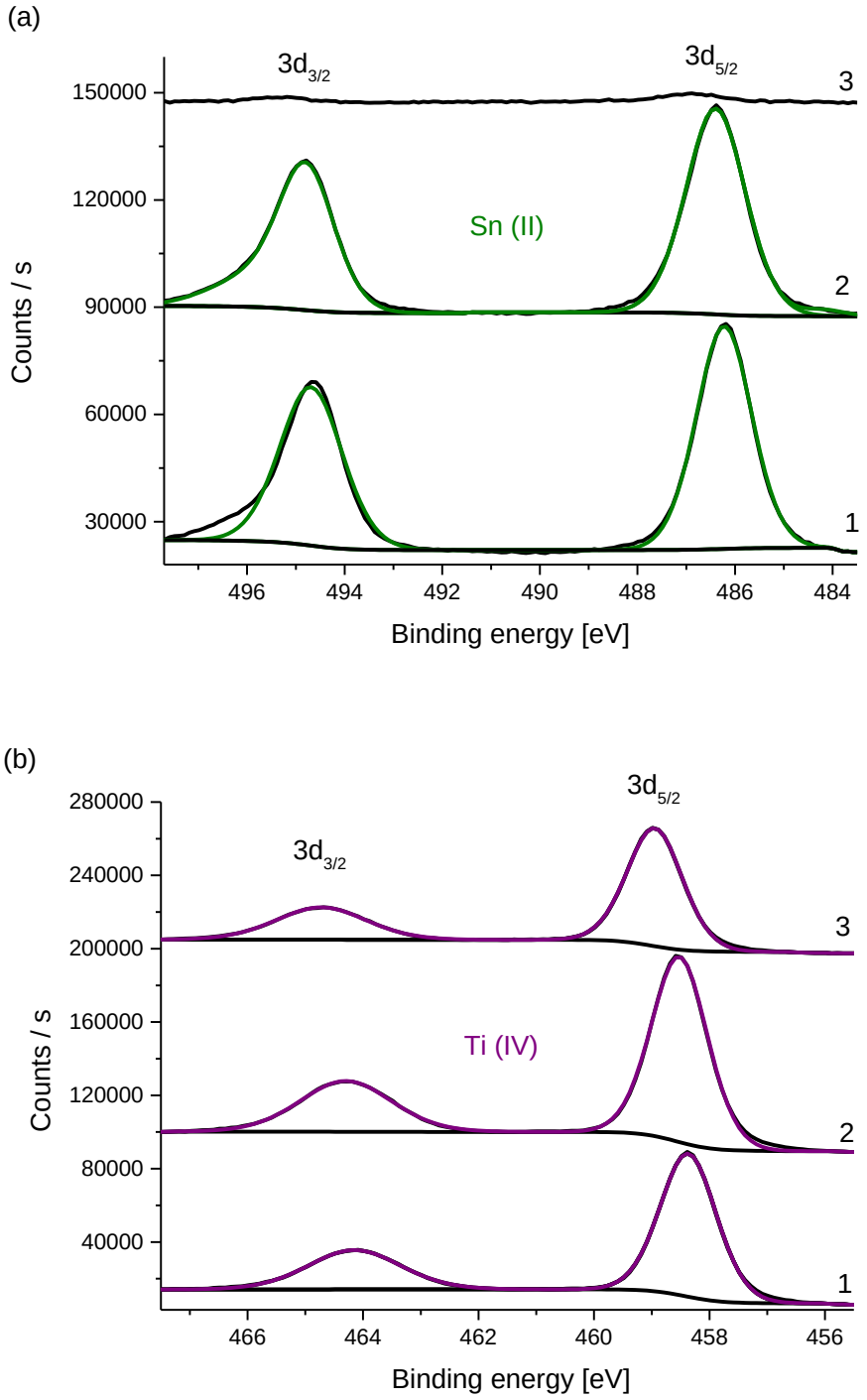

Fig. 3. 8 XPS spectra of a film formed by AACVD of $Ti(OBu)_4$-MeOH at 500 °C showing (a) tin in the 3d region (b) titanium in the 2p region.

XPS was performed on all the parts, revealing that the surface of the film contains no Sn (0) in any of the parts. For parts 1 and 2 the binding energy for the Ti $2p_{3/2}$ excitation varied between 458.4 and 458.8 eV which corresponds with the Ti^{4+} in TiO_2. Tin was detected only in parts 1 and 2 with the binding energy for Sn $3d_{5/2}$ excitation of 486.2 and 486.3 eV respectively, corresponding with the Sn^{4+} in SnO_2.[192]

Table 5 Results of the XPS analysis, showing the binding energies of Ti, Sn and Nb, atomic % ratio measured by EDX, electrical properties and film thickness of the film formed by AACVD of $Ti(OBu)_4$-MeOH at 500 °C.

	Binding energy [eV]			Hall effect measurements			EDX atomic % ratio		Film thickness [μm]
	Ti^{4+} $2p_{3/2}$	Sn $3d_{5/2}$		Charge carrier concentration [cm^{-3}]	Charge carrier mobility [$cm^2 V^{-2} s^{-1}$]	Resistance [$\Omega \square^{-1}$]	Ti	Sn	
		Sn^{4+}	Sn^0						
1	458.4	486.2	-	1.1×10^{15}	1.4	3.9×10^3	1	6	0.4 ± 0.2
2	458.4	486.3	-	2.7×10^{17}	0.2	112.8	1	4	0.3 ± 0.09
3	458.8	-	-	1.5×10^{17}	2.5	15	1	2	0.4 ± 0.1

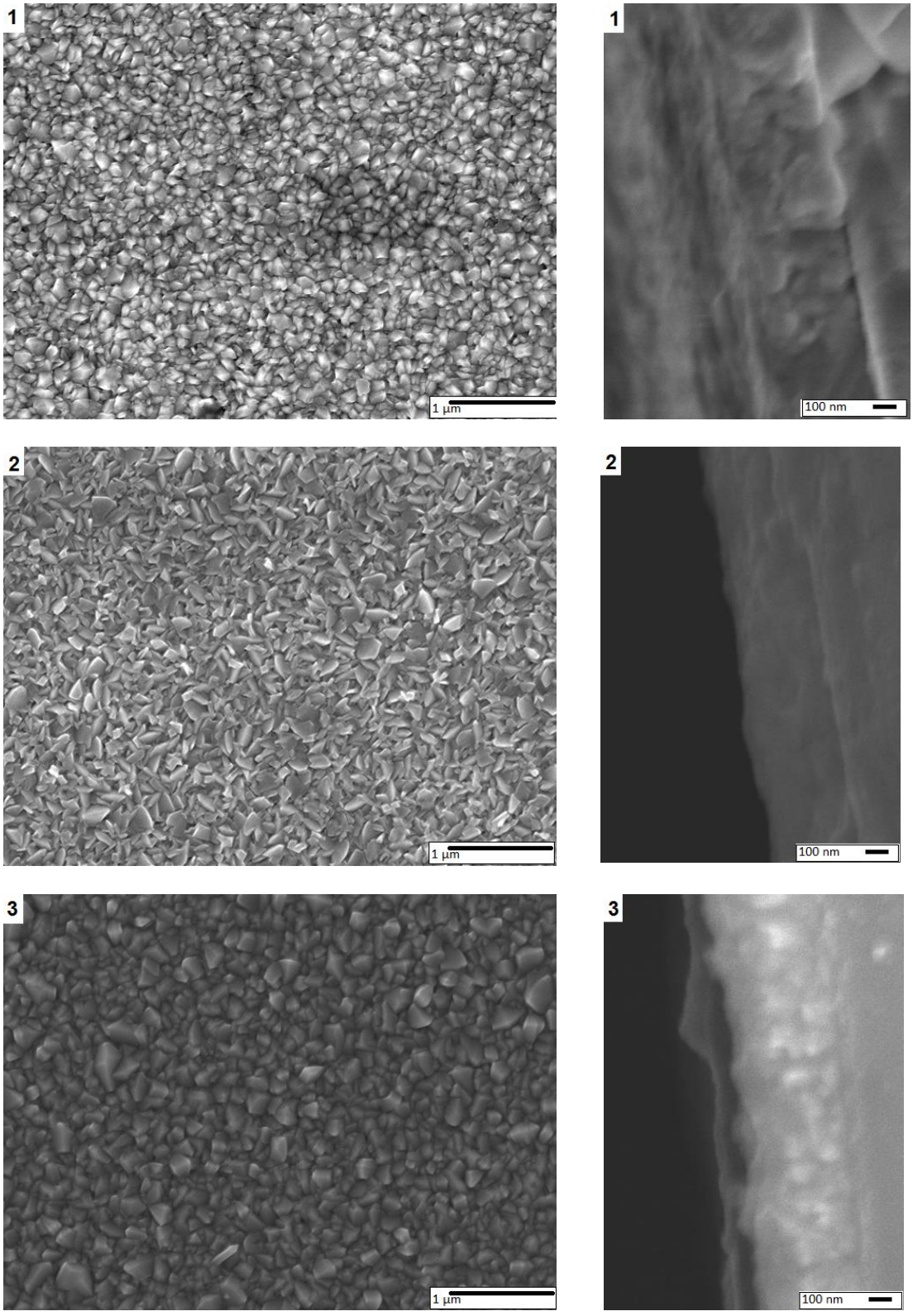

Fig. 3. 9 SEM pictures showing changes in the morphologies of the different parts of the film formed by AACVD of $Ti(OBu)_4$-MeOH at 500 °C. Numbers refer to those marked in **Fig. 3. 6**.

EDX analysis shows that lowering temperature by 50 °C reverses the Sn:Ti ratio from TiO_2 being the main matrix at 550 °C to SnO_2 at 500 °C. This is consistent with

both the XRD results showing only a minor presence of the rutile phase of TiO_2 and Hall Effect measurements along with the increasing amount of Ti in the film charge carrier mobility increases and resistance decreased. SEM micrographs (**Fig. 3. 9**) show the change of the morphology with the increase of Ti. In all three parts the films were polycrystalline, uniformly covered the substrate, were 0.3 - 0.4 μm thick and were formed of one layer, without any distinctive separation. Films covering the first and third parts both consisted of cone-like domes, though they appeared sharper in the 3rd part. The morphology of the second part differed from the former parts with its plate like facets.

Hall effect studies were performed on all 3 parts of $Ti(OBu)_4$ – MeOH – 500 °C thin film showed that they display *n-type* conductivity as electrons are the prominent type of carrier species. Part 1 had a sheet resistance of 3.9 x 10^3 Ω/□, with the charge carrier concentration of 1.1 x 10^{15} cm^{-3} and the charge carrier mobility 1.4 cm^3/Vs. Part 2 had a sheet resistance of 112.8 Ω/□, with the charge carrier concentration of 2.7 x 10^{17} cm^{-3} and the charge carrier mobility 0.2 cm^3/Vs. Part 3 had a sheet resistance of 15 Ω/□, with the charge carrier concentration of 1.5 x 10^{17} cm^{-3} and the charge carrier mobility 2.5 cm^3/Vs. Out of the 3 regions analysed only the resistance of part 3 met electrical values displayed by FTO glass (sheet resistance of 15 Ω/□, charge carrier concentration of 8.8 x 10^{20} cm^{-3} and the charge carrier mobility of 15 cm^3/Vs). All the other values show that the electrical properties of the film were affected by the TiO_2.

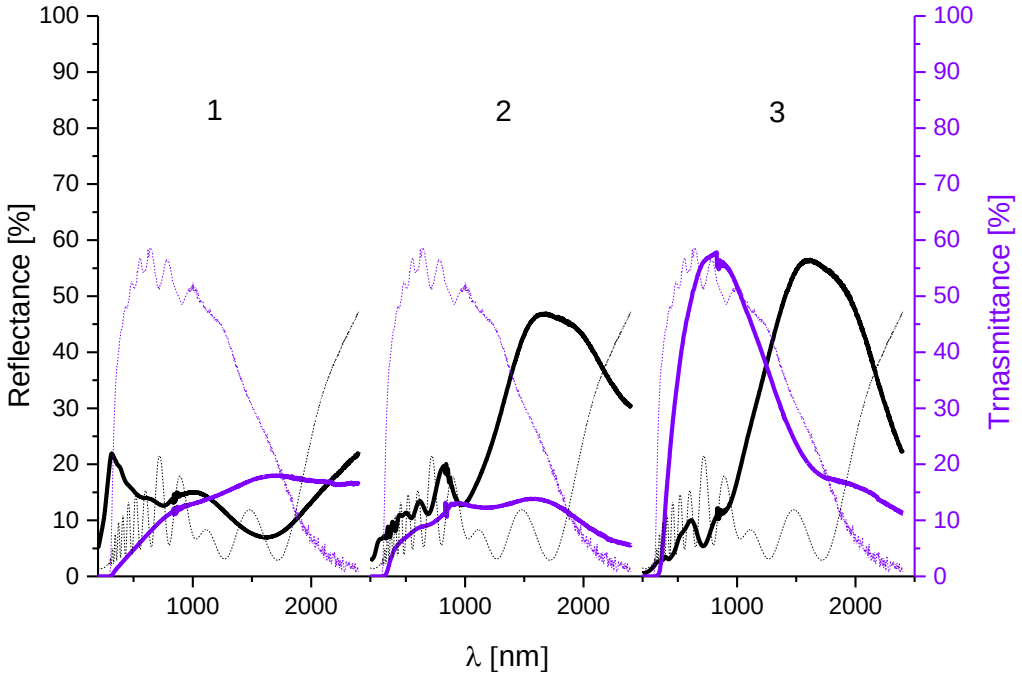

Fig. 3. 10 *UV-vis* spectra of film formed by AACVD of $Ti(OBu)_4$-MeOH at 500 °C. Dotted lines show spectra of FTO glass.

UV-vis spectra of all 3 parts are shown in the **Fig. 3. 10** and each part was compared with the *UV-vis* profile of the FTO substrate used for this synthesis (solid lines show data of a sample, dotted lines show *UV-vis* profile of FTO glass). Part 1 and 2 both display low transmittance throughout the whole measured spectrum. The reflectance of part 1 is also low despite the metallic layer of the film. Reflectance of part 2 is low in the 200 – 1000 nm region and steadily increases further into the IR region up to 50%. The *UV-vis* profile of part 3 matches the low-e window requirements with the high transmittance in the visible region (up to 60%) and high reflectance in the IR (up to 60%).

3.3.3. $Ti(OBu)_4$-$Nb(OEt)_5$-MeOH-550 °C

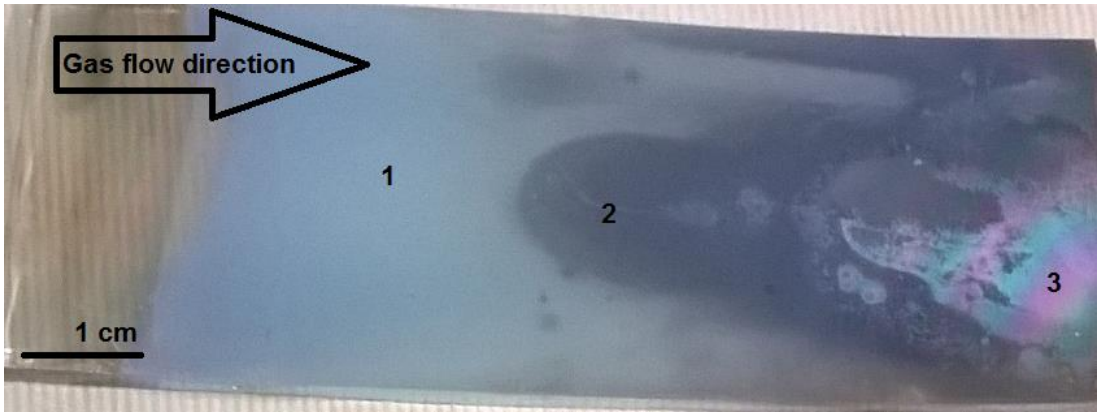

Fig. 3. 11 Picture of a film formed by AACVD of $Ti(OBu)_4$-$Nb(OEt)_5$-MeOH at 550 °C.

As the deposition of TiO_2 thin film at 550 °C resulted in a film containing significantly more rutile phase of TiO_2 than the one carried at 500 °C, niobium doping was implemented only at 550 °C.

When comparing the pictures of the $Ti(OBu)_4$ – MeOH – 550 °C and $Ti(OBu)_4$ – $Nb(OEt)_5$ – MeOH – 550 °C thin films there appears to be a reversal of the film's development, with the first 2 cm of the plate containing no film at all and the deposition moved further along the substrate. The 5 atom.% Nb:Ti doping level was chosen as it was the amount that showed the least phase segregation along with the highest electrical performance described in the chapter 2 of this thesis.

AACVD deposition of $Ti(OBu)_4$ with $Nb(OEt)_5$ dissolved in MeOH at 550 °C resulted in a film with 3 distinctive parts (marked 1, 2 and 3 on **Fig. 3. 11**). While part 1 was robust and passed the scotch tape test, parts 2 and 3 could be easily scratched or wiped. Turning the substrate 180° revealed that under the black surface of part 2 there was a metallic continuous film.

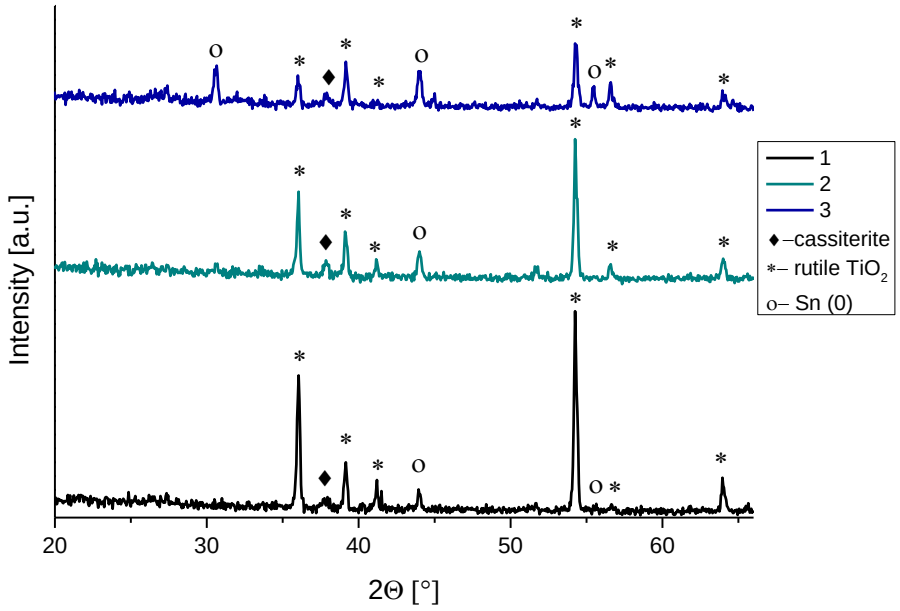

Fig. 3. 12 XRD patterns of the three parts of film formed by AACVD of $Ti(OBu)_4$-$Nb(OEt)_5$-MeOH at 550 °C. The rutile phase of TiO_2, cassiterite phase of SnO_2 and Sn(0) phases were marked.

XRD patterns of all 3 parts showed that the main phase in all 3 of them was rutile phase of TiO_2 and the second phase was metallic tin with a reflection at 37.9° corresponding with cassiterite phase of SnO_2.

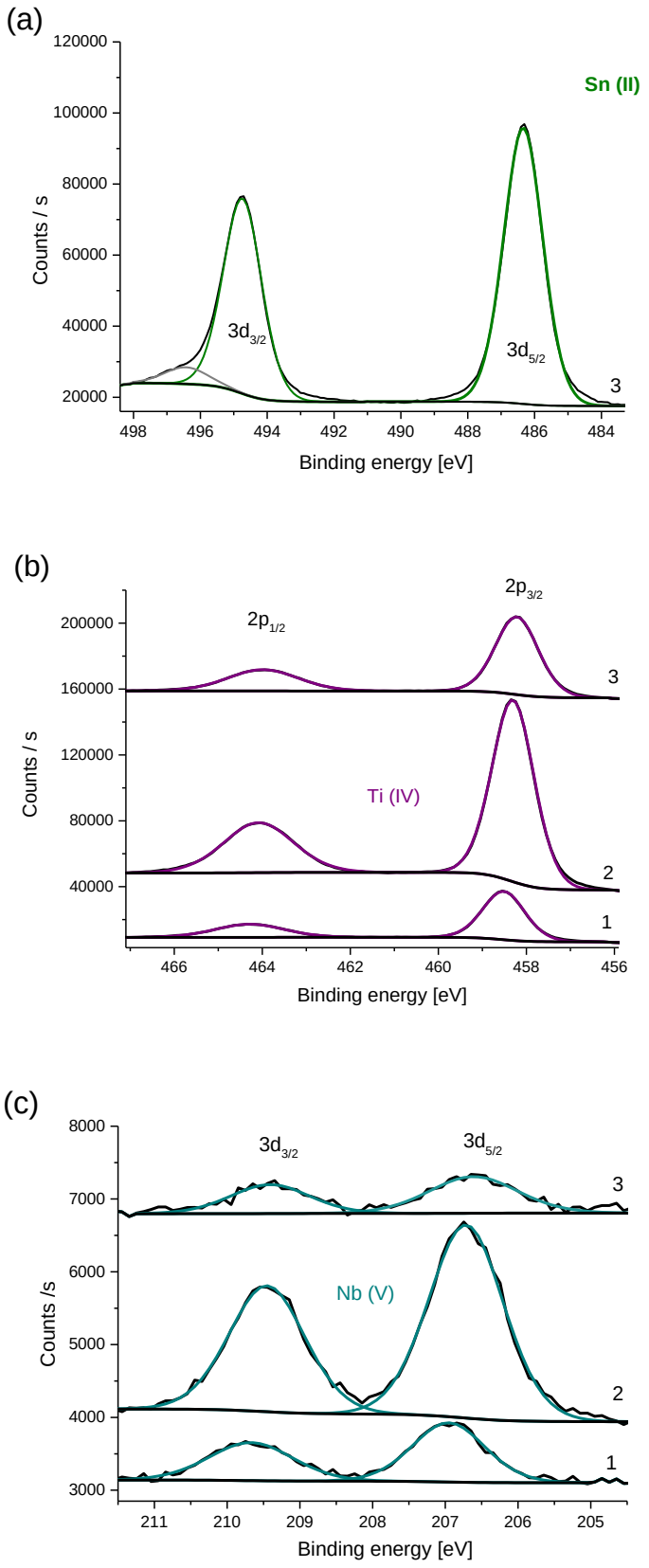

Fig. 3. 13 XPS spectra of film formed by AACVD of $Ti(OBu)_4$-$Nb(OEt)_5$-MeOH at 550 °C showing (a) tin in the 3d region (b) titanium in the 2p region (c) niobium in the 3d region.

XPS was performed on all 3 parts of the film. The surface XPS scan showed that tin was only present in the 3rd part with the binding energy for the Sn $3d_{5/2}$ excitation of 486.3 eV corresponding with Sn^{4+} in SnO_2. Titanium was present on the surface of all 3 parts with the binding energy for the Ti $2p_{3/2}$ excitation varying between 458.5 and 459.1 eV corresponding with Ti^{4+} in TiO_2. Niobium was also detected in all 3 parts, with the binding energy for the Nb $3d_{5/2}$ excitation between 206.9 to 207.0 eV corresponding to Nb^{5+}.[193]

Table 6 Results of the XPS analysis, showing the binding energies of Ti, Sn and Nb, electrical properties, atomic % ratio measured by EDX and film thickness of the film formed by AACVD of $Ti(OBu)_4$-$Nb(OEt)_5$-MeOH at 550 °C.

	Binding energy [eV]			Hall effect measurements			EDX atomic % ratio			Film thickness [nm]
	Ti^{4+} $2p_{3/2}$	Sn^{4+} $3d_{5/2}$	Nb^{5+} $3d_{5/2}$	Charge carrier concentration [cm^{-3}]	Charge carrier mobility [$cm^2 V^{-2} s^{-1}$]	Resistance [$\Omega \square^{-1}$]	Ti	Sn	Nb	
1	459.1	-	207.0	2.4×10^{16}	11.5	22.9	94	5	1	0.3 + 0.8
2	458.7	-	207.1	1.1×10^{17}	3.5	16.3	88	11	1	0.2 + 0.7
3	458.5	486.3	206.9	-	-	> 1M	90	9	1	0.3 + 0.8

SEM images (**Fig. 3. 14**) revealed how the addition of $Nb(OEt)_5$ into the precursor mixture changes the films' morphology. It is clear that instead of homogenous films like in case of $Ti(OBu)_4$– MeOH – 550 °C, each part consisted of films with two distinctive layers. Part 1 consisted of 0.3 μm layer of FTO thin film and 0.8 μm layer of Ti:Sn:Nb mixed oxide, the surface of which was composed of broad rhomboidal facets. The 2nd part was also formed of two layers, but they were separated from each other and a substrate. First layer was formed of 0.2 μm thin reduced metallic continuous β-Sn film, which was flexible upon bending by the brittle metal oxide film layer. The top layer appeared to be more crystalline than that of the 1st and 3rd part, with the morphology similar to the one displayed by 3rd part of $Ti(OBu)_4$ – MeOH – 550 °C film. Such distinctive crystals might also be a reason why part 2 had the highest conductivity of all

3 parts. In the 3rd part two layers could be also distinguished with the 0.3 μm FTO layer at the bottom and 0.8 μm layer of the Ti:Sn:Nb mixed oxide on the top.

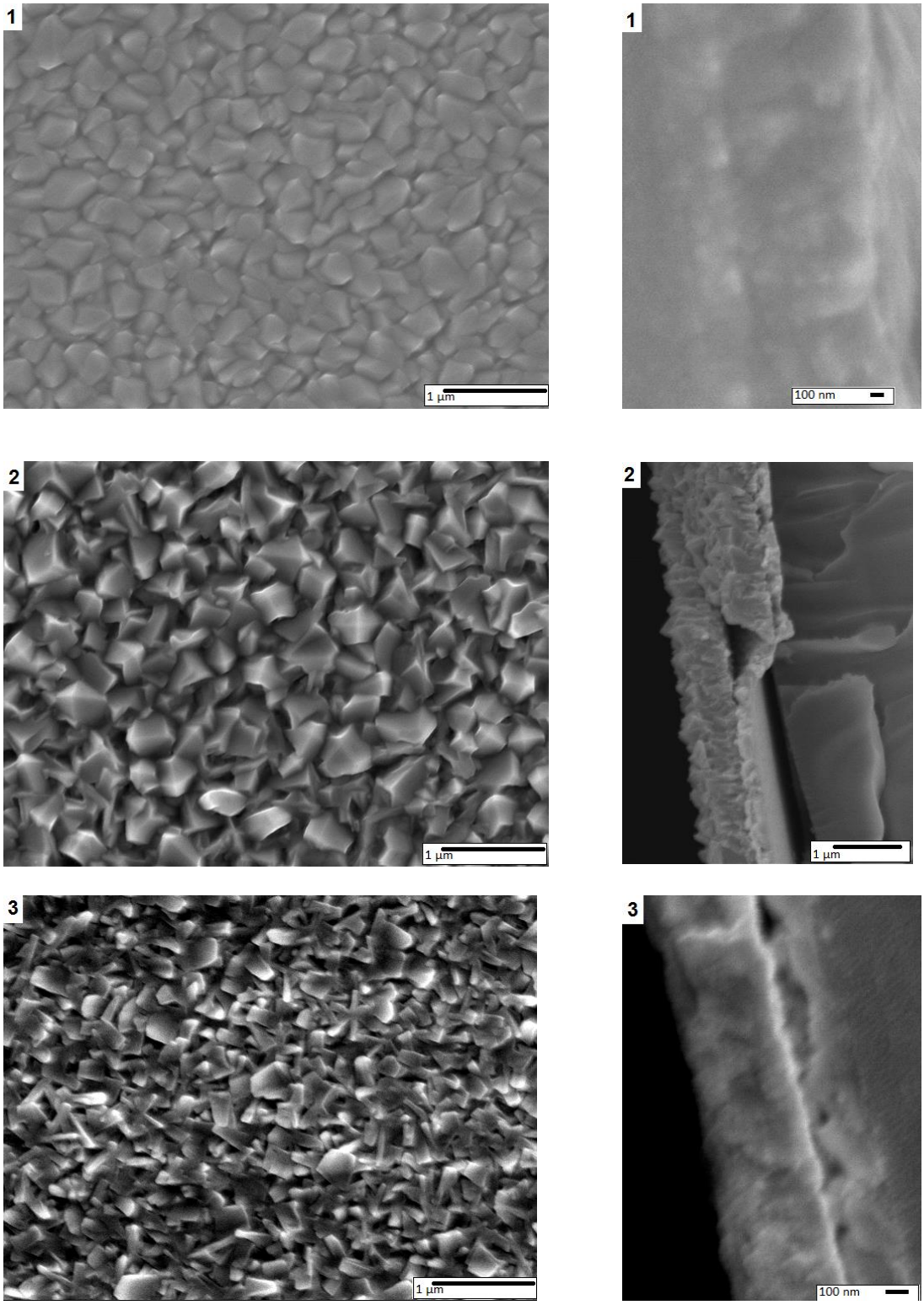

Fig. 3. 14 SEM pictures showing changes in the morphologies of the different parts of the film formed by AACVD of $Ti(OBu)_4$-$Nb(OEt)_5$-MeOH at 550 °C. Numbers refer to those marked in **Fig. 3. 11**.

The Hall effect studies were performed on parts 1 and 2 of $Ti(OBu)_4$ – $Nb(OEt)_5$ – MeOH – 550 °C thin film and showed that they displayed *n-type* conductivity as electrons were the prominent type of carrier species. Part 1 has a sheet resistance of 22.9 Ω/□, with charge carrier concentration of 2.4 x 10^{16} cm^{-3} and the charge carrier mobility of 11.5 cm^3/Vs. Part 2 has a sheet resistance of 16.3 Ω/□, with the charge carrier concentration of 1.1 x 10^{17} cm^{-3} and the charge carrier mobility of 3.5 cm^3/Vs.

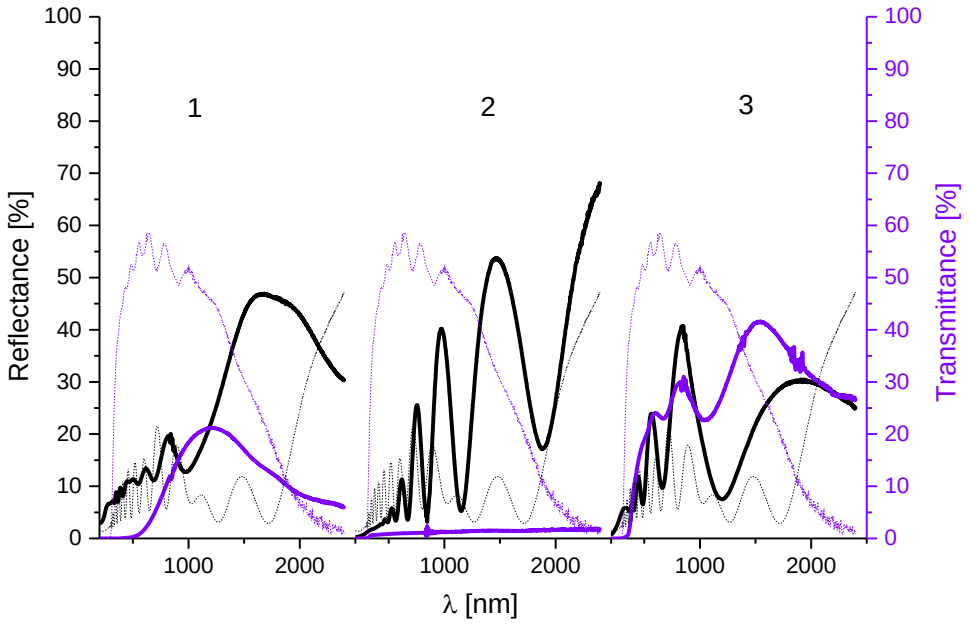

Fig. 3. 15 *UV-vis* spectra the film formed by AACVD of $Ti(OBu)_4$-$Nb(OEt)_5$-MeOH at 550 °C. Dotted lines show spectra of FTO glass.

UV-vis transmittance – reflectance profile of all 3 parts is shown in the **Fig. 3. 15** and each part was compared with the *UV-vis* profile of the FTO substrate used for this synthesis (solid lines show data of a sample, dotted lines show *UV-vis* profile of FTO glass). Part 1 was transitive only in the region between 800 and 1800 nm (up to 20%) while its reflectance increased steadily from 10% at 1200 nm to 50 % in the far IR region. Part 2 showed no transmittance throughout the whole measured spectrum and its reflectivity increased linearly from 0% at 200 nm to 70% at 2400 nm. The *UV-vis* profile of part 3 showed transmittance increasing in the 200 – 1200 nm region up to

30% and remaining steady the higher wavelength. Its reflectance growth was constant from 0% at 200 nm to 30% at 2400 nm.

3.3.4. $Ti(OEt)_4$-hex-500 °C and $Ti(OEt)_4$-$Nb(OEt)_5$-hex-500 °C

Undoped and niobium doped TiO_2 thin film was deposited on FTO glass used as a substrate at 500 °C from hexane solution via AACVD. In order to decrease the carbon contamination the titanium precursor was changed from $Ti(OBu)_4$ to $Ti(OEt)_4$ and $Nb(OEt)_5$ was used as niobium source at the 0 and 5 atom.% doping level. In both cases the obtained films were uniform, robust, transparent and colourless.

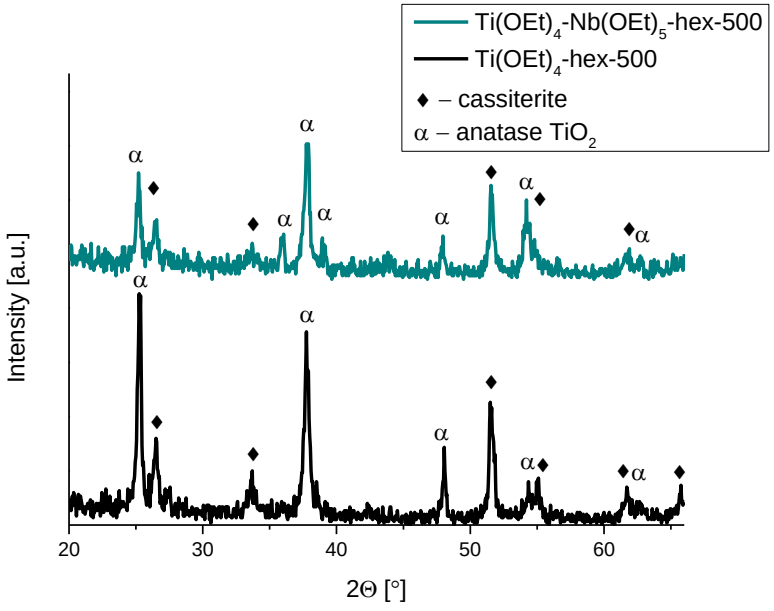

Fig. 3. 16 XRD patterns of the thin films formed by AACVD of $Ti(OEt)_4$-hex at 500 °C and $Ti(OEt)_4$-$Nb(OEt)_5$-hex 500 °C. The anatase phase of TiO_2 and cassiterite phase of SnO_2 were marked.

XRD shows that the anatase phase of TiO_2 and cassiterite phase of SnO_2 are the only two phases present in both investigated films.

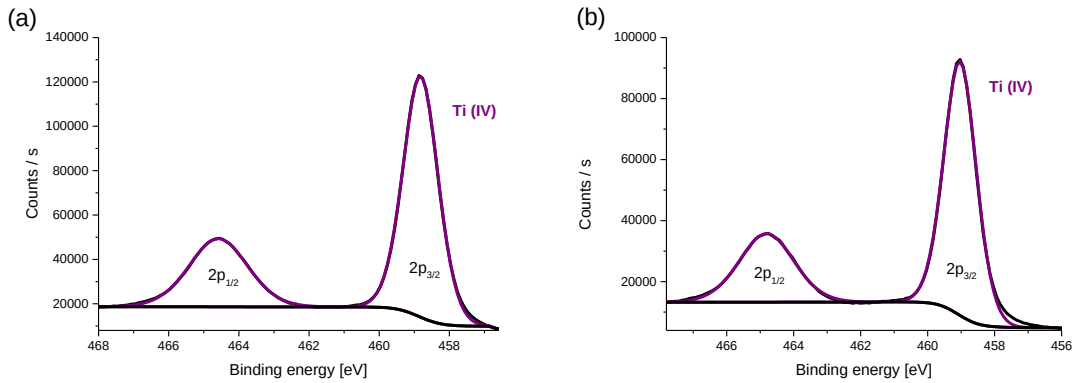

Fig. 3. 17 XPS spectra in titanium 2p region of (a) $Ti(OEt)_4$-hex-500 °C and (b) $Ti(OEt)_4$-$Nb(OEt)_5$-hex-500 °C thin films.

XPS analysis in both cases showed no sign of fluorine, tin or niobium in the film. Titanium present in the film was only in the 4^+ oxidation state with a binding energy for the $2p_{3/2}$ excitation of 458.8 eV in each film.

Table 7 Results of the XPS analysis, showing the binding energies of Ti, atomic % ratio measured by EDX and film thickness of the thin films formed by AACVD of $Ti(OEt)_4$-hex at 500 °C and $Ti(OEt)_4$-$Nb(OEt)_5$-hex 500 °C.

	Binding energy [eV]	EDX atomic % ratio			Film thickness [µm]
	Ti^{4+} $2p_{3/2}$	Ti	Sn	Nb	
$Ti(OEt)_4$-hex-500	458.8	67	33	-	0.4 + 0.04
$Ti(OEt)_4$-$Nb(OEt)_5$- hex-500	458.8	60	37	3	0.4 + 0.03

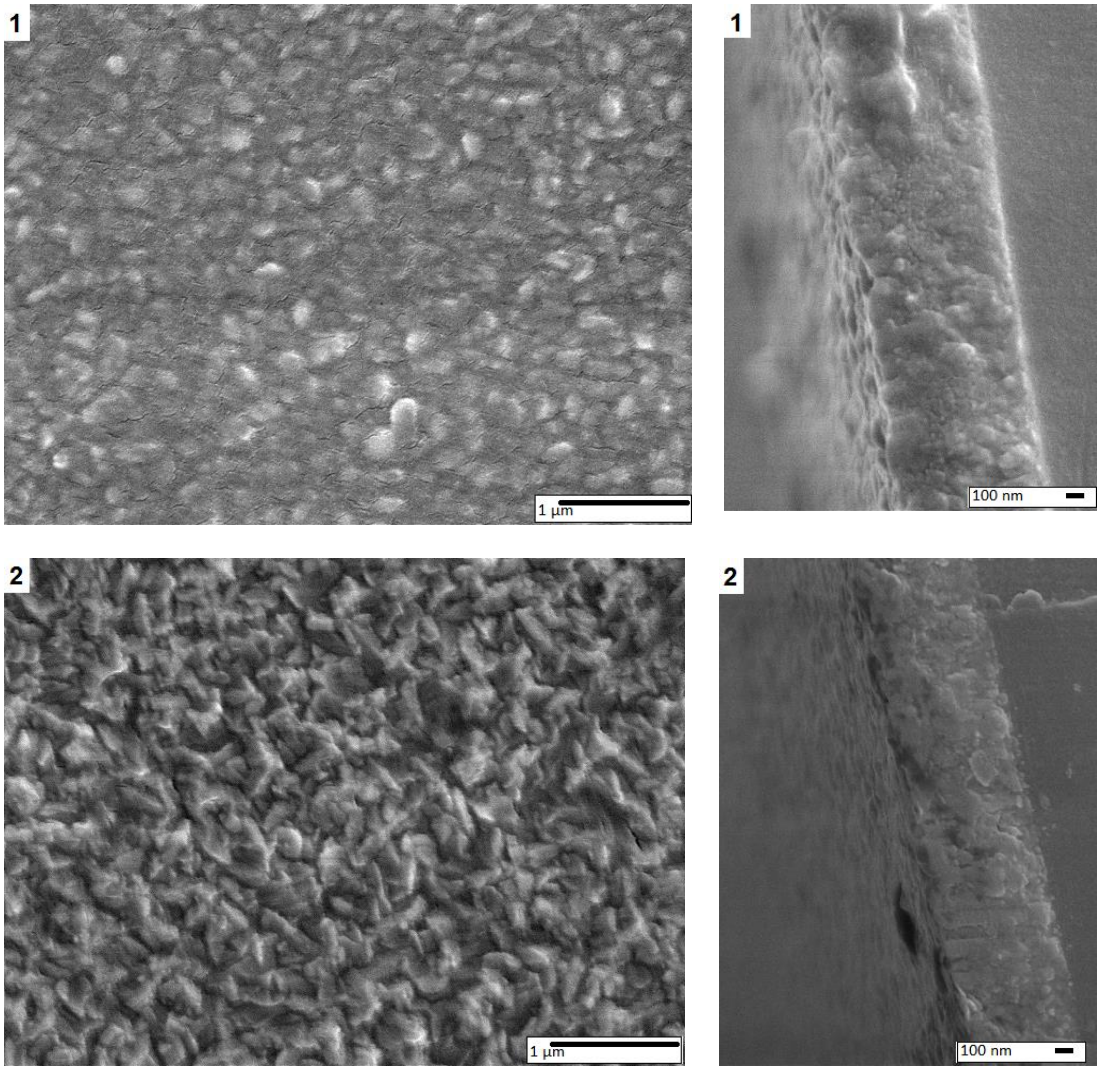

Fig. 3. 18 SEM pictures showing changes in the morphologies between (1) $Ti(OEt)_4$-hex-500 °C and (2) $Ti(OEt)_4$-$Nb(OEt)_5$-hex-500 °C thin films.

SEM micrographs of the films deposited from hexane as a solvent showed that in both cases films were composed of two layers – first one was a 0.3 µm layer of FTO, and second one was a layer of anatase TiO_2 both pristine and Nb doped. The microstructure of the $Ti(OEt)_4$-hex-500 °C thin film shows that the as-deposited film was composed of rather flat domes of size about 40-70 nm, similar to the anatase form of TiO_2 films revealed in the undoped TiO_2 film in chapter 2. Upon doping with Nb the facets have sharp pyramids shape.

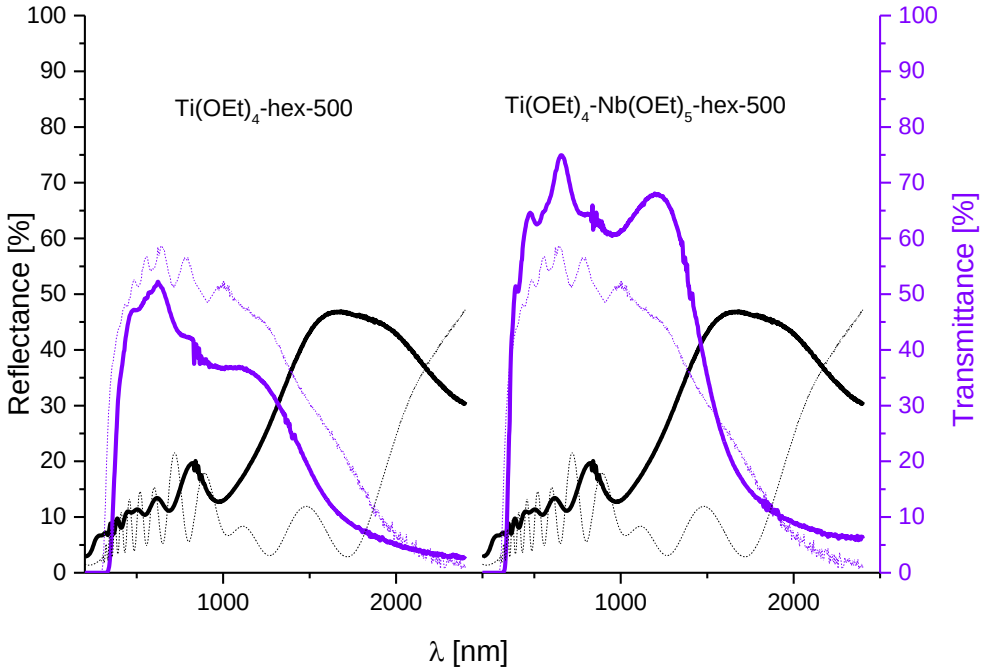

Fig. 3. 19 *UV-vis* spectra of $Ti(OEt)_4$-hex-500 and $Ti(OEt)_4$-$Nb(OEt)_5$-hex-500 thin films. Dotted lines show spectra of FTO glass.

UV-vis transmittance – reflectance profile of all 3 parts is shown in the **Fig. 3. 19** and each part was compared with the *UV-vis* profile of the FTO substrate used for this synthesis (solid lines show data of a sample, dotted lines show *UV-vis* profile of FTO glass). Both of the investigated films showed same reflectance profile which increases from 10% at 1000 nm to 50% around 2000 nm and then decreased to 30%. The transmittance spectra of both films was similar to the one displayed by FTO substrate, while the TiO_2 was 10% lower and Nb:TiO_2 15% higher in the 200 – 1800 nm range.

3.4. Discussion

Even though all the deposited films with and without the addition of niobium and parts exhibited an electrical conductivity, only the ones with amounts of Sn exceeding or equal Ti were conductive enough to allow the Hall Effect measurements. The addition of niobium into the precursor mixture resulted in films with distinctive two layers, the highest amounts of Ti shown by EDX analysis and the highest ratio of rutile TiO_2 phase amongst all films deposited using MeOH as a solvent.

Although β-Sn was present in most of the parts of the films deposited from MeOH, each film deposited both at 500 and 550 °C had only one part with the continuous mirror film. Each part consisting of β-Sn was either grey in color or had its transparency affected by the haze.

Different morphologies of the MeOH deposited films can be explained by the mass transport effects of the CVD process. Consequently as the reagents deplete as the deposition moved further from the inlet, the synthesis conditions change such as precursor concentration and their temperature.[194] This directly affects the decomposition, absorption, nucleation and growth as well as desorption processes, which therefore has an impact on the Ti:Sn:Nb:O ratio during the entire deposition. The difference in the phase composition and higher rutile phase of TiO_2 content in some parts over other can be also enhanced by the changes in the local temperatures of the substrate, being a result of the AACVD reactor setup.[195, 196]

Reduction of the SnO_2 and formation of β-Sn indicates oxygen deficiency during the reaction. This has been previously ascribed to the ability of solvents such as MeOH, EtOH or iPrOH to cause a hydride reduction of SnO_2 to the metal as a result of decomposition of the solvent at the high temperatures.[6, 197, 198] As explained by Chadwick *et al.,*[196] this is why all the films and their parts deposited from MeOH contained β-Sn as one of the phases present. Methanol during the decomposition reacts

with the layer of FTO on the substrate leading to re-formation and re-crystallisation of the film. $Ti(OBu)_4$ during its decomposition reacts with SnO_2 creating a mixed metal oxide or a solid solution instead of intended layers. While at 500 °C particles of β-Sn are mostly scattered in the film. At 550 °C the degree of oxygen deficiency is high enough to create a continuous metallic film between a substrate and metal oxide film. It is expected that these two reactions occur simultaneously to create the continuous metallic film, reducing the FTO using pure MeOH both at 550 and 500 °C did not result in any change to the substrate in this experiment. Since hexane as a solvent used in the reaction does not reacts with the FTO layer during deposition, the XRD shows only two phases anatase TiO_2 and cassiterite SnO_2. The SEM micrographs show that their grain size is similar however, two layers can be noticed. XPS results are in agreement with this conclusion, as the surface scans show only titanium, with the binding energy ascribed to TiO_2.

Neither EDX nor XPS analysis showed the presence of fluorine in the films, which indicates that due to the low solubility of fluorine both in SnO_2 and TiO_2,[199, 200] during the re-formation and re-crystallisation of the films fluorine was removed from the film. This corresponds with the XRD and SEM results showing that in the reactions where methanol was a solvent, instead of acting as a seed layer FTO took part in the films' interacting with the precursors. The binding energies for the Ti^{4+}, Sn^{4+} and Nb^{5+} peaks varied very little across the different films and parts analysed, which is in agreement to the results obtained by Sathasivam *et al.*[195] Since the XPS is a surface-sensitive technique[201, 202] and the fact that the tin was not detected on the surface of all the films and parts might suggest the phase segregation of SnO_2 and TiO_2, especially in the films where methanol was used as a carrier. This effect has been previously observed in the literature of TiO_2 - SnO_2 composite thin films deposited both by AA and AP CVD techniques.[190, 195, 196]

Each part of the described films display high electrical conductivity also characterise with the surface plasmon resonance observed in the *UV-vis* spectrum with high reflectance and low transmittance in the near-infrared region.[203]

Apart from the thin film deposited using $Ti(OEt)_4$ and $Nb(OEt)_5$ from hexane at 500 °C thin film all the deposited film and their parts display transmittance lower than that of the FTO film used as a seed layer. This is caused by the oxygen deficiency during the deposition affecting the transmittance in the visible region. As shown by Noor[6] oxygen-rich conditions result in the improved optical transparency of the SnO_2 thin films. Interestingly is the impact of FTO layer on the niobium incorporation into the anatase phase of TiO_2 thin film. As shown in the literature[87, 99, 175, 204, 205] and chapter 2 of this thesis doping niobium into the TiO_2 lattice affects a blue coloration of the deposited films, which are also electrically conductive, with the values close to commercial TCO materials. Both of the described films were transparent, electrically insulating and with XPS showing only Ti^{4+} on the surface. This suggests the surface phase segregation between niobium and titania. The lack of the peaks in the XRD pattern belonging to any of the niobium oxides indicates that even though niobium is incorporated into the lattice as EDX shows, it either occupies interstitial sites of TiO_2 lattice or creates nanocrystals of Nb_xO_y as a phase separated composite with TiO_2 as described in chapter 2.

3.5. Conclusion

While using hexane as a solvent in the reaction, FTO acts as a seed layer affecting the morphology, dopant ratio and electrical properties of the films deposited over it. When changing a solvent to MeOH, the FTO layer acts as one of the precursors, undergoing various reactions depending on the temperature of the substrate, oxygen ratio and the depletion of the precursors. Those reactions were ranging from a

complete reduction to metallic tin forming either a continuous film or particles of β-Sn, to creating a mixed phased TiO_2 - SnO_2 layer.

4. Synthesis and characterisation of pristine and niobium doped TiO_2 thin film nanocomposites with a silver layer by RF magnetron sputtering and AACVD.

4.1. Introduction

Silver films and its composites has found application in the multiple materials such as high-temperature superconductive ceramics, as silver mirrors or as bactericidal compounds.[206-208] Application of silver in the microelectronics and TCO with silicon substrate is limited due to the diffusion of silver into the Si, which leads to the increase of the material's resistivity.[209, 210] Chapter 2 showed that upon successful doping of niobium into the TiO_2 lattice the photocatalytic properties of TiO_2 substantially decreased. Niobium doped TiO_2 is a promising material for low-e glazing as doping of niobium into the titania decreases its transparency in the IR region, while remaining good transparency in the visible region. Another advantage of niobium doping into the TiO_2 lattice is obtaining a pleasant, blue colour of the glazing.[204] Although in order for Nb:TiO_2 to meet commercial requirements low-e window glazing, the IR reflectance should be increased. Magnetron sputtered silver coatings offer both partial transmittance in the visible range (for 10 nm thin film transmittance is 50 %[3]) as well as IR reflectivity in the range of 95-99%.[211] Unlike a TiO_2 thin film, such a metal film tends not to be durable and can be easily wiped or scratched, consequently it is usually applied to an inside surface of a double panel windows so it can be protected by the glass. Covering silver or gold PVD coating with a layer of TiO_2, which has an excellent mechanical durability[212] as a thin film may lead to the visible transparent, IR-reflective and durable, long lasting window glazing.

4.2. Experimental

4.2.1. Chemicals and substrates

All chemicals used in this experiment were purchased from Sigma Aldrich Chemical Co. and used without further purification; silver and gold sputtering target, diam. x thickness 3.00 in. x 0.125 in., 99.99% trace metal basis, 2 g of technical grade titanium(IV) ethoxide, (0-5 atom.% Nb:Ti) 99.95% niobium(V) ethoxide, 25 ml of hexane. Nitrogen (oxygen free) was provided by BOC. The precursor flow was kept at 0.6 l/min.

4.2.2. Material synthesis

Deposition of the 0 – 11 nm thick silver and gold films was carried out in the *JEOL JFC-1200 Fine Coater* RF magnetron sputtering chamber, using argon as a carrier gas, current of 35 mA for 0 – 150 s on a 15 cm x 3.5 cm x 0.3 cm standard float glass coated with a 50 nm layer of SiO_2 to prevent ion migration from the glass[161] supplied by Pilkington NSG Group. Deposition of pristine and niobium doped TiO_2 thin films was carried out in the AACVD reactor (see 2.2.2). Films were deposited onto the gold or silver films in a cold wall reactor in the N_2 atmosphere, the temperature of the substrate was 500 °C during the entire deposition, and then cooled to room temperature.

4.2.3. Material characterisation

For identification of the crystal structure and orientation of the film, X-ray film diffraction (XRD) was carried out on a *Bruker GADDS D8* diffractometer with a Cu-Kα X-ray source and readings were taken over the 10 ° < 2θ < 66 ° range. To confirm the phase of the film a *Reinshaw 1000 Invia* Raman spectrometer was used under ambient conditions with an Ar laser source (514.5 nm) over the 100-1500 cm^{-1} wavelength range. Transmittance-Reflectance (T-R) spectra were taken against an air background using a *Perkin Elmer Fourier Transform Lambda 950 UV-vis* spectrometer at a wavelength range of 200-2500 nm. Film thickness was measured with *Scanning Electron Microscopy* (SEM) side images of the films using a *JEOL JSM-6301F Field Emission SEM* at accelerating voltage of 5 keV, on Au-coated samples. SEM imaging was also used to determine film morphology. Energy dispersive X-ray (EDX) was used to determine the Nb:Ti atomic ratio on the C-coated samples. Measurements of surface composition and the state of the elements were carried out using a *Thermo Scientific K-Alpha* X-ray photoelectron spectrometer (XPS) with a monochromatic Al-Kα source. Results were then fitted using CasaXPS software with the binding energies calibrated to carbon (285 eV). Water contact angle measurements were carried out to determine hydrophilic/hydrophobic properties using a *FTA 1000 Water Droplet Analyser*. Samples were cleaned and then measurements were taken on non-irradiated samples as well as those irradiated with a 254 nm lamp for various amounts of time. For the photocatalytic activity tests, intelligent ink, based on Rezazurin dye was prepared as described by Mills *et al.* Samples were cleaned with acetone and propan-2-ol, irradiated overnight with 254 nm for further cleaning and then sprayed with the ink. UV-vis transmittance spectra were taken after irradiation with 365 nm light until complete decomposition of the dye. Charge carrier concentration (n /cm^{-3}), charge carrier mobility (μ /cm^2 V^{-1} s^{-1}), bulk resistivity (ρ /Ω cm) and sheet resistance (R_{sh} /Ω $\square^{-1}$)

were measured at room temperature on an *Escopia HMS-3000* set up in the Van der Pauw configuration. Measurements were carried out using a current of 1μA and 0.58 T permanent magnet on ≈ 1 x 1 cm squares with silver paint (Agar Scientific) used as ohmic contacts, the integrity of which was tested prior to measurement.

4.3. Results

The TiO_2 and Nb:TiO_2 thin films that were deposited onto the gold layer had a deep purple colour, while the TiO_2 thin film deposited onto the silver was deep blue and the corresponding Nb:TiO_2 film was violet. Films with gold layer were not adsorbed to the surface of the substrate and were flaking off when touched. No further analysis was performed on these films. Films that were yellowish in colour, powdery, easily wiped from the substrate's surface by hand were designated as AgΔT. Films with the TiO_2 layer deposited onto the silver layer were well adsorbed to the surface and passed the Scotch tape test shortly after deposition as well as after storing exposed to the air over a year period. The following chapter focuses on characterisation of 3 films:

- AgΔT- 11 nm layer of silver film sputtered on the silica coated glass, heated up to 500 °C in the AACVD reactor with N_2 gas flow and cooled down to room temperature,
- Ag:TiO_2- 11 nm layer of silver film sputtered on the silica coated glass, heated up to 500°C in the AACVD reactor with N_2 gas flow, covered with TiO_2 thin film and cooled down to room temperature,
- Ag:Nb:TiO_2- 11 nm layer of silver film sputtered on the silica coated glass, heated up to 500 °C in the AACVD reactor with N_2 gas flow, covered with Nb doped TiO_2 thin film and cooled down to room temperature.

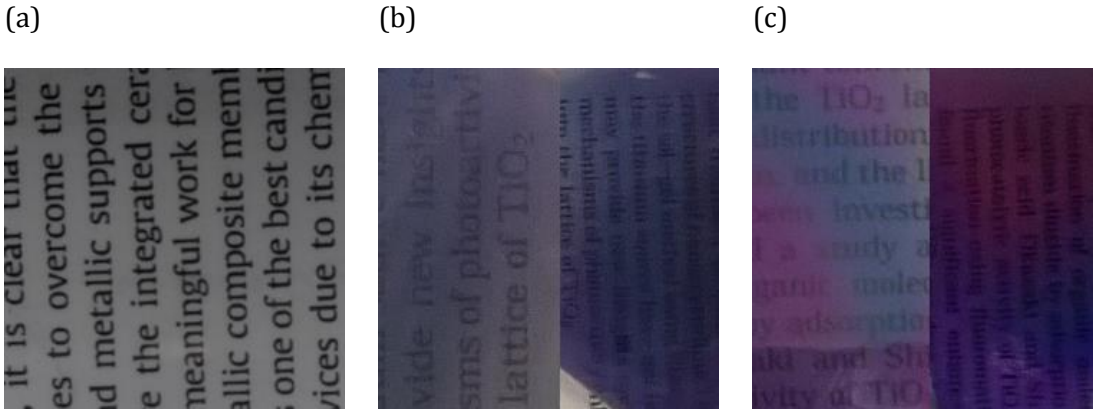

Fig. 4. 1 Pictures showing (a) TiO_2, (b) Ag:TiO_2, (c) Ag:Nb:TiO_2 thin films. Pictures of Ag:TiO_2 and Ag:Nb:TiO_2 were taken from two different angles of the same piece of film. All three thin films were photographed against scientific report printed out on the white paper.

As a reference TiO_2 thin film (see chapter 2) was used.

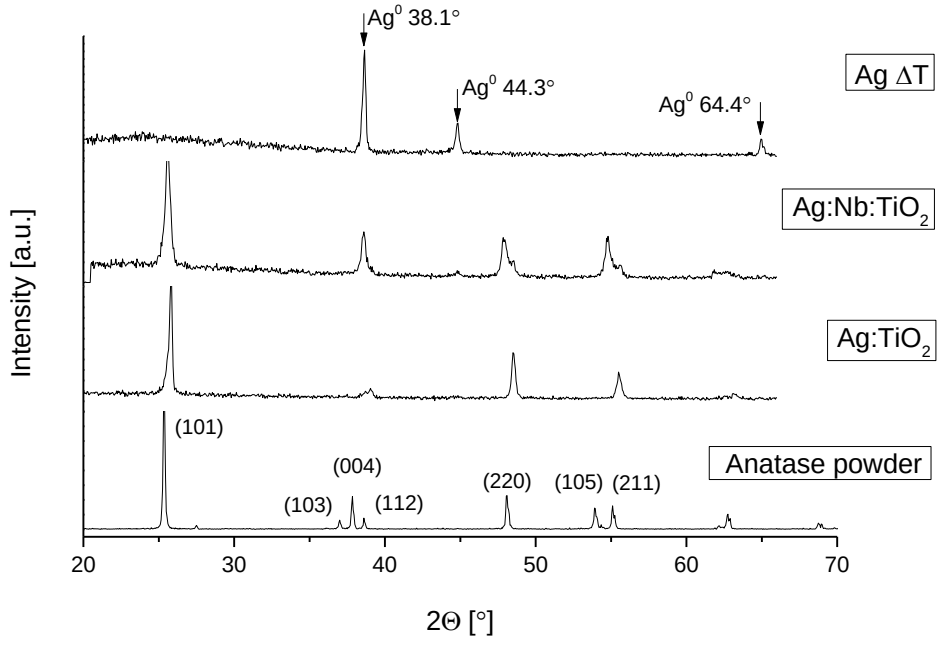

Fig. 4. 2 XRD pattern of anatase powder, AgΔT, Ag:TiO_2, Ag:Nb:TiO_2 thin films. The anatase reflection positions with appropriate values *(hkl)* are shown in brackets.

X-ray diffraction of the sliver film, sputtered by PVD and heated up to 500 °C in the CVD reactor revealed the presence of the *silver-3c syn*,[106, 213] while the only phase observed in Ag:TiO_2 and Ag:Nb:TiO_2 thin films were the anatase form of TiO_2 (**Fig. 4. 2**). In both cases no preferred orientation of the deposited films could be distinguished. The Raman (**Fig. 4. 3**) patterns were consistent with the XRD, showing no significant features in AgΔT film, and the presence of only peaks distinctive for the anatase form of TiO_2 in both Ag:TiO_2 and Ag:Nb:TiO_2 thin films, although the lack of 143 cm^{-1} peak attributed to the O–Ti–O vibrations, as well as broad and low intensity peaks in Ag:Nb:TiO_2 thin film, has to be pointed out.

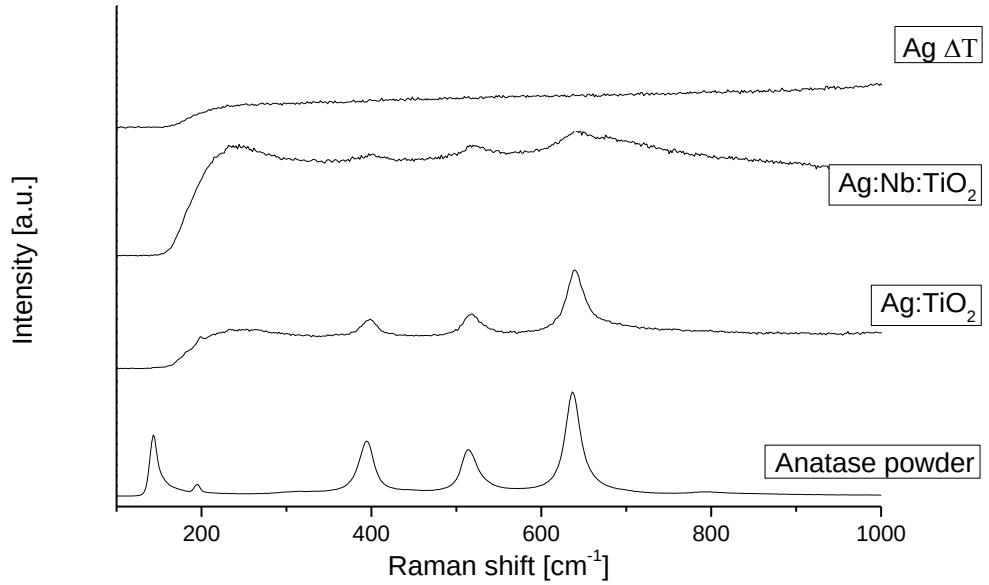

Fig. 4. 3 Raman spectra of anatase powder, AgΔT, Ag:TiO_2 and Ag:Nb:TiO_2 thin films.

X-ray photoelectron spectroscopy was performed on AgΔT, Ag:TiO_2 and Ag:Nb:TiO_2 thin films obtaining both surface scans as well as depth profiles. For the AgΔT thin film the energy for the Ag $3d_{5/2}$ excitation was 368.5 eV with the peak separation of 6.0 eV, indicating the metallic nature of the silver and the absence of Ag^+ ions.[110, 113, 214] For films with the TiO_2 layer the energy of the Ti $2p_{3/2}$ excitation was

458.7 eV, which corresponds with Ti^{4+} in TiO_2.[167] Niobium was detected at all levels in the Ag:Nb:TiO_2 sample and the binding energy for the Nb $3d_{5/2}$ excitation was 207.1 eV, which is representative of Nb^{5+} formation.[215] Silver was detected at all levels only in the Ag:Nb:TiO_2 sample with the binding energy for the $3d_{5/2}$ excitation of 365.8 eV. This effect was reproducible in both Ag:TiO_2 and Ag:Nb:TiO_2 thin films.

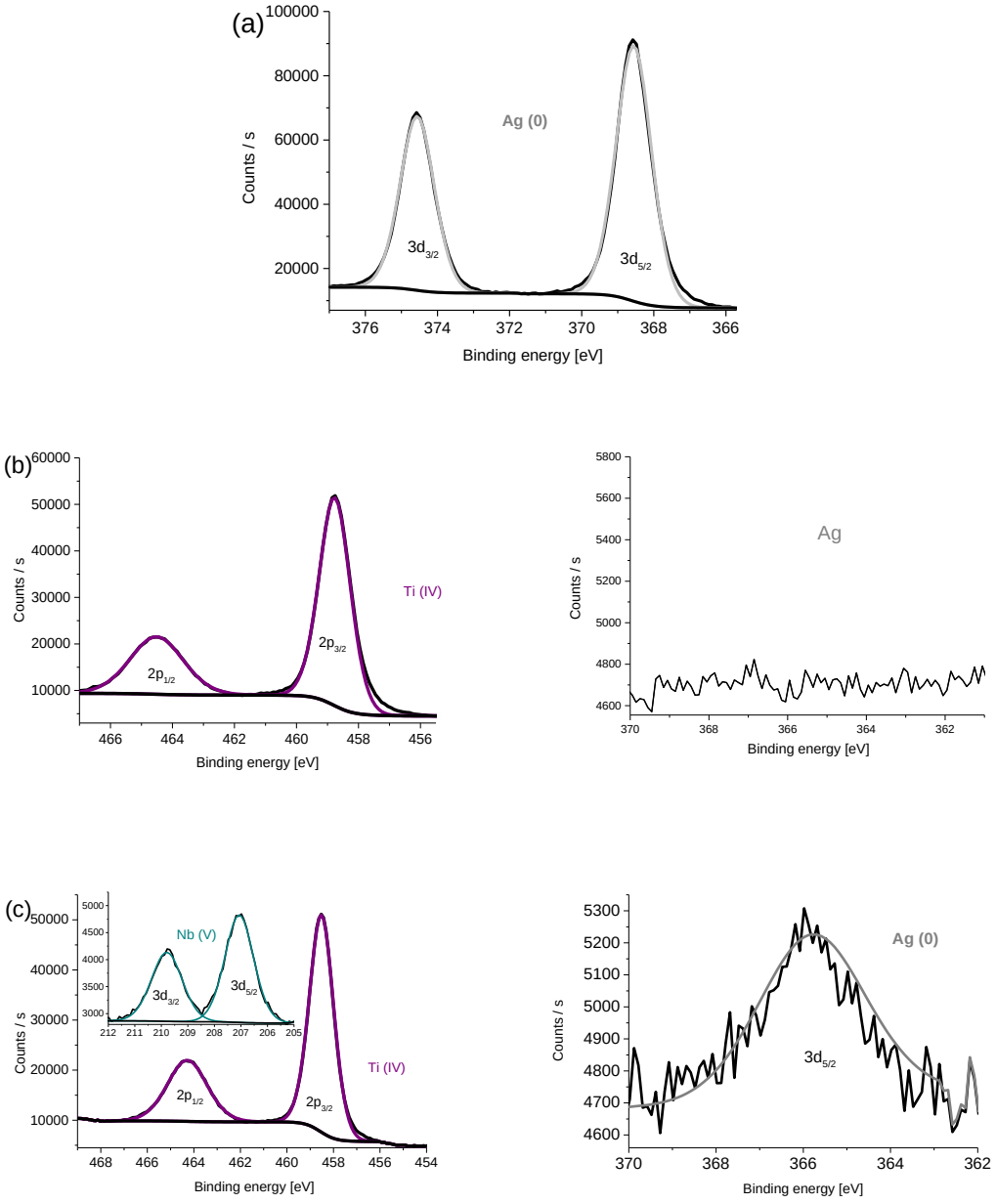

Fig. 4. 4 XPS spectra of (a) AgΔT (b) Ag:TiO_2 (c) Ag:Nb:TiO_2 thin films in the titanium 2p region (insert shows niobium 3p region) and silver 3d region.

Table 8 Results of the XPS analysis, showing the binding energies of Ti, Nb, Ag; XPS atomic % ratio; EDX atomic % ratio and the film thickness of the Ag:TiO_2 and Ag:Nb:TiO_2 thin films.

Sample	Binding energy [eV]			XPS atomic % ratio			EDX atomic % ratio			Film thickness [μm]
	Ti $2p_{3/2}$	Nb $3d_{5/2}$	Ag $3d_{5/2}$	Ti^{4+}	Nb^{5+}	Ag	Ti	Nb	Ag	
Ag:TiO_2	458.7	N.A.	-	100	N.A.	-	32	N.A.	1	0.6 ± 0.09
Ag:Nb:TiO_2	458.7	207.1	365.8	97	2	1	40	9	1	0.4 ± 0.05

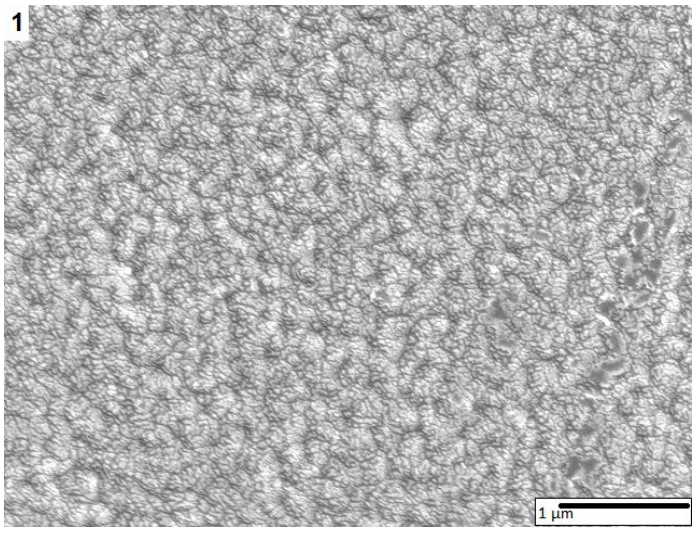

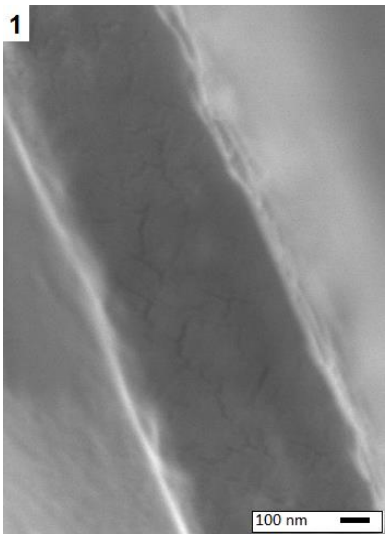

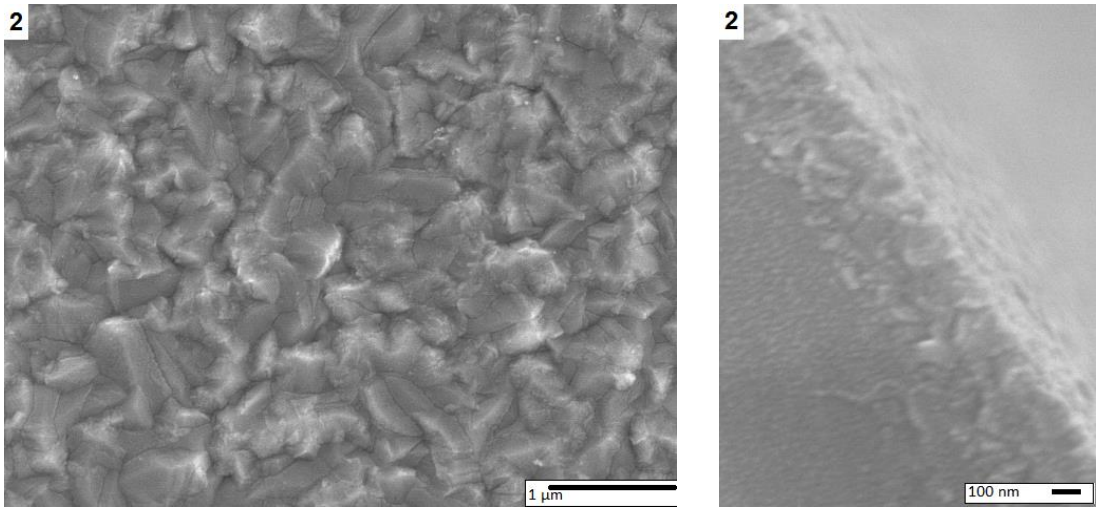

Fig. 4. 5 Top-down and side-on SEM pictures of (1) Ag:TiO_2 and (2) Ag:Nb:TiO_2 thin films.

The morphology of the film surface (**Fig. 4. 5**) changed both with the addition of the Ag and Nb to the TiO_2. As seen in the **Fig. 2. 11** the pristine TiO_2 thin film was made up an irregular aggregation of small units approximately 10 nm size. The surface of the Ag:TiO_2 thin film was made of small units about 10 nm and smaller, creating "curd-like" 200 nm agglomerations. This trend was reversed in the Ag:Nb:TiO_2 thin films which were made of large cone-like crystallites between 200 and 500 nm.

The underlayer of silver between the substrate and TiO_2 thin film had an impact not only on the films' morphology but also on its thickness. While using the same precursor solution, the pristine TiO_2 thin film was 1.1 µm thick while Ag:TiO_2 was only 0.6 µm thick. This effect was also observed with the niobium doping with a film thickness decreased from 1.5 µm (see table 2.3) to 0.4 µm in the counterpart with the silver underlayer.

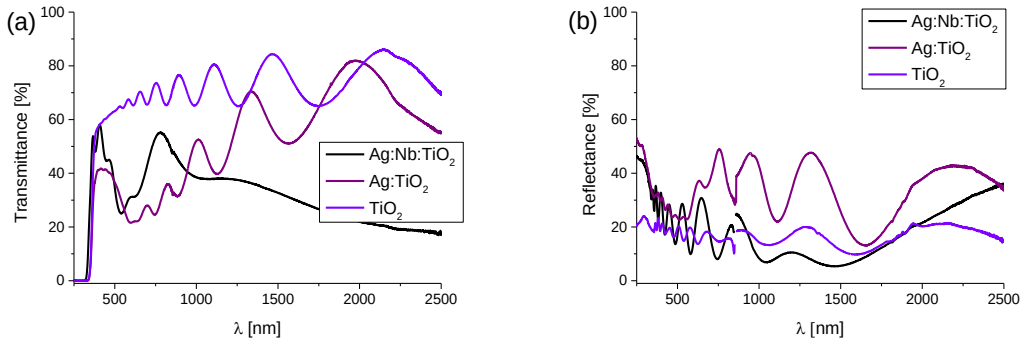

Fig. 4. 6 (a) transmittance and (b) reflectance (%) plot of TiO_2, Ag:TiO_2 and Ag:Nb:TiO_2 thin films over the *UV-vis-IR* range.

UV-vis performance of the Ag:TiO_2 and Ag:Nb:TiO_2 thin films were compared with the pristine TiO_2 thin film. Pristine TiO_2 thin film was transparent from 250 nm onwards and its transparency reached 80% its reflectance spectra remained steady at around 20% throughout the whole spectrum.

The effects of doping on the TiO_2 thin films were visible for Ag:TiO_2 and Ag:Nb:TiO_2 thin films in both transmittance and reflectance spectra. For Ag:TiO_2, thin film transmittance increased from 0% to 40% between 350 and 600 nm and then after dropped to 20% and steadily increased untill the end of measured spectrum to 75%. The reflectance drops from 50% for the 350 nm wavelength and had a minimum of 25% in the 350-600 nm range, and remained steady after increasing to 45%.

Ag:Nb:TiO_2 thin film was transparent (60%) in the 350-520 nm region and then its transparency dropped to 25% in the region between 520 and 650 nm, to increase again to 60% (650-950 nm) and then steadily dropped from 40% to 25% in the 650- 2500 nm range.

Indirect band gap for each film was determined via the Tauc plot using the $(\alpha h\nu)^{1/2}$ relation. The results decreased from 3.19 eV for pristine anatase TiO_2, to 3.12 eV for Ag:TiO_2 and 3.45 eV for the Ag:Nb:TiO_2 thin film.

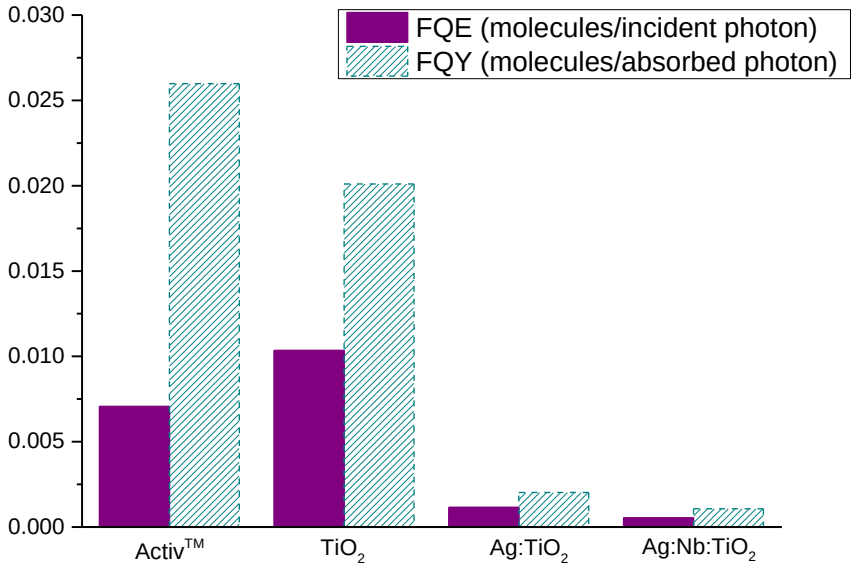

Fig. 4. 7 Comparison of formal quantum efficiency and formal quantum yield of Ag:TiO_2 and Ag:Nb:TiO_2 thin films with Pilkington Activ™.

The photo-catalytic properties of TiO_2, Ag:TiO_2 and Ag:Nb:TiO_2 thin films were investigated using Rezazurin dye and the results were compared with the industry standard Pilkington Activ™. Photo-reduction of the dye was incited by the irradiation of the samples with 365 nm with a *UV* lamp with photon flux of 1.2 x 10^{14} photons cm^{-2} s^{-1} and checked using *UV-vis* spectroscopy between the range 400 and 800 nm. Photo-reduction of dye molecules for Activ™ and the TiO_2 thin film was an order of magnitude higher than of the Ag:$TiO_2$and Ag:Nb:TiO_2 films and was respectively 2.7 x 10^{12},1 x 10^{12}, 4.4 x 10^{11} and 2.0 x 10^{11} dye molecules cm^{-2} s^{-1} for Activ™, TiO_2, Ag:TiO_2 and Ag:Nb:TiO_2 thin films.

Considering the UVA photon flux and photon absorption for all the samples the formal quantum efficiency (the FQE) – the number of molecules destroyed per incident photon, and formal quantum yield (the FQY) – the number of molecules destroyed per absorbed photon, were calculated. The best FQE was found for the TiO_2 thin film (1.0 x 10^{-2} dye molecules per incident photon), followed by Activ™ (7.1 x 10^{-3} dye molecules

per incident photon), the Ag:Nb:TiO_2 thin film (5.4 x 10^{-3} dye molecules per incident photon) and Ag:TiO_2thin film (1.1 x 10^{-3} dye molecules per incident photon). Formal quantum yield was highest for Activ™ (2.6 x 10^{-2} dye molecules per absorbed photon) followed by the TiO_2 thin film (2.0 x 10^{-2} dye molecules per absorbed photon). FQY for both Ag:TiO_2 and Ag:Nb:TiO_2 were an order of magnitude lower than presented by Activ™ and TiO_2 thin film (2.7 and 1.1 x 10^{-3} dye molecules per absorbed photon respectively).

Table 9 Water contact angle measurements of pristine TiO_2, Ag:TiO_2 and Ag:Nb:TiO_2 thin films, performed on as-deposited films, after irradiating them for 2 and 12 h using 254 nm lamp and after storing them in dark place for 24 h.

	Clean [°]	2h 254nm irradiation [°]	12h 254nm irradiation [°]	24h in the dark [°]
TiO_2	46 – 59	21 – 67	< 10	27 – 45
Ag:TiO_2	90 – 92	60 – 66	14 – 18	28 – 36
Ag:Nb:TiO_2	104 – 110	44 – 84	9 – 17	26 – 39

Water contact measurements were performed on Ag:TiO_2 and Ag:Nb:TiO_2 and pristine TiO_2 thin films deposited on glass substrate from the same solution as the investigated samples, without a layer of Ag film. Prior to the measurement samples were washed with propane-2-ol and left to dry in air. Measurements were taken on non-irradiated films, after 1 h and 12 h of 254 nm irradiation and after storing samples for 24 h in the dark.

The as-deposited pristine TiO_2 film displayed hydrophobic properties, water contact angle decreased with irradiation and became super-hydrophilic (water contact angle below 10 °) after 12 h of irradiation.

After 24 h in the dark the film lost its super-hydrophilic properties, but did not return completely to its pre-irradiated state. Ag:TiO_2 and Ag:Nb:TiO_2 thin films displayed similar behaviour to the TiO_2 one. Prior to irradiation they showed hydrophobic properties (water contact angle above 90°), and became more hydrophilic

along with the increasing irradiation time, yet neither of them reached a super-hydrophilic state. After 24 h storage in the dark, water contact angle for both cases increased up to 40° but did not return to the pre-irradiated state.

The Hall effect measurement was performed only on Ag:Nb:TiO_2 thin film, as the Ag:TiO_2 thin film displayed too high a resistivity. The Ag:Nb:TiO_2 thin film displayed *n*-type conductivity as electrons were the prominent type of carrier species, with a resistivity of 3 kΩ/□, charge carrier mobility of 0.016 cm^2/V s and charge carrier concentration of 1.3 x 10^{-17} cm^{-2}.

4.4. Discussion

The presence of the *silver-3c syn* phase in the AgΔT XRD, which was present in neither the Ag:TiO_2 nor Ag:Nb:TiO_2 thin films, indicates that silver instead of remaining in the separate layer, diffuses into the titania phase and either creates a solid solution or becomes dispersed in the TiO_2 as silver NPs. As observed previously[216, 217] silver instead of penetrating into the TiO_2 crystal lattice and creating a covalent bond, creates a heterojunction with the TiO_2.[218-221]

The discrepancy between the atomic ratio of elements in the film measured by EDX and in the surface of the film measured by XPS indicates segregation within the film. Also interesting is the amount of niobium in the film. The starting solution contained 5 atom.%, while the measured amount in the film was almost 4 times higher. This is surprising, as presented in the chapter 2 and 5, the amount of niobium in the TiO_2 structure is usually about 50 – 100% higher than in the starting solution. This might indicate the direct impact of the silver layer on the niobium incorporation and solubility in the TiO_2 lattice.

There is a Ag $3d_{5/2}$ peak shift to the lower position between the AgΔT and Ag:Nb:TiO_2 thin films (365.8 eV and 368.5 eV respectively). Gao *et al.*[110] suggested that

this phenomenon is due to the migration of electrons from the TiO_2 particles to the silver, which indicates a strong interaction between the silver NPs and TiO_2 crystallites at the interface of the heterojunctions.[222]

The studies on the existing literature show that silver/TiO_2 heterojunctions enhance the photocatalytic efficiency[109,111,223-225] by the advantageous trapping of excited electrons from metal particles occupying the TiO_2 surface or by the separate charge transfer resulting with the shifts of the Fermi levels in the silver/TiO_2 heterojunctions to more negative potentials. As shown by the Rezazurin test and water contact angle measurements addition of the silver layer not only does not improve as expected but actually decreases the photocatalytic properties of the TiO_2. This effect is intensified with the niobium doping.

In the Ag:Nb:TiO_2 thin film this can be explained by the fact that even though the silver has diffused through the film to the surface, it has been engaged along with the niobium into lowering the bandgap and increasing the electrical conductivity of TiO_2, therefore accelerating the e^-/h^+ recombination. Moreover since the colour of the film is purple-blue might indicate that silver has undergone reaction with niobium reducing it in the bulk into the Nb^{3+}.

The blue colour of the Ag:TiO_2 thin film indicates reduction of the Ti^{4+} to Ti^{3+}, but since XPS showed no sign of the silver, even in the deep profile, and the film's electrical conductivity could not be measured either using the Hall effect nor crude two point probe, suggests that silver either does not diffuse into the thin film overlayer or diffusion occurs only few atomic layers or nm into the bottom of the film. This is still sufficient to cause surface effect of changed morphology and inhibited photocatalytic properties.

4.5. Conclusion

RF magnetron sputtered layer of silver has not improved the reflectance of the AACVD undoped and niobium doped TiO_2 thin film as expected. Both gold and silver underwent a reaction with the TiO_2 overlayer in the AACVD reactor. While the composite films with silver were well adhered to the substrate, using gold as an underlayer caused the Au:TiO_2 composite films to crumble and flake off when touched, therefore not suitable for the window coating that could be used without a double glazing protection.

As the metallic layer of silver underwent the reaction in the AACVD reactor and turned into the yellowish powder of *silver-3c-syn*, it has lost its ability to reflect the IR light, which resulted in the films with similar IR reflectance as TiO_2 and Nb:TiO_2 thin films. Moreover the addition of silver hinders not only the photocatalytic properties of TiO_2 but also electrical properties of the Nb:TiO_2 thin films. While in the Ag:TiO_2thin film silver remained on the bottom of the film, in the Ag:Nb:TiO_2 thin film it has not only diffused throughout the film but also seemingly increased the niobium solubility in the TiO_2.

5. Hydrothermal synthesis of anatase and rutile niobium doped TiO_2

5.1. Introduction

High temperature processes such as AACVD introduce constraint when choosing both precursors and substrates. In addition the temperature of the process increases the film manufacturing costs.

Previous experimental chapters have described synthesis of pristine, niobium doped and modified niobium doped TiO_2 thin films, both anatase and rutile phase. In each case the technique used was AACVD and the temperature needed for a successful substitutional doping of niobium into the TiO_2 lattice was 500 °C and above.

Low temperature thin film deposition processes such as sol-gel, spin-coating or liquid phase deposition require post-deposition annealing in order to obtain crystalline films. However, in the case of niobium doped titania thin films post-deposition temperature treatment leads to "knocking-out" of niobium from the substitutional position into the interstitial ones. This leads to a significant decrease of electrical conductivity, as well as producing the blue colour of the film.

This introduces the need of a one-step synthesis at a temperature which would be suitable, not only for glass or single crystal substrates, but also for polymers or on the devices with unstable or temperature-sensitive components.

This chapter describes hydrothermal synthesis of both rutile and anatase niobium doped TiO_2, using the same precursors and temperatures, but changing the solution and its pH. After successful doping of niobium into the TiO_2 lattice both of the synthesis routes have been used in order to grow thin films on various substrates including soda lime glass, polycarbonate, FTO and various single crystals.

5.2. Experimental

5.2.1. Chemicals, substrates and synthesis

All chemicals used in this experiment were used without further purification.

Nb doped rutile TiO_2: HCl 37 % (KMG Chemicals) and distilled water were mixed in the same volume proportions and mixed together. 3.6 mmol of reagent grade titanium(IV) butoxide (Sigma Aldrich) and (0-20 atom.% Nb:Ti) niobium powder (Alfa Aesar, 99.8% metal basis) were added to the 30 ml of the mixture of water and HCl and

stirred for 5 min. The mixture was then transferred to a Parr autoclave with the Teflon liner (50 ml capacity, 70 % filling) and heated to 180 °C for 20 h. The obtained precipitate was then washed with deionised water and centrifuged until a neutral pH was reached, and then dried at 40 °C in air.

Nb doped anatase TiO_2: 18 mmol of reagent grade titanium(IV) butoxide (Sigma Aldrich) and 0- 20 atom.% Nb:Ti of Nb powder (Alfa Aesar, 99.8% metal basis) were gradually added into the solution containing 25 ml of 31% hydrogen peroxide (MGC Pure Chemicals Singapore Pte Ltd) and 5 ml of 25 % aqueous ammonia (Honeywell, 0.9 g/ml at 25 °C) under continuous stirring.

The obtained solution was then slowly heated in a water bath in order to evaporate excess ammonia, which resulted in a yellow suspension. The mixture was then transferred to a Parr autoclave with the Teflon liner (50 ml capacity, 70% filling) and heated to 180 °C for 20 h. The obtained precipitate was then washed with deionised water and centrifuged until a neutral pH was reached, and then dried at 40 °C in the air.

Film growth: FTO ($F:SnO_2$, TEC Glass™, 13 Ω/□, Pilkington NSG group); single crystal rutile titanium(IV) oxide <001> TiO_2, lanthanum aluminium oxide <100> $LaAlO_3$ and strontium titanate <100> $SrTiO_3$ (Sigma-Aldrich, 10 mm x 10 mm x 0.5 mm, single side polished), polycarbonate (Sigma-Aldrich, grade makrofol de 1-4, PC, sheet 0.5 x 10 x 10 mm) and soda lime glass (Pilkington NSG group, 10 mm x 10 mm x 1 mm) were used as substrates for the film growth. Each of the substrates was placed in each of the reaction solutions with the film growing side facing down. After the synthesis the substrates were washed with the deionised water and allowed to dry under ambient air.

5.2.2. Material characterisation

For identification of the crystal structure and preferred orientation growth of the film X-ray diffraction (XRD) was used. This was carried out on a *Bruker GADDS D8* diffractometer with a Cu Kα X-ray source and readings were taken over the 15° < 2θ < 80° range. In order to determine unit cell parameters, Rietveld refinement was used to fit the collected data using GSAS and EXPGUI software. To confirm the phase of the film a *WITEC CRM200* Raman spectrometer was used under ambient conditions with an Ar laser source (532 nm) over the 100-1500 cm^{-1} wavelength range. Film morphology was determined using *Scanning Electron Microscopy* (SEM) *JEOL JSM-6301F Field Emission SEM* at accelerating voltage of 5 keV, on the Au-coated samples. Energy dispersive X-ray spectroscopy (EDX- obtained by using a *JEOL JSM-6301F Field Emission SEM*) was used to determine the Nb:Ti atomic ratio on the C-coated samples. Lattice structural information and EDX mapping were examined with *JEOL 2100 TEM* and results were analysed using Gatan software. Measurements of surface composition and the state of elements were carried out using a *Thermo Scientific K-Alpha* X-ray photoelectron spectrometer (XPS) with a monochromatic Al-Kα source. Results were then fitted using *CasaXPS* software with the binding energies suited to carbon (285 eV). Brunauer-Emmett-Teller (BET) surface area measurements were carried out using N_2 in a micrometrics ASAP 2020 Automatic High Resolution Micropore Physisorption Analyzer. The samples were degassed at 70 °C (12 h) under vacuum before measurements.

5.3. Results

5.3.1. Rutile TiO_2

Hydrothermally synthesised Nb doped titania nanoparticles were obtained from a mixture of $Ti(OBu)_4$ and Nb powder in HCl/H_2O 1:1 vol. at 180 °C. Apart from white, pure TiO_2, as-synthesised powders were blue in colour and the intensity of the colour

increased with the niobium amount, up to the niobium incorporation limit, and decreased thereafter.

X-ray diffraction of HCl/H_2O niobium doped TiO_2 powders showed a propagation of phase segregation along with the doping. For 0, 1 and 5 atom.% the undoped TiO_2 and then 1 and 5 atom.% of niobium doped powders showed only the presence of rutile phase of TiO_2. At the 10% level of doping the minor amount of Nb_2O_5 secondary phase was present. At the 20% TiO_2 sample showed the presence of rutile TiO_2, Nb_2O_5 and $TiNb_2O_7$ (**Fig. 5. 1 b**). In order to confirm that niobium is substitutionally incorporated into the rutile TiO_2 lattice the Rietveld refinement was performed on the XRD data. The Nb^{5+} ion radius is 0.03 Å larger than that of Ti^{4+}, which resulted in an expected unit cell expansion. The Raman spectra were consistent with the formation of only the rutile form of TiO_2 in the 0, 1 and 5 atom.% niobium doped TiO_2 powders. Rutile $TiO_2$was also present in the phase segregated 10 and 20 atom.% Nb doped samples.

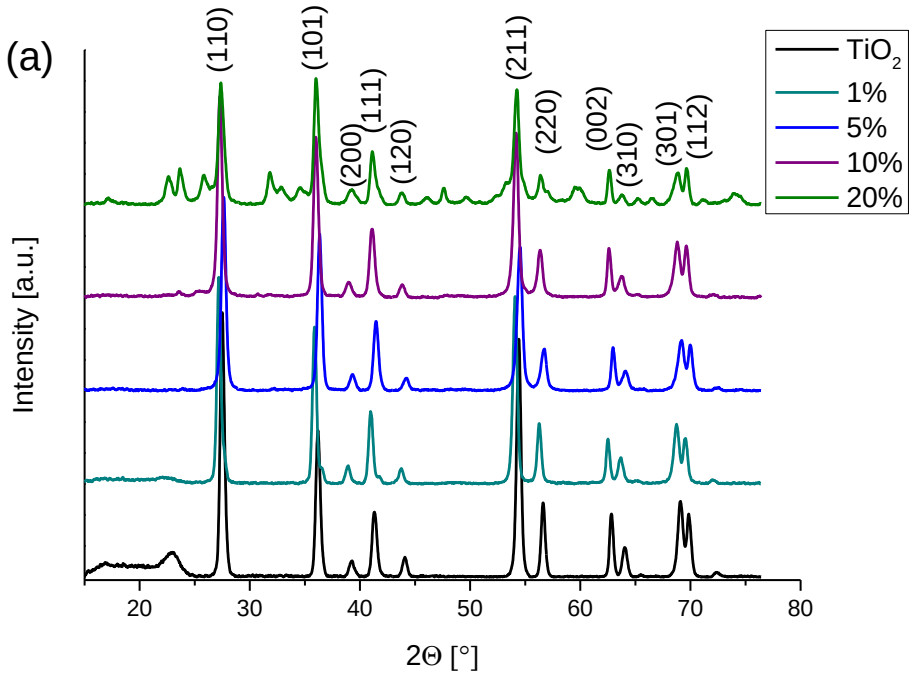

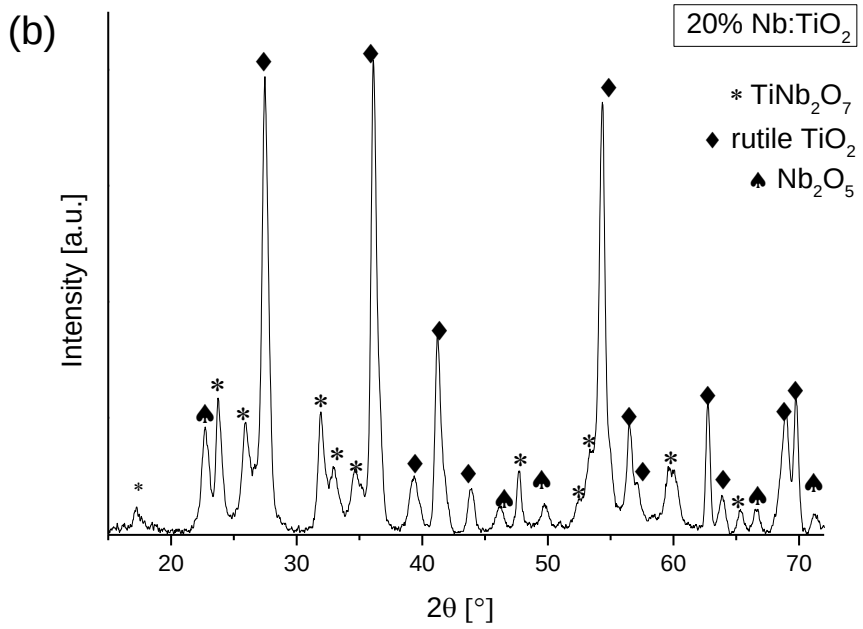

Fig. 5. 1 (a) XRD patterns of Nb doped TiO_2 powders synthesised via hydrothermal method. The rutile TiO_2 reflection positions with appropriate values *(hkl)* are shown in brackets, (b) phase segregation in 20 % Nb doped TiO_2.

Table 10 BET surface analysis and lattice parameters *a, b and c* with increasing Nb. Lattice parameters obtained from Rietveld refinement fitting of models to the data. The associated fitted R_{wp} for the goodness of fit is given also, below 10 % indicates a good fit.

sample	a [Å]	c [Å]	Unit cell volume [Å^3]	R_{wp} (%)	BET surface area [m^2 g^{-1}]
TiO_2	4.5906(58)	2.9557(33)	62.29	5	10
1% Nb:TiO_2	4.6020(81)	2.9567(39)	62.62	10	16
5% Nb:TiO_2	4.6058(51)	2.9594(32)	62.78	8	46
10% Nb:TiO_2	4.6098(36)	2.9616(54)	62.93	7	46
20% Nb:TiO_2					48

The Rietveld refinement was used in order to obtain the unit cell parameters of as-synthesised powders and determine if there was an expansion in the unit cell volume upon doping with niobium. The lattice constants in pristine TiO_2 were a = 4.5906 Å and c = 2.9557 Å and increased gradually upon niobium doping into the system up to a = 4.6098 Å and c = 2.9616 Å for 10% niobium doped TiO_2 (see **Table 10**). Unit cell

volume therefore increased from 62.29 Å^3 for undoped TiO_2 up to 62.93 Å^3 for 10% Nb:TiO_2 indicating, along with the blue colouration of the Nb doped rutile powder, that the niobiumwas substituted into the titania lattice. Due to the phase segregation in the 20% Nb:TiO_2, the Rietveld refinement resulted with the best fit with R_{wp} of 50%, subsequently making it unsuitable for the further analysis and discussion. Although both the blue and white colour of the powder suggested that the niobium was present in two separate species within the powder, one being substutionally doped into the titania lattice and other being a Nb_2O_5 phase.

The BET surface area increased gradually along with the lattice and unit cell expansion upon doping of niobium into the lattice.

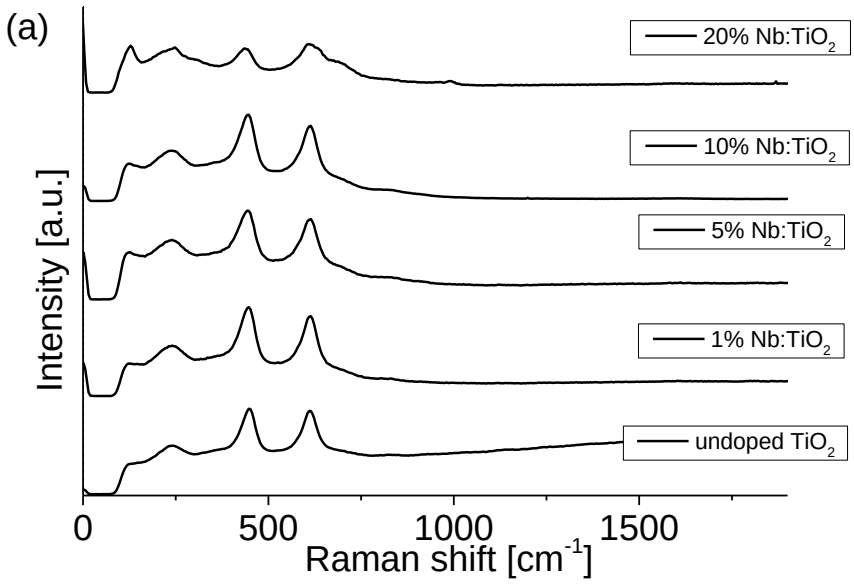

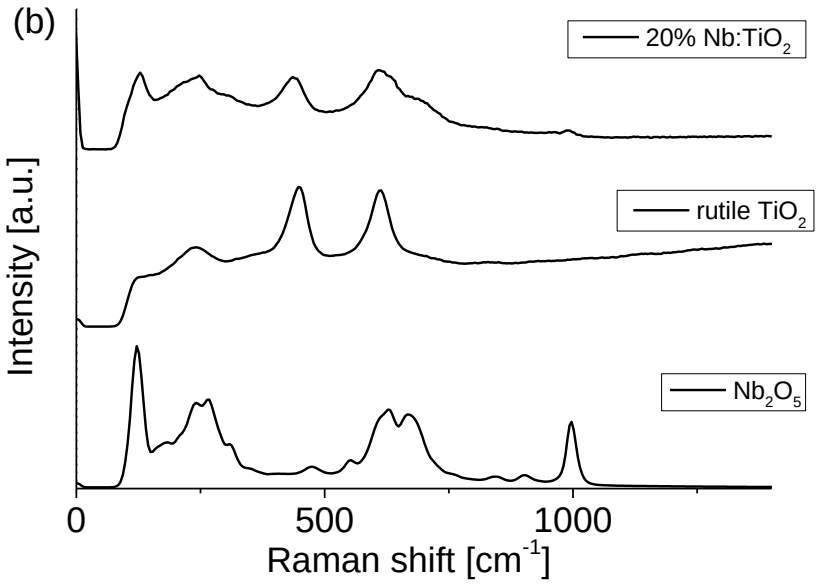

Fig. 5. 2 Raman spectra of the (a) 0-20% niobium doped rutile TiO_2 powders, (b) undoped rutile TiO_2, Nb_2O_5 and phase segregated 20% Nb doped TiO_2.

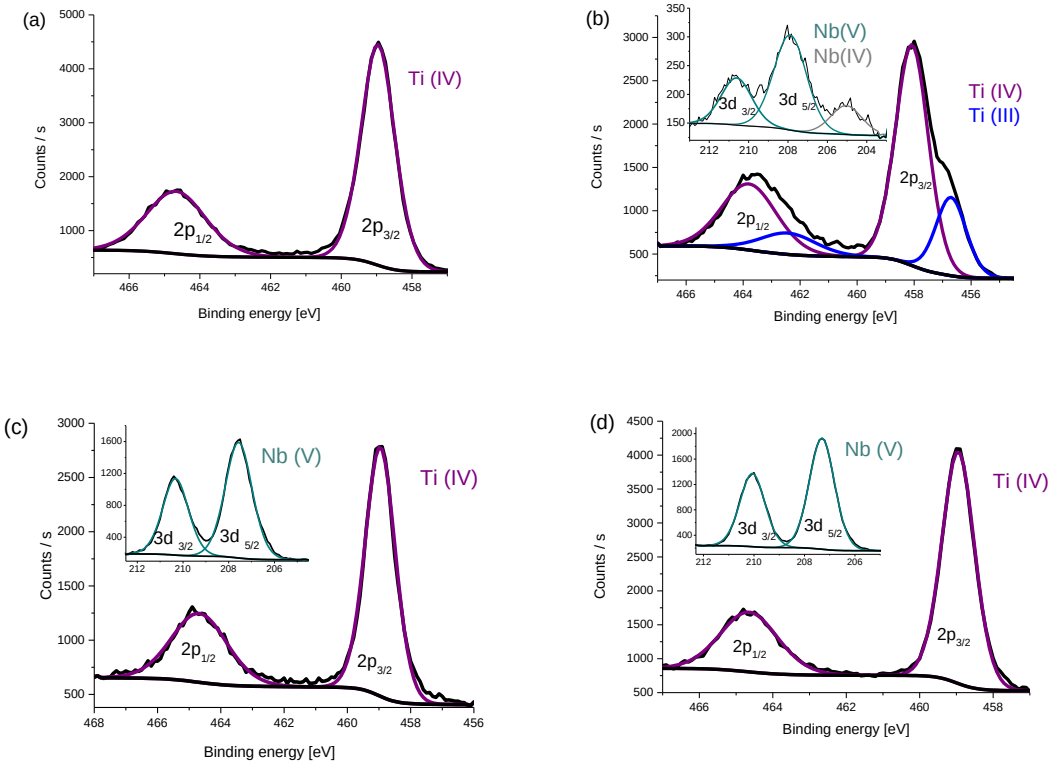

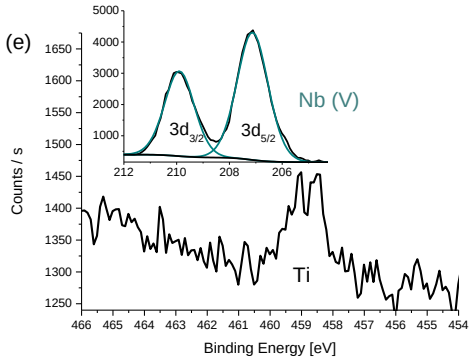

Fig. 5. 3 XPS spectra of (a) undoped TiO_2 (b) 1% (c) 5% (d) 10% (e) 20% Nb doped TiO_2 nanoparticles in the titanium 2p region (inserts show niobium 3d region).

X-ray photoelectron spectroscopy was performed on all samples. For undoped, 5 and 10% Nb:TiO_2 powders the binding energy for the Ti $2p_{3/2}$ excitation was 458.9 ± 0.02 eV, which corresponds with Ti^{4+} in TiO_2. 1% Nb doped titania powders showed the presence of both Ti^{4+} species with the binding energy of 458.1 eV and Ti^{3+} with the binding energy of 456.7 eV[226]. Niobium in the 5 and 10% Nb doped TiO_2 powders fitted only to the Nb^{5+} $3d_{5/2}$ transition states, with binding energies of 207.6 eV and 207.3 eV respectively. The 1% Nb doped TiO_2 powder showed the presence of both Nb^{5+} $3d_{5/2}$ species with the binding energy of 207.8 eV and Nb^{4+} with the binding energy of 205.0 eV.[227] 20% Nb:TiO_2 XPS scans showed the progress of the phase segregation, revealing the amounts of Ti at the surface of the particles was hardly detectable above the noise, and only the Nb^{5+} $3d_{5/2}$ transition states with the binding energy of 207.2 eV corresponding with the Nb^{5+} oxidation state were observed. The blue colouration of the all Nb doped TiO_2 powders suggested the presence of Ti^{3+} and Nb^{4+}, though the concentration of reduced species in all the samples was below the detection limit of the XPS.

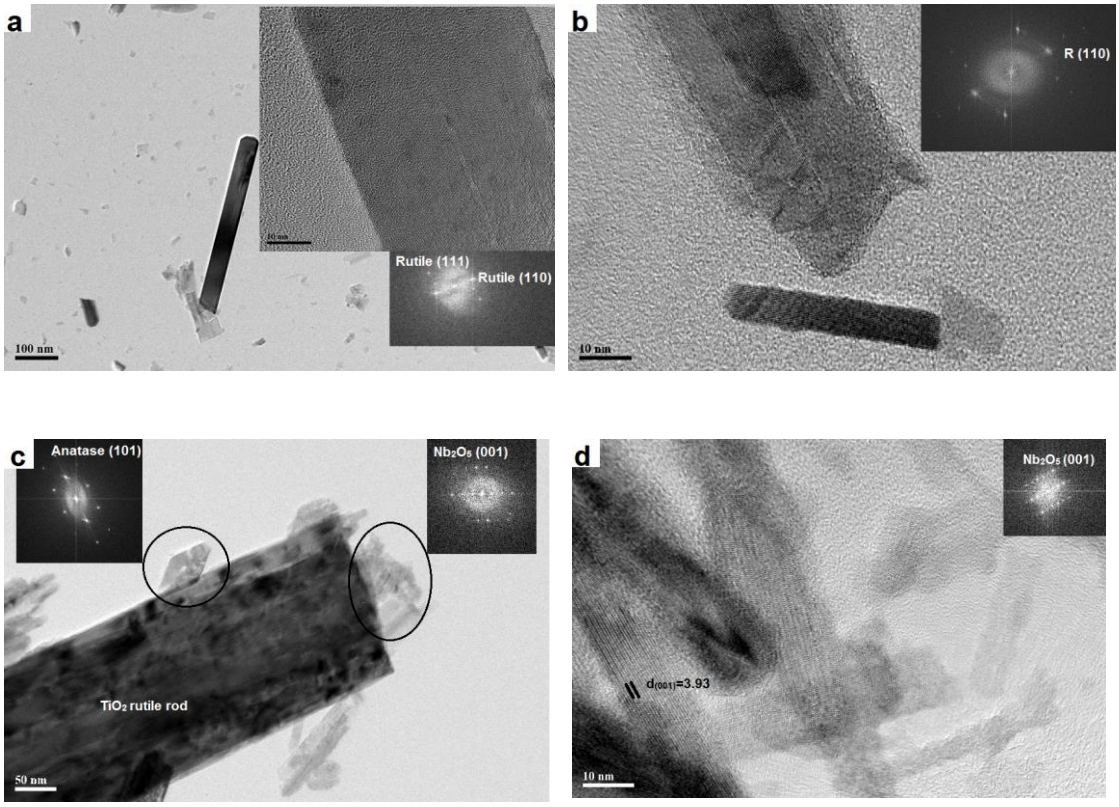

Fig. 5. 4 TEM picture of (a) undoped TiO_2, (b) 5 %, (c) 10 % and (d) 20 % niobium doped TiO_2 as-synthesised powders

High resolution TEM analysis was performed on all samples. Pristine TiO_2 powder consists only of the rutile rods with the sizes varying from 100 nm to 1.5 μm in length. At the 5 % doping level the only phase to be found is rutile forming characteristic rods. At the 10 % doping level the rutile TiO_2 rods can be observed with the anatase TiO_2 characteristic rhombohedrum and Nb_2O_5 particles. Similarly to the pristine TiO_2 powder, the main reflections found in the all the investigated rods were (1 1 1) and (1 1 0) planes, suggesting growth only in this particular crystal orientation. Moreover, all of the investigated by HRTEM crystals showed that (1 1 0) plane was oriented along the longer edge of the crystal for both pristine and doped sample. STEM elemental mapping performed on 5, 10 and 20% niobium doped titania powders show the even distribution of niobium in the titania lattice in the 5 and 10% niobium doped titania powders forming a solid solution. In the 10% niobium doped rutile TiO_2 powder the secondary phase of Nb_2O_5 could also be observed. Conversely, at the 20% doping level

the titanium is still present in the investigated sample, though the particles consist mostly of niobium and oxygen.

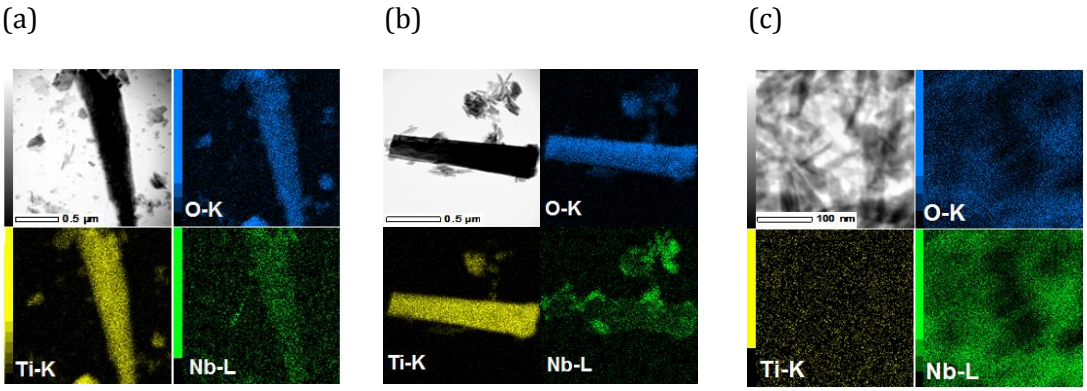

Fig. 5. 5 Elemental mapping of Ti-K (yellow), Nb-L (green) and O-K (blue) of a) 5% b) 10% and c) 20% Nb doped TiO_2.

Table 11 Results of the XPS analysis, showing the binding energies of Ti and Nb; XPS atomic % ratio; EDX atomic % ratio of the niobium doped rutile TiO_2 powders.

At. % of Nb in the solution	Binding energy [eV]				XPS atomic % ratio				EDX atomic % ratio	
	$2p_{3/2}$		Nb $3d_{5/2}$							
	Ti^{4+}	Ti^{3+}	Nb^{5+}	Nb^{4+}	Ti^{4+}	Ti^{3+}	Nb^{5+}	Nb^{4+}	Ti	Nb
0	459.0	-	-	-	100	-	-	-	100	-
1	458.0	456.6	207.8	204.9	70	23	6	1	98	2
5	459.0	-	207.2	-	55	-	45	-	96	4
10	459.0	-	207.3	-	70	-	30	-	97	3
20	458.8	-	207.1	-	5	-	95	-	12	88

EDX analysis (**Table 11**) showed that the for 1 atom.% of niobium in the solution 1.8% was incorporated into the structure, but for the 5 and 10% the amounts were 3.5 and 3% respectively. This suggested that the limit of niobium solubility in the rutile phase of TiO_2 was 3.5% and decreases along with propagation of the phase segregation. For the 20% Nb:Ti ratio in the starting solution the EDX analysis supports previous

findings and showed that in the investigated powder rate of niobium to titanium was 7:1.

5.3.2. Anatase TiO_2

Hydrothermally synthesised Nb doped titania nanoparticles were obtained from the mixture of $Ti(OBu)_4$ and Nb powder in NH_3/H_2O_2 1:5 vol. at 180 °C. Apart from pure, undoped, white TiO_2, as-synthesised powders were blue in colour and the intensity of the colour increased with the niobium amount incorporated into the TiO_2 lattice.

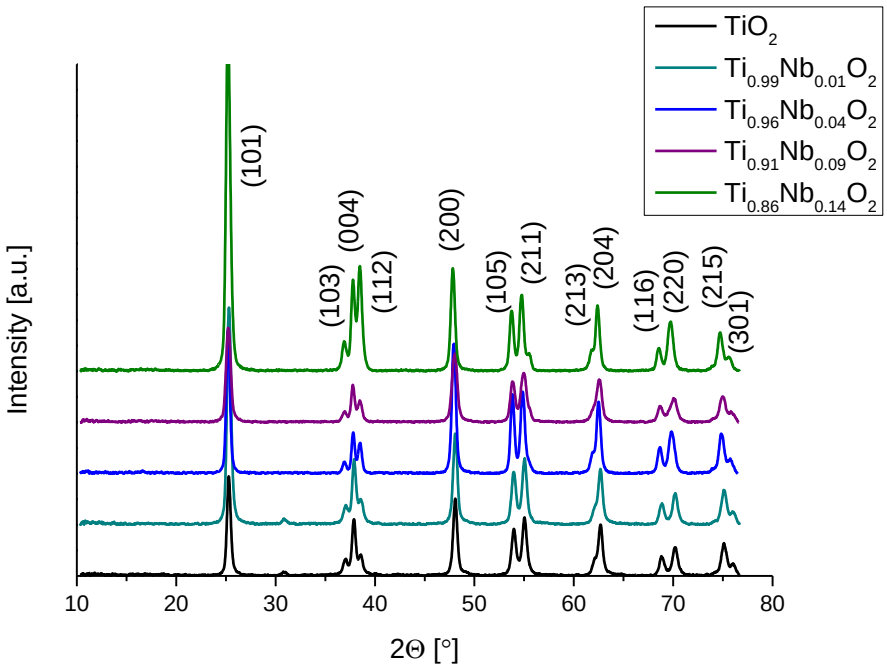

Fig. 5. 6 XRD pattern of Nb doped TiO_2 powders synthesised via hydrothermal method. The anatase reflection positions with appropriate values *(hkl)* are shown in brackets.

X-ray diffraction of the niobium doped TiO_2 powders synthesised from the NH_3/H_2O_2 solution (**Fig. 5. 6**) showed that the only crystalline phase present in all of the samples was anatase form of TiO_2. The phase segregation present in the Nb doped rutile phase of TiO_2 has not occurred in the anatase counterpart using the same amounts of dopant.

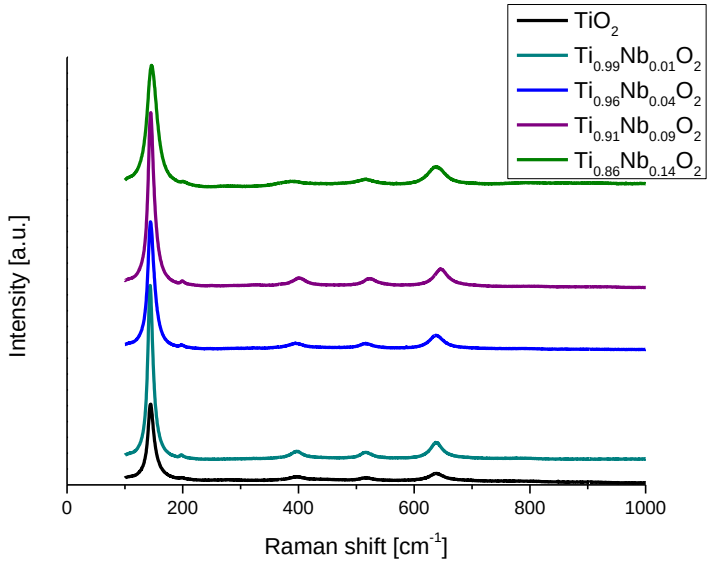

Fig. 5. 7 Raman spectra of the 0-20% niobium doped anatase TiO_2 powders.

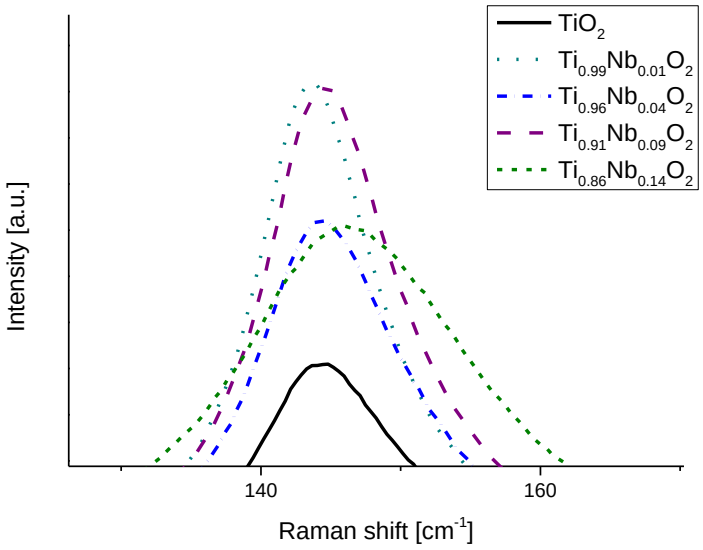

Fig. 5. 8 Shift of E_g band of niobium doped TiO_2 and pristine titania powders.

The Raman patterns were fully consistent with the formation of only the anatase form of TiO_2. Notably the peak at 143 cm^{-1} in pure anatase was shifted to higher energy with niobium doping (**Fig. 5. 7**), which was also observed by Fehse *et al.*[162] and was attributed to the change in O–Ti–O bending vibration. This is also consistent with previous studies based on W-doping into TiO_2.[163] In accordance with the work of Sheppard *et al.*[164] the titania lattice expands in direct proportion with the amount of

niobium concentration in the film. The Raman pattern peaks tend to become broader with niobium content. Despite this broadening, no niobium oxide phase could be detected by Raman.[165, 166]

Table 12 BET surface analysis and lattice parameters *a, b and c* with increasing Nb content. Lattice parameters obtained from Rietveld refinement fitting of models to the data. The associated fitted R_{wp} for the goodness of fit is given also, below 10% indicates a good fit.

sample	a [Å]	c [Å]	Unit cell volume [Å^3]	R_{wp} (%)	BET surface area [m^2 g^{-1}]
TiO_2	3.7939	9.5149	136.95	6	23
$Ti_{0.99}Nb_{0.01}O_2$	3.7940	9.5169	136.99	9	32
$Ti_{0.96}Nb_{0.04}O_2$	3.8105	9.5491	138.65	7	35
$Ti_{0.91}Nb_{0.09}O_2$	3.8014	9.5396	138.00	5	43
$Ti_{0.86}Nb_{0.14}O_2$	3.8149	9.5551	139.06	6	44

The Rietveld refinement was used in order to obtain the unit cell parameters of as-synthesised powders and to determine if there was an expansion in the unit cell volume upon doping with niobium. The lattice constants in pristine TiO_2 were *a* = 3.7939 Å and *c* = 9.5149 Å and increased gradually upon niobium doping into the system up to *a* = 3.8149 Å and *c* = 9.5551 Å for $Ti_{0.86}Nb_{0.14}O_2$ powder (see **Table 12**). Unit cell volume therefore increased from 136.95 Å^3 for undoped TiO_2 up to 139.06 Å^3 for $Ti_{0.86}Nb_{0.14}O_2$ powder indicating that the niobium is substituted into the titania lattice.

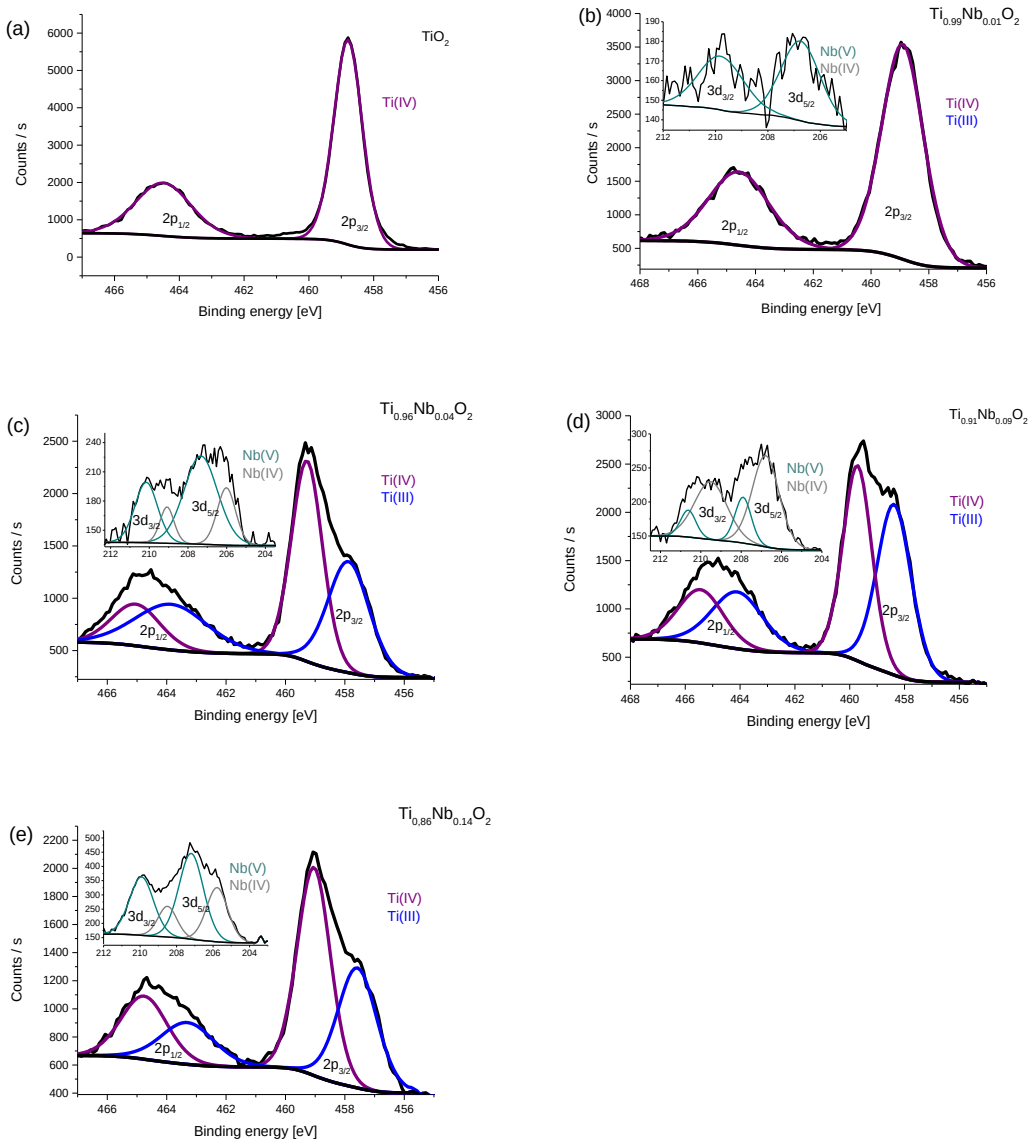

Fig. 5. 9 XPS spectra of anatase (a) TiO_2 (b) $Ti_{0.99}Nb_{0.01}O_2$ (c) $Ti_{0.96}Nb_{0.04}O_2$ (d) $Ti_{0.91}Nb_{0.09}O_2$ (e) $Ti_{0.86}Nb_{0.14}O_2$ powders in the titanium 2p region (inserts show niobium in 3d region).

X-ray photoelectron spectroscopy was performed on all the samples. For undoped TiO_2 and $Ti_{0.99}Nb_{0.01}O_2$ powders the binding energies for the Ti $2p_{3/2}$ excitation were 458.8 and 459.1 eV respectively which corresponds with the Ti^{4+} in TiO_2.[167] Upon further doping with the niobium the analysis of $Ti_{0.96}Nb_{0.04}O_2$, $Ti_{0.91}Nb_{0.09}O_2$ and $Ti_{0.86}Nb_{0.14}O_2$ powders showed the presence of both Ti^{4+} species with the binding energies of 459.3 ± 0.2 eV and Ti^{3+} species with the binding energies of 457.8, 458.3 and 457.6 eV respectively, corresponding with Ti^{3+} in Ti_2O_3.[228] Niobium in the $Ti_{0.99}Nb_{0.01}O_2$

powder was fitted only to the Nb^{5+} $3d_{5/2}$ transition state, with binding energy of 207.4 eV. The analysis of $Ti_{0.96}Nb_{0.04}O_2$, $Ti_{0.91}Nb_{0.09}O_2$ and $Ti_{0.86}Nb_{0.14}O_2$ powders showed the presence of both Nb^{5+} species with the binding energies of 207.5 ± 0.2 eV and Nb^{4+} species with the binding energies of 206.0, 206.8 and 205.8 eV respectively, corresponding with Nb^{4+} in NbO_2.[229] The detailed ratio of both Nb and Ti and their oxidation states is shown in the **Table 13**.

Table 13 Results of the XPS analysis, showing the binding energies of Ti and Nb; XPS atomic % ratio; EDX atomic % ratio of the niobium doped anatase TiO_2 powders.

At. % of Nb in the solution	Binding energy [eV]				XPS atomic % ratio				EDX atomic % ratio	
	$2p_{3/2}$		Nb $3d_{5/2}$		Ti^{4+}	Ti^{3+}	Nb^{5+}	Nb^{4+}	Ti	Nb
	Ti^{4+}	Ti^{3+}	Nb^{5+}	Nb^{4+}						
0	458.8	-	-	-	100	-	-	-	100	-
1	459.1	-	207.4	-	99	-	1	-	99	1
5	459.2	457.8	207.5	206.0	55	41	3	1	96	4
10	459.5	458.3	207.7	206.8	47	49	1	3	91	9
20	459.1	457.6	207.4	205.8	51	35	9	5	86	14

EDX analysis (**Table 13**) showed that for 1 atom.% niobium in a solution, the amount incorporated into the TiO_2 lattice was 1 atom.%. Solutions consisting of 1, 5, 10 and 20 atom.% of niobium resulted in powders containing 1, 4, 9 and 14 atom.% doped into the TiO_2 structure respectively.

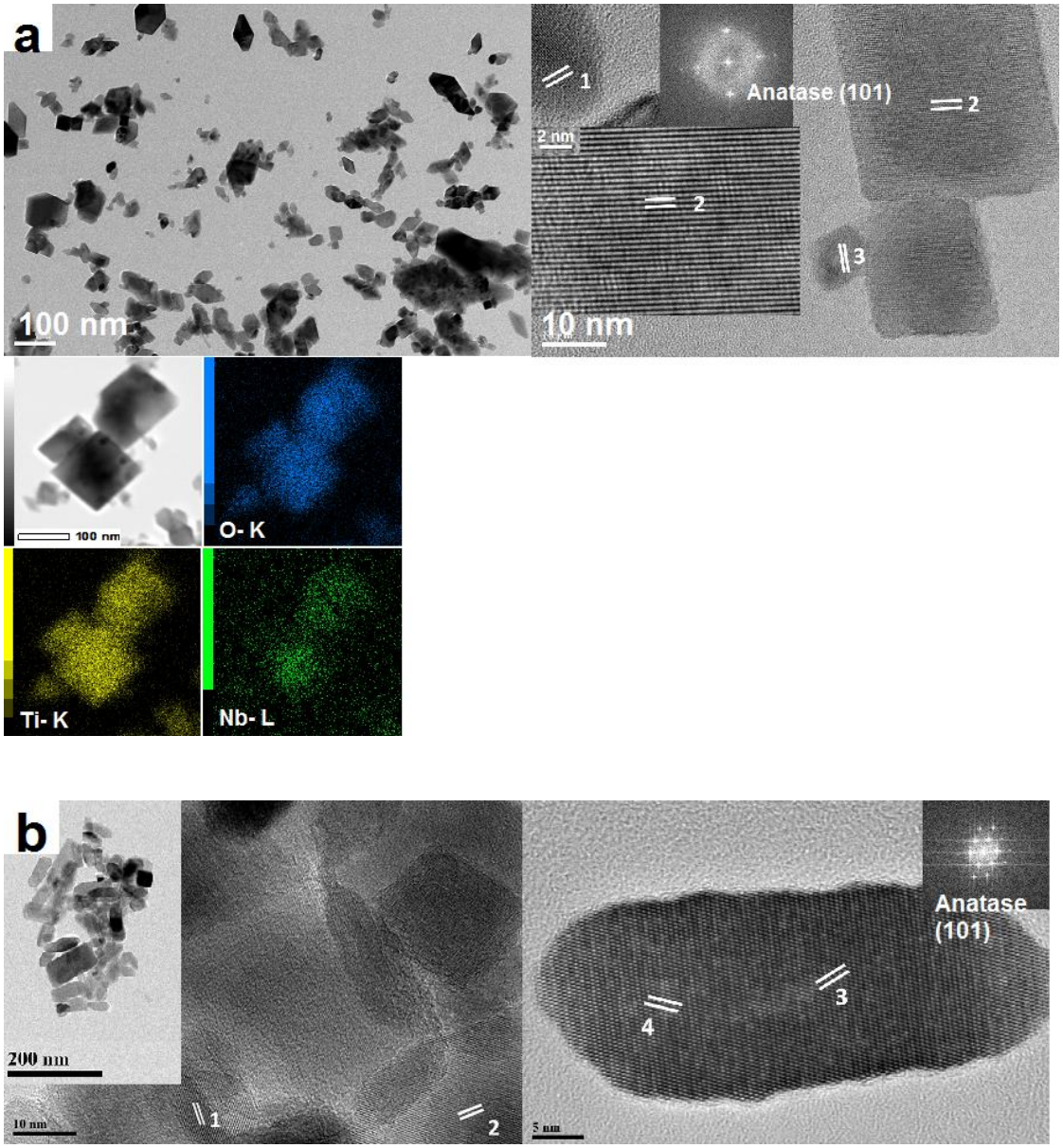

Fig. 5. 10 TEM picture of anatase (a) $Ti_{0.99}Nb_{0.01}O_2$ (number 1 correlates to TiO_2 d_{103} = 2.44±0.02Å, 2 and 3- d_{101} = 3.52±0.01Å) with elemental mapping of O-K, Ti-K and Nb-L, (b) $Ti_{0.86}Nb_{0.14}O_2$ (numbers 1- 4 correlate to TiO_2 d_{101} = 3.51±0.02Å).

Since neither XRD nor Raman analysis revealed any phase segregation, the TEM analysis was performed only on the $Ti_{0.99}Nb_{0.01}O_2$ and $Ti_{0.86}Nb_{0.14}O_2$ samples. In both cases the only phase observed was the anatase form of TiO_2 with the main reflections of (1 0 1) and (1 0 3) plane. The $Ti_{0.99}Nb_{0.01}O_2$ particles had the characteristic rhombohedral shape, though with doping of niobium into the lattice they lose their distinctive sharp edges, becoming coarse in the $Ti_{0.86}Nb_{0.14}O_2$ sample. STEM elemental

mapping was performed on $Ti_{0.99}Nb_{0.01}O_2$ powder, showing even distribution of niobium in the titania lattice and formation of a solid solution.

5.3.3. Film growth

FTO glass, single crystal rutile titanium (IV) oxide (0 0 1) TiO_2, lanthanum aluminium oxide (1 0 0) $LaAlO_3$ and strontium titanate (1 0 0) $SrTiO_3$, polycarbonate and soda lime glass were used as substrates for the film growth. Each of the substrates was placed in each of the reaction solutions with the film growing side facing down. The only positive result obtained were pristine rutile TiO_2 rods grown on the FTO glass (**Fig. 5. 11**), as described by Liu and Aydil[118]. Both niobium doped anatase and rutile precipitated, creating a loose powder described above.

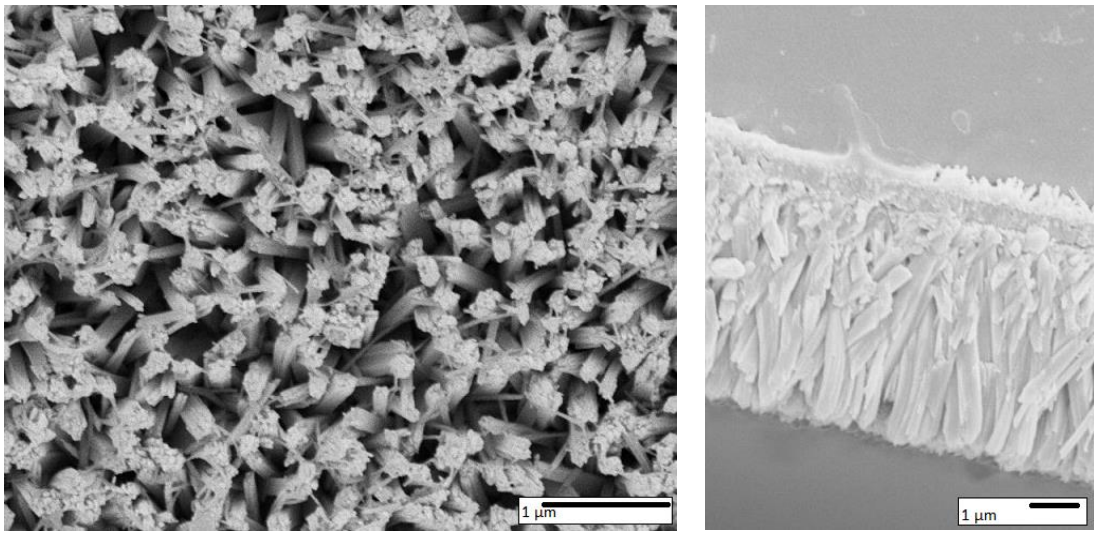

Fig. 5. 11 SEM pictures of the rutile TiO_2 rods grown on the FTO glass.

5.4. Discussion

It seems that not only pH plays a role in the synthesis and formation of different TiO_2 polymorphs, but also the counter ion such as Cl^-, NO_3^-, SO_4^{2-}, $C_2O_4^{2-}$, NH_4^+. Although the formation of rod-like rutile TiO_2 has been observed in the acidic environment *via* - hydrothermal treatment,[230-232] Dambournet *et al.*[26] have reported the synthesis of TiO_2 in the acidic medium (H_2SO_4) with pH = 0.1, which resulted in the formation of the anatase phase, instead of the expected rutile. It was explained that the sulfate species acted as a directing agent, which favours the formation of anatase over the rutile phase of TiO_2. NH_4^+ ions acted similarly to sulfates in the basic environment, also the presence of the amino-agents (both tertiary amines and quaternary ammonium hydroxides) enhances crystallisation process.[233, 234]

The chloride anions by entering the first coordination sphere of titanium form hydroxychloro complexes such as $[Ti(OH)_2Cl_2(H_2O)_2]^0$, $[Ti(OH)_2Cl_3(OH_2)]^-$, $[Ti(OH)_2(OH_2)_4]^{2+}$, $[Ti(OH)_2Cl(OH_2)_3]^+$ and $[Ti(OH)_2Cl_4]^{2-}$ which favour the formation of the rutile phase.[235] Although, as reported by Pottier *et al.* the addition of oxalate or nitrate anions to the chloride solution supports formation of brookite phase of TiO_2. The mechanism of this reaction was explained by the fact that in the aqueous solution titanium is solvated and forms 6-fold-coordinated complexes $[TiL_6]^{x+}$, where L is dictated by the pH and the nature of the solution. When the complexing agent is absent, then the pH plays a major role in the phase formation. In the presence of the complexing species, which can enter the coordination sphere of titanium, the solid phase is likely to form from different zero-charged precursors, resulting in the creation of one particular phase.[26, 236]

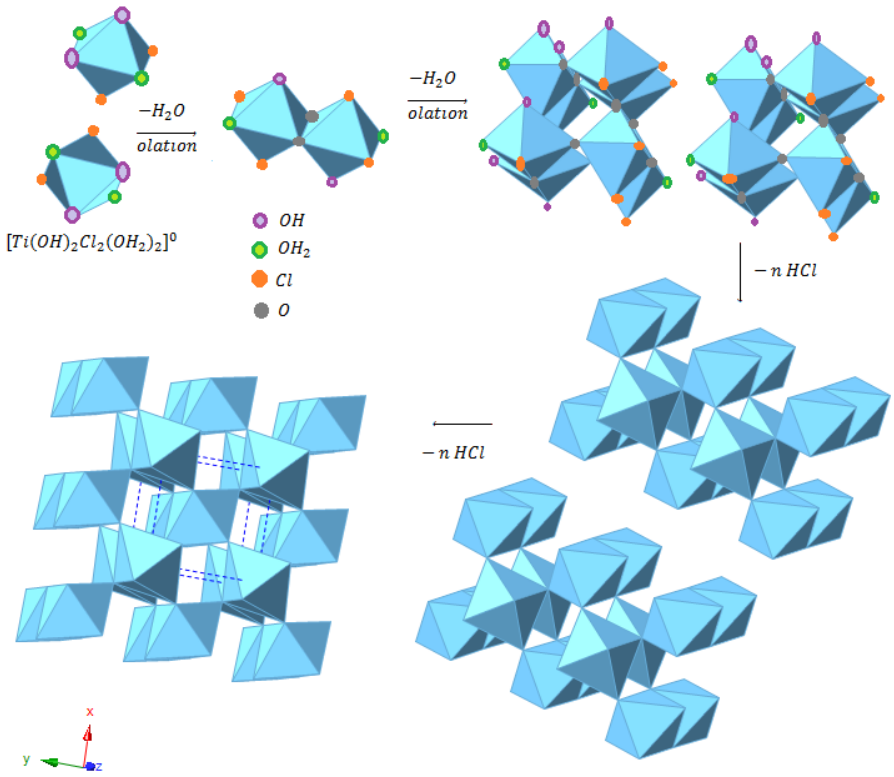

Fig. 5. 12 Possible reaction pathway for rutile formation from one of the proposed complexes.

This theory is in agreement with the formation of niobium doped rutile TiO_2 in the presence of Cl^- ions, even though the presence of niobium atoms as a dopant stabilises the anatase system and inhibits the growth of the rutile phase.[94]

Since the radius of Nb^{5+} is 0.03 Å bigger than the Ti^{4+}, it generates a stress upon substitutional incorporation into the TiO_2 lattice, causing an inhibition of the growth of the TiO_2 crystallites, as described by Sharma *et al.*,[237] which explains the increase of the surface area of both rutile and anatase TiO_2 along with the niobium doping. As shown by Burnside *et al.*[233] the surface area of the TiO_2 particles synthesised in the autoclave varies from 10 to 50 m^2/g, depending on the temperature of the process. Similarly to the results obtained by Arbiol *et al.*[177] the crystal size and surface drastically dropped at the low percentage of niobium doping into the TiO_2 lattice and even though the size and surface area further decreases along with increasing niobium content, the decrease is slower. This trend was clearer in the anatase phase than in rutile. Although it has been

reported that niobium incorporation suppresses coarsening of the TiO_2 grains[238-240] the overall crystallinity of both rutile and anatase Nb:TiO_2 powders presented in this chapter has not been affected. The reason for this effect can be a high temperature and a long time of the synthesis, supporting Ostwald ripening,[241, 242] resulting in obtaining an order of magnitude larger particles compared to the literature.[177, 238, 239]

As shown by Huy *et al.*[243] the incorporation of niobium into the lattice will be more likely to occur in an oxygen-poor environment. In an oxygen-rich environment niobium will therefore prefer to form a pentoxide, instead of acting as a dopant. The dopant solubility in the titania is therefore dependent on two factors, the crystalline phase and the availability of oxygen.

The hydrolysis reaction equilibrium is moved towards the formation of Nb_2O_5 while the TiO_2 remains in the solution. The phase segregation in niobium doped titania starts above 5 atom.% and primarily leads to formation of the insulating phase $TiNb_2O_7$ under an oxidasing atmosphere[239, 244] and, as reported by Huang *et al.*[245] 25 atom.% under reducing atmosphere. Further doping of niobium results in the coexistence of 3 phases TiO_2, $TiNb_2O_7$ and Nb_2O_5, as shown on the 20% niobium doped rutile TiO_2 XRD pattern. As shown in the HRTEM pictures in the 10% Nb:TiO_2 rutile powder, the propagation of the phase segregation started from the presence of nanoclusters of Nb_2O_5 on the surface of rutile rods, which trend was previously described.[177, 246]

In the 10 and 20% rutile Nb:TiO_2 powders niobium existed both as a substitutional dopant and was segregated from the TiO_2 structure, creating both $TiNb_2O_7$ and Nb_2O_5 phases. At the same time the anatase counterpart containing same amount of niobium in the starting solution remained unseparated. The lower solubility of niobium in the rutile phase of TiO_2 compared to anatase can be explained by the differences in the crystal structure and unit cell volume. While the unit cell volume of pristine anatase TiO_2 is 136.95 $Å^3$, pristine rutile's unit cell volume is only 62.29 $Å^3$. Therefore the same

amount of niobium incorporated in the rutile structure will induce more stress than in the case of anatase.

There are reports on the successful synthesis both rutile and anatase Nb:TiO_2 thin films[71, 92, 99, 247, 248] using methods such as CVD, PLD, PVD. LPD methods result in the growth of either anatase or amorphous cation doped TiO_2 thin films.[140, 249, 250] That is a reason why the unsuccessful growth of Nb:TiO_2 thin film *via* hydrothermal method presented in this chapter requires further study.

5.5. Conclusions

Although the reported solubility limits of niobium in the TiO_2 are 20 atom.% for rutile[92, 244, 251] and 25 atom.% for anatase phase,[177] the results obtained *via* hydrothermal synthesis showed that for the rutile phase limit was reached at 3.5 atom.% and for anatase 15 atom.%.

Comparing results obtained in this chapter with the literature study, it can be concluded that the phase segregation in the niobium doped TiO_2 thin films depends on 4 coexisting and co-dependent factors:

- reducing, inert or oxidising environment of the synthesis
- crystal phase of the TiO_2
- form of the synthesised material: film, powder or nanoparticles
- complexing agent.

6. Synthesis of rutile Nb:TiO_2 free-standing thin film at the liquid-air interface

6.1. Introduction

Hitherto, self-assembly at the liquid-air interface of free-standing films were made of either graphene[252-254] or polymer composites.[255, 256] There is a plethora of scientific reports regarding graphene and polymer based materials, there are only a few reporting fabrication of metal oxide free- standing films.[109, 257, 258] Prinz *et al.* report a method of growing InGaAs/GaAs free-standing films that were fabricated while de-bonding from the substrate. Yang *et al.* describe a surfactant-templated synthesis of oriented mesoporous silica films grown at the air-water interface. And He *et al.* reports a synthesis of free-standing TiO_2-NT arrays by a two-step anodization of Ti sheets. This chapter describes synthesis of the Nb doped rutile TiO_2 free-standing inorganic film fabricated *via* single step hydrothermal method, without using any kind of templating and forming a film that was flexible and could be shaped when first taken from the solution.

6.2. Experimental

6.2.1. Film synthesis

All chemicals used in this experiment were used without further purification; 1 ml of technical grade titanium(IV) butoxide (Sigma Aldrich), (10 atom.% Nb:Ti) niobium powder, -325 mesh (Alfa Aesar), 12.5 ml of deionised water and 12.5 ml of 37% HCl (Sigma Aldrich) were mixed together and stirred until obtaining homogenous mixture. The whole mixture was then transported into the Parr autoclave (50% filled) and heated to 180 °C for 20 h. After cooling and leaving the vessel in the fume hood for at least 12 h, the obtained foil was carefully taken out from the autoclave and washed with water and dried in air.

6.2.2. Material characterisation

For identification of the crystal structure of the foil X-ray diffraction (XRD) was used. This was carried out on a *Bruker GADDS D8* diffractometer with a Cu Kα X-ray source and readings were taken over the $10° < 2\theta < 75°$ range. Energy dispersive X-ray spectroscopy (EDX- obtained by using a *JEOL JSM-6301F Field Emission* SEM) was used to determine the Nb:Ti atomic ratio on the C-coated samples. Scanning electron microscopy imaging was used to determine foil morphology and thickness using a *JEOL JSM-6301F Field Emission SEM* at accelerating voltage of 5 keV, on Au-coated samples. Absorbance was measured using a *SHIMADZU UV-3101PC UV-vis-NIR* scanning spectrophotometer. *FT-IR* spectrum was taken using *Perkin Elmer FTIR spectrometer 100.* Electrical properties were measured at room temperature on an Escopia HMS-3000 set up in the Van der Pauw configuration. Measurements were carried out using a current of 1 μA and a 0.58 T permanent magnet on ≈ 1 x 1 cm squares with silver paint

(Agar Scientific) used as ohmic contacts, integrity of which was tested prior to measurements.

6.3. Results and discussion

The free-standing niobium doped rutile TiO_2 film (**Fig. 6. 1**) was synthesised *via* a hydrothermal method without the use of a template at the liquid- air interface. SEM images (**Fig. 6. 4**) revealed that the film was 10 μm thick, with rutile rods creating a stable and merged structure that maintains flexibility and could be shaped within the two minutes window. Decoration of the free-standing TiO_2 film with a conductive layer may lead to nanosized, flexible electrodes for photo-electrochemical,[111] gas sensors or solar panels applications.

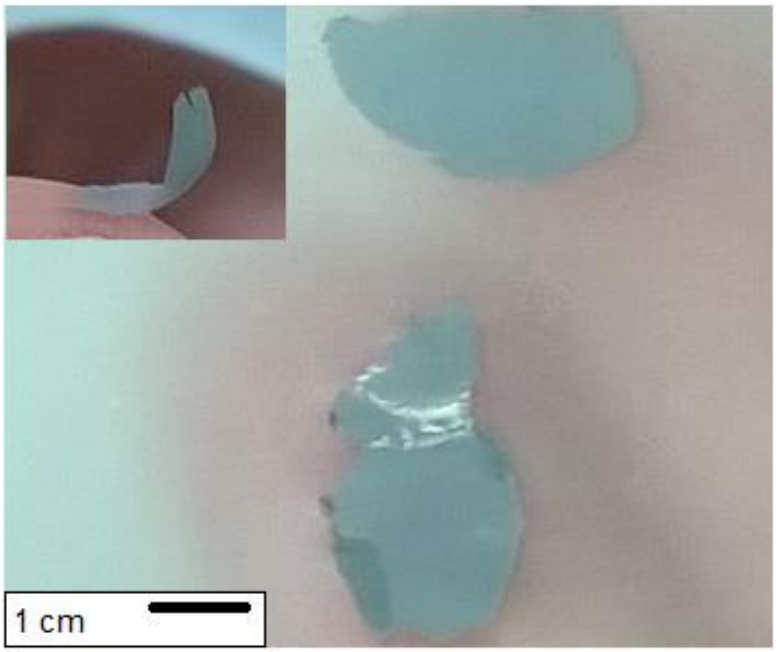

Fig. 6. 1 Image showing niobium doped titania self-assembled foil on the flat surface, insert shows same foil after bending.

Self-assembled niobium doped rutile TiO_2 free-standing films were synthesised *via* a single step hydrothermal method. Although different concentrations of niobium and titanium source were used, the film assembly from the formed powder was observed

only at 10 atom.% Nb:Ti. The rutile film forms at the liquid-air interface and its size was dependent on the diameter of the synthesis vessel. In this experiment a Parr autoclave with a Teflon liner, with the diameter of 2.5 cm was used, therefore the biggest obtained pieces were about 2 cm in diameter.

The film was opaque, blue in colour and was similar to the silica films grown by Yang *et al.;* flexible enough to withstand bending as well as transferring onto cylindrically shaped objects. Although the Nb:TiO_2 film was most flexible shortly after being removed from the solution, after drying in air it behaved like a ceramic material and broke if bent. It could be stored either in common solvents or air and both the colour and shape was stable for over a year. Annealing the film in air at 500 °C for 12 h resulted in a loss of colour yet the macro structure remained unchanged and did not disintegrate into the powder form.

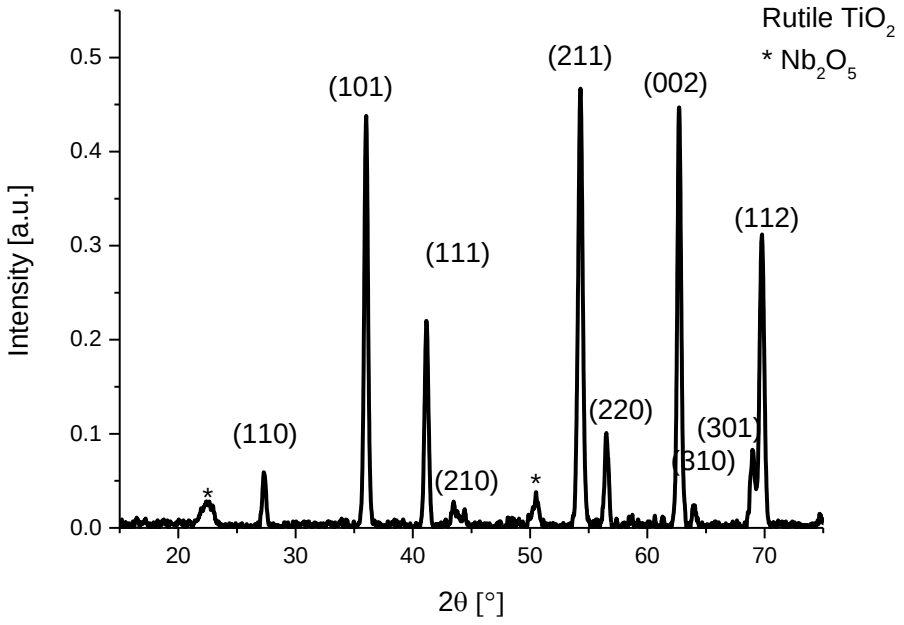

Fig. 6. 2 XRD pattern of niobium doped rutile titania free-standing film. The rutile TiO_2 reflection positions with appropriate values *(hkl)* are shown in brackets.

Niobium was present in two separate species within the film, one being doped into the titania lattice and other being a Nb_2O_5 phase. X-ray diffraction (**Fig. 6. 2**) showed

that the primary phase was rutile TiO_2 with a minor presence of Nb_2O_5 as a secondary phase formed due to the excess of niobium in the starting solution. In order to confirm that niobium was substitutionally incorporated into the rutile TiO_2 lattice the Rietveld refinement was performed on the XRD data collected from the free-standing film and pristine rutile TiO_2 prepared by the same method. Since the Nb^{5+} ion radius is 0.03 Å larger that of Ti^{4+} an expected unit cell expansion was observed from 62.29 $Å^3$ for undoped TiO_2 (a = 4.5906 Å, c = 2.9557 Å, R_{wp} = 5%) to 62.93 $Å^3$ for Nb doped TiO_2 (a = 4.6098 Å, c = 2.9616 Å, R_{wp} = 10%).

EDX analysis showed that even though the starting solution contains 10 atom.% Nb:Ti, the dopant level in the TiO_2 lattice is 3.5 atom.%. This was confirmed by the HR-TEM images of the powder co-precipitated along with the free-standing film. Small amounts of the Nb_2O_5 phase were present on the Nb doped rutile TiO_2 rods. Close TEM examination of the rods showed that the main reflections found in all the investigated rods were rutile TiO_2 (1 1 1) and (1 1 0), with the (1 1 0) plane going along the longer edge of the crystallites (**Fig. 6. 3**).

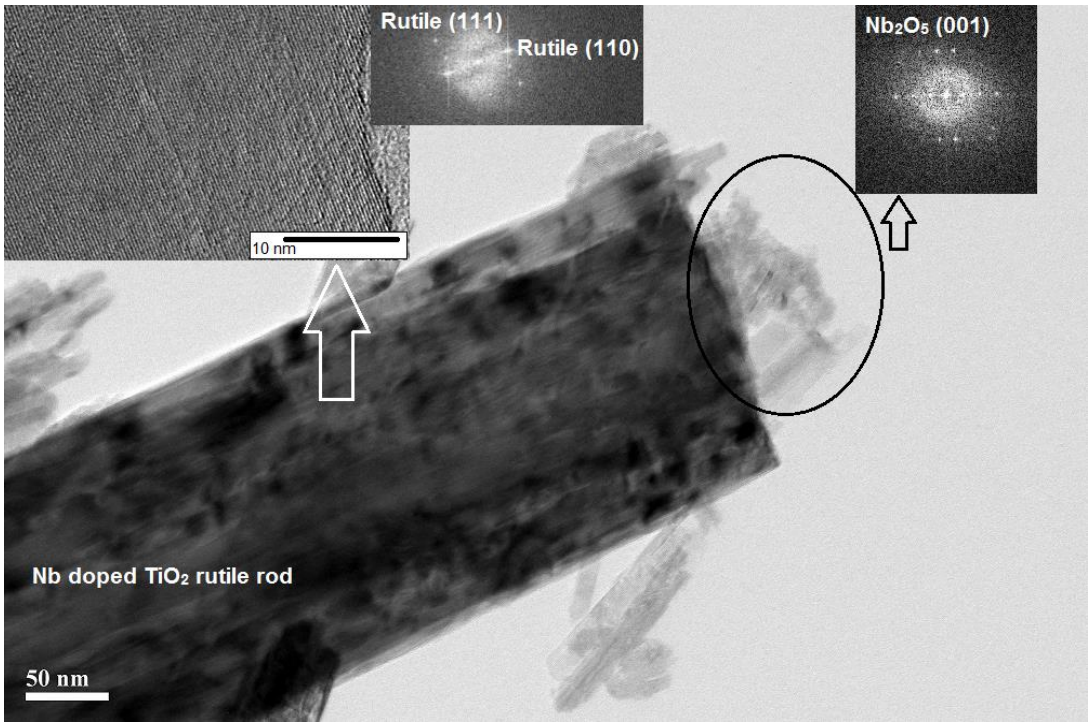

Fig. 6. 3 HR TEM picture of the Nb:TiO_2 powder precipitated from the same solution along with the free-standing film.

SEM images revealed that free-standing film was built of chrysanthemum-like assembled rods with clear centres. This allows one "chrysanthemum" to grow into the side of another and form a solid structure. This characteristic distinguished the Nb doped TiO_2 film from templated silica film[258] or graphene sheets due to its amphiphilicity.[259, 260] Hong *et al.* report the formation of rutile TiO_2 mesocrystals, which were partially linked by an organic medium and partially by the nanocrystals themselves.[261] Linking of the crystallites occurs through a homoepitaxial self-assembly.[262]

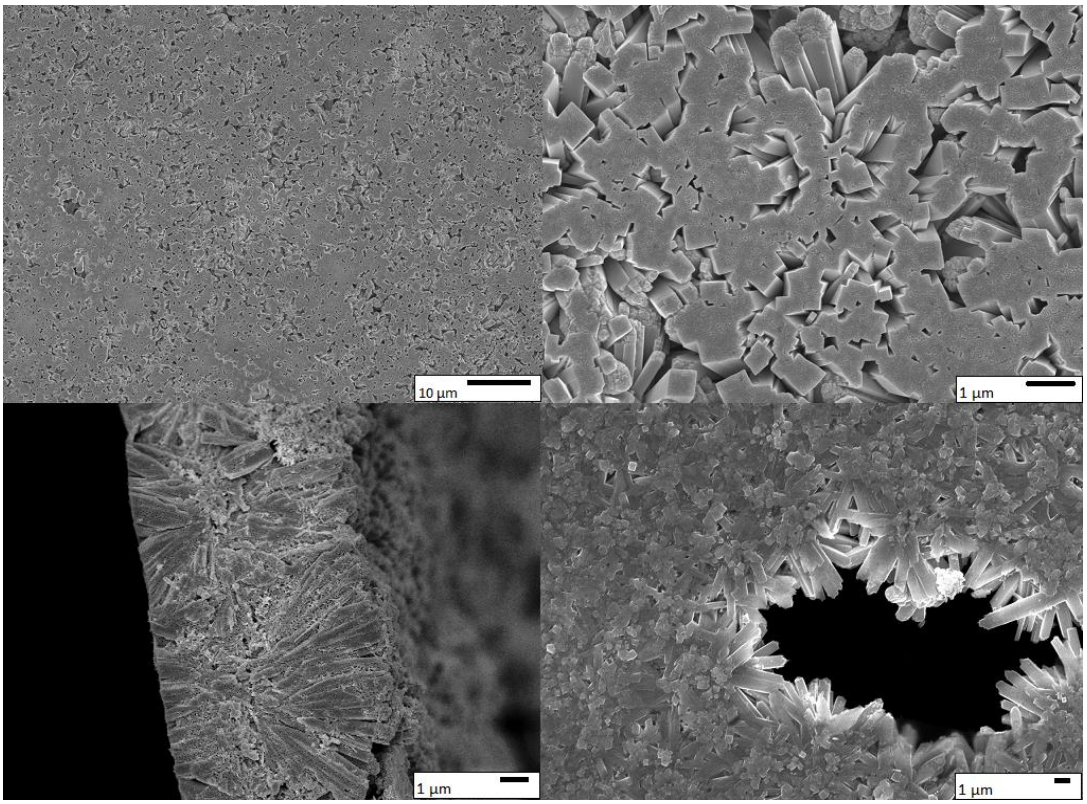

Fig. 6. 4 Top-down and cross-sectional SEM images of the free-standing film.

It was observed that after removal from the solution, the film was flexible when handled. It was surmised that the Nb:TiO_2 rods were formed while the space between them remained in liquid form. The newly formed film became more brittle after several minutes in air which was likely be the due to the evaporation of the solution between the Nb:TiO_2 rutile rods.

Despite successful doping of niobium into the titania lattice, which increases electrical conductivity[204], the Hall effect studies showed that the film remains insulating, most likely due to the pores and micro gaps between the rods.

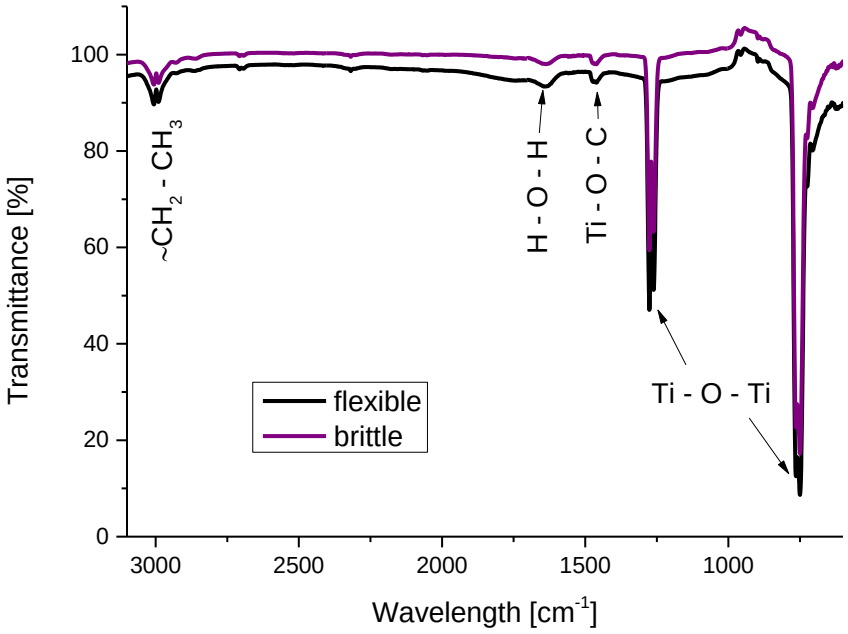

Fig. 6. 5 FT-IR spectra of of the Nb:TiO_2 free standing film. 1st scan was taken immediately after taking the film out of the synthesis vessel and washing it with DI water, when the film is flexible. 2nd scan were taken after 10 min when the film loses its initial flexibility.

In order to understand the loss of flexibility the FT-IR analysis was performed immediately after taking the film out of the synthesis vessel and washing with DI water and after 10 minutes when film loses its initial flexibility (**Fig. 6. 5**). The FT-IR spectra of the Nb:TiO_2 rutile free-standing film showed two distinctive bands at 1275 to 1260 cm^{-1} and 765 to 759 cm^{-1} characteristic for the Ti–O and Ti–O–Ti framework bonds.[263, 264] The 3006 – 2989 cm^{-1} band shows stretching vibrations of unhydrolysed $–CH_2–CH_3$ chains,[265] the 1637 cm^{-1} band can be ascribed to the bending vibration of chemically adsorbed H_2O molecules[263] and the 1462 cm^{-1} band showed the presence of Ti–O–C asymmetric vibrations.[266] The lack of significant changes between the two spectra fails to help understanding the transition between flexible and brittle state.

Soaking the dried film overnight in post-synthesis solution, water or IPA did not restore the flexibility. Yang *et al.* assign the flexibility of their silica film to the thin organic-inorganic composite nature of it. Though the flexibility of the Nb:TiO_2 film might be explained by its macroporous structure. As the elements of the two "chrysanthemums" overlapped and created a continuous film, the rods could rub each other, without breaking the structure.

6.4. Conclusions

In conclusion, this chapter describes one-step hydrothermal method of synthesising a free-standing niobium doped rutile TiO_2 film at the water-air interface without the use of surfactants or other templates.

7. Summary and future work

This thesis has focused on the synthesis and characterisation of niobium doped TiO_2 semiconducting materials, in the forms of films and powders. The work was presented in 5 experimental chapters.

1. First experimental chapter described the synthesis and characterisation of niobium doped anatase TiO_2 thin films *via* AACVD, from a hexane solution, deposited on silica coated float glass at 500 °C. 4 different doping levels from 0 to 10 atom.% were used in order to obtain the best TCO properties, although the electrical resistivity reached a maximum point and started dropping with further doping. Analysis of both the Nb k-edge XANES and EXAFS and the TEM pictures revealed the presence of niobium both incorporated into the titanium dioxide lattice, as well as being present in the form of Nb_2O_5, which had an impact on the optical and electrical properties. The presence of niobium (V) oxide nanocrystals within titania structure increased resistivity of the film and its optical transparency. The results obtained in this chapter have set a bench mark for the next experiments described in this thesis.
2. The second experimental chapter shows AACVD of pristine and niobium doped TiO_2 over a FTO substrate in order to achieve the rutile form of TiO_2 by templating the lattice. Although obtaining pure continuous rutile TiO_2thin film proved to be impossible using the synthesis routes chosen, the work presented revealed that the FTO acts both as a lattice template affecting the morphology, dopant ratio, electrical properties of the films and directing the dopant into the interstitial site of the titania lattice when

using hexane as a solvent; or as one of the precursors when using methanol.

3. Nb:TiO_2 thin films described in chapter 2 did not display sufficient IR reflectivity to be considered as a low-e window glazing. Therefore a RF magnetron sputtered thin layer of gold and silver was introduced prior to the AACVD of Nb:TiO_2. While the composite with silver was well adhered to the substrate, films with the underlayer of gold were flaking off, which discarded them as a window coating. The layer of metallic silver underwent the reaction in the AACVD reactor and transformed into the *silver-3c-syn*, due to which it lost its ability to reflect IR light. Moreover, the addition of silver hindered both the photocatalytic and electrical properties of TiO_2 and Nb:TiO_2 thin films. Interestingly, the niobium doping caused the silver migration throughout the film and the presence of silver increased niobium solubility in the TiO_2.
4. In the 4th experimental chapter the synthesis of niobium doped rutile and anatase phases of TiO_2 *via* hydrothermal synthesis, with the successful substitutional doping of niobium into the titania lattice at 180 °C was described. This chapter focuses on the differences in the behaviour of the two most common TiO_2 phases upon niobium doping,
5. Synthesis route for rutile Nb:TiO_2 described in the previous chapter, upon altering the concentration of the precursors has led to the composition of the free-standing film formed at the water-air interface. The film was obtained without the use of any surfactants or templates and displayed a certain level of flexibility within a two minute window after removal from the solution.

Niobium solubility in TiO_2 and phase segregation play important role in tailoring the semiconducting properties of this material. They not only depend on the crystalline structure but also on the form of the material and the presence of other elements and compounds. In the Nb:TiO_2 anatase thin film synthesised *via* AACVD the phase segregation started occurring at the 8 atom.% of niobium loading, while loose powders of anatase contained up to 14 atom.% without signs of phase segregation. This can be attributed to the additional stress on the structure which is induced on the material by the polycrystalline nature of the film and the preferred orientation of the crystallites. The presence of tin and its oxides decreased niobium solubility and prevented its substitutional doping into the titania lattice, while the presence of silver increased the solubility and hindered the phase segregation.

It can be concluded that the solubility and phase segregation in the niobium doped TiO_2 thin films depends on 4 coexisting and co-dependent factors:

- reducing, inert or oxidising environment of the synthesis
- crystal phase of TiO_2
- form of the synthesised material: film, powder or nanoparticles
- presence of other elements of compounds.

As the first 3 factors have been widely investigated, the fourth one opens an exploration route for the composite and co-doped materials consisting of Nb:TiO_2 with tailored properties.

Publications

List of publications associated with this thesis:

[1] **A. J. Gardecka**, G. K. L. Goh, G. Sankar, I. P. Parkin, On the nature of niobium substitution in niobium doped titania thin films by AACVD and its impact on electrical and optical properties, *Journal of Matrials Chemistry A,* 2015, **3**, 17755-17762.

[2] **A. J. Gardecka**, G. K. L. Goh, G. Sankar, I. P. Parkin, Synthesis of rutile Nb:TiO_2 free-standing thin film at the water-air interface, *Adv. Mater. Interfaces*, 2016, **3**, 1600361

[3] **A. J. Gardecka**, M. Lübke, C. Armer, Z. Liu, G. K. L. Goh, J. A. Darr, I. P. Parkin, Oriented single-crystalline niobium doped rutile TiO_2 nanorods for lithium-ion batteries, 2016 (Manuscript in preparation)

[4] M. Lübke, C. Armer, **A. J. Gardecka**, I. P. Parkin, Z. Liu, J. A. Darr, Investigation of the Electrochemical Activity of Nb-doped rutile TiO_2 in Lithium-ion Batteries, 2016 (Manuscript in preparation)

References

1. C. G. Granqvist, *Sol. Energ. Mater. Sol. Cells*, 2007, **91**, 1529-1598.

2. K. Badeker, *Ann. Phys*, 1907, **22**, 749.

3. A. D. Rakić, A. B. Djurišić, J. M. Elazar and M. L. Majewski, *Appl. Opt.*, 1998, **37**, 5271-5283.

4. R. B. H. Tahar, T. Ban, Y. Ohya and Y. Takahashi, *J. Appl. Phys.*, 1998, **83**, 2631-2645.

5. M. S. Farhan, E. Zalnezhad, A. R. Bushroa and A. A. D. Sarhan, *Int. J. Precision Engineering and Manufacturing*, 2013, **14**, 1465-1469.

6. N. Noor and I. P. Parkin, *J. Mater. Chem. C*, 2013, **1**, 984-996.

7. E. Fortunato, D. Ginley, H. Hosono and D. C. Paine, *MRS bulletin*, 2007, **32**, 242-247.

8. E. Fortunato, A. Goncalves, A. Marques, A. Viana, H. Aguas, L. Pereira, I. Ferreira, P. Vilarinho and R. Martins, *Sur. Coat. Tech.*, 2004, **180**, 20-25.

9. S.-M. Park, T. Ikegami and K. Ebihara, *Thin Solid Films*, 2006, **513**, 90-94.

10. K. E. Lee, M. Wang, E. J. Kim and S. H. Hahn, *Curr. Appl. Phys.*, 2009, **9**, 683-687.

11. K. H. Kim, K. C. Park and D. Y. Ma, *J. Appl. Phys.*, 1997, **81**, 7764-7772.

12. S. Major, A. Banerjee and K. Chopra, *Thin Solid Films*, 1983, **108**, 333-340.

13. H. Hosono, *J. Non-Crystalline Solids*, 2006, **352**, 851-858.

14. K. Nomura, A. Takagi, T. Kamiya, H. Ohta, M. Hirano and H. Hosono, *Jpn J. Appl. Phys.*, 2006, **45**, 4303.

15. H. Yabuta, M. Sano, K. Abe, T. Aiba, T. Den, H. Kumomi, K. Nomura, T. Kamiya and H. Hosono, *Appl. Phys. Lett.*, 2006, **89**, 2123.

16. R. M. Pasquarelli, D. S. Ginley and R. O'Hayre, *Chemical Society Reviews*, 2011, **40**, 5406-5441.

17. H. Zhang, B. Wu, W. Hu and Y. Liu, *Chem. Soc. Rev.*, 2011, **40**, 1324-1336.

18. T. L. Thompson and J. T. Yates, *Chem. Rev.*, 2006, **106**, 4428-4453.

19. U. Diebold, *Surf. Sci. Rep.*, 2003, **48**, 53-229.

20. O. Carp, C. L. Huisman and A. Reller, *Prog. Solid State Chem.*, 2004, **32**, 33-177.

21. U. Kirner, K. Schierbaum, W. Göpel, B. Leibold, N. Nicoloso, W. Weppner, D. Fischer and W. Chu, *Sensors and Actuators B: Chemical*, 1990, **1**, 103-107.

22. E. Garfunkel and E. Gusev, *Fundamental Aspects of Ultrathin Dielectrics on Si-based Devices*, Springer Science & Business Media, 2012.

23. H. Selhofer, E. Ritter and R. Linsbod, *Appl. Opt.*, 2002, **41**, 756-762.

24. S. Noimark, C. W. Dunnill, M. Wilson and I. P. Parkin, *Chem. Soc. Rev.*, 2009, **38**, 3435-3448.

25. P. Carmichael, D. Hazafy, D. S. Bhachu, A. Mills, J. A. Darr and I. P. Parkin, *Phys. Chem. Chem. Phys.*, 2013, **15**, 16788-16794.

26. D. Dambournet, I. Belharouak and K. Amine, *Chem. Mater.*, 2009, **22**, 1173-1179.

27. F. Grant, *Rev. Mod. Phys.*, 1959, **31**, 646.

28. L. S. Dubrovinsky, N. A. Dubrovinskaia, V. Swamy, J. Muscat, N. M. Harrison, R. Ahuja, B. Holm and B. Johansson, *Nature*, 2001, **410**, 653-654.

29. L. Kavan, M. Gratzel, S. E. Gilbert, C. Klemenz and H. J. Scheel, *J. Am. Chem. Soc.*, 1996, **118**, 6716-6723.

30. A. Fahmi, C. Minot, B. Silvi and M. Causa, *Phys. Rev. B*, 1993, **47**, 11717.

31. J. Banfield, *Journal of Materials Chemistry*, 1998, **8**, 2073-2076.

32. H. Zhang and J. F. Banfield, *J. Phys. Chem. B*, 2000, **104**, 3481-3487.

33. J. F. Banfield, B. L. Bischoff and M. A. Anderson, *Chem. Geol.*, 1993, **110**, 211-231.

34. M. Boehme and W. Ensinger, *Nano-Micro Lett.*, 2011, **3**, 236-241.

35. G. Odling and N. Robertson, *Chemsuschem*, 2015, **8**, 1838-1840.

36. T. Luttrell, S. Halpegamage, J. Tao, A. Kramer, E. Sutter and M. Batzill, *Sci. Rep.*, 2014, **4**, 4043.

37. H. Tang, K. Prasad, R. Sanjines, P. Schmid and F. Levy, *J. Appl. Phys.*, 1994, **75**, 2042-2047.

38. J. G. Speight, *Lange's handbook of chemistry*, McGraw-Hill New York, 2005.

39. F. Kröger and H. Vink, *J. Phys. Chem. Solids*, 1958, **5**, 208-223.

40. L. Van der Pauw, *Philips Res. Rep.*, 1961, **16**, 187-195.

41. L. Solymar, D. Walsh and R. R. Syms, *Electrical properties of materials*, OUP Oxford, 2014.

42. G. Parker, *Introductory semiconductor device physics*, CRC Press, 2004.

43. H. T. Grahn, *Introduction to semiconductor physics*, World Scientific, 1999.

44. B. Yacobi, *Semiconductor materials: an introduction to basic principles*, Springer Science & Business Media, 2003.

45. W. Strehlow and E. Cook, *J. Phys. Chem. Ref. Data*, 1973, **2**, 163-200.

46. W. Choi, A. Termin and M. R. Hoffmann, *J. Phys. Chem.*, 1994, **98**, 13669-13679.

47. K. O'Donnell and X. Chen, *Appl. Phys. Lett.*, 1991, **58**, 2924-2926.

48. D. F. Ollis and H. Al-Ekabi, *Photocatalytic purification and treatment of water and air: proceedings of the 1st International Conference on TiO2 Photocatalytic Purification and Treatment of Water and Air, London, Ontario, Canada, 8-13 November, 1992*, Elsevier Science Ltd, 1993.

49. P. V. Kamat, *Chem. Rev.*, 1993, **93**, 267-300.

50. E. Pelizzetti and N. Serpone, *Homogeneous and heterogeneous photocatalysis*, Springer Science & Business Media, 2012.

51. N. Serpone and E. Pelizzetti, *Photocatalysis: fundamentals and applications*, Wiley New York, 1989.

52. A. Fujishima, *Nature*, 1972, **238**, 37-38.

53. A. L. Linsebigler, G. Lu and J. T. Yates Jr, *Chem. Rev.*, 1995, **95**, 735-758.

54. M. A. Fox and M. T. Dulay, *Chem. Rev.*, 1993, **93**, 341-357.

55. A. Fujishima, T. N. Rao and D. A. Tryk, *J. Photochem. Photobiol. C: Photochemistry Rev.*, 2000, **1**, 1-21.

56. Y. Nosaka and M. A. Fox, *J. Phys. Chem.*, 1988, **92**, 1893-1897.

57. R. Zallen and M. Moret, *Solid State Commun.*, 2006, **137**, 154-157.

58. A. Nakajima, S.-i. Koizumi, T. Watanabe and K. Hashimoto, *Langmuir*, 2000, **16**, 7048-7050.

59. D. Mardare and G. Rusu, *J. Optoelectron. Adv. Mater.*, 2001, **3**, 95-100.

60. K. Page, M. Wilson and I. P. Parkin, *J. Mater. Chem.*, 2009, **19**, 3819-3831.

61. S. Malato, P. Fernández-Ibáñez, M. Maldonado, J. Blanco and W. Gernjak, *Catal. Today*, 2009, **147**, 1-59.

62. A. Mills, J. Wang and M. McGrady, *J. Phys. Chem. B*, 2006, **110**, 18324-18331.

63. J. Straube and P. Eng, *J. B. E. D. Winter*, 2010, 13-15.

64. A. Roos, P. Polato, P. A. Van Nijnatten, M. G. Hutchins, F. Olive and C. Anderson, *Solar Energy*, 2001, **69**, 15-26.

65. S. Huang, Z. Wang, J. Xu, L. Wang, D. Lu and T. Yuan, *Thin Solid Films*, 2009, **517**, 2963-2967.

66. F. Ungureanu, R. Medianu, R. Ghita, C. Negrila, P. Ghita, A. Manea and M. Lazarescu, *J. Optoelectron. Adv. Mater.*, 2007, **9**, 1457-1461.

67. L. Sheppard, T. Bak and J. Nowotny, *J. Phys. Chem. B*, 2006, **110**, 22447-22454.

68. A. Kafizas, C. W. Dunnill and I. P. Parkin, *J. Mater. Chem.*, 2010, **20**, 8336-8349.

69. A. Mills and S. Le Hunte, *J. Photochem. Photobiol. A: Chem.*, 1997, **108**, 1-35.

70. C. H. Heo, S.-B. Lee and J.-H. Boo, *Thin Solid Films*, 2005, **475**, 183-188.

71. M. Atashbar, H. Sun, B. Gong, W. Wlodarski and R. Lamb, *Thin Solid Films*, 1998, **326**, 238-244.

72. M. Ni, M. K. Leung, D. Y. Leung and K. Sumathy, *Renew. Sust. Energ. Rev.*, 2007, **11**, 401-425.

73. A. Yoshino, *Angew. Chem. Int. Ed.*, 2012, **51**, 5798-5800.

74. O. W. Johnson, *Phys. Rev.*, 1964, **136**, A284-A290.

75. M. V. Koudriachova, N. M. Harrison and S. W. de Leeuw, *Solid State Ionics*, 2003, **157**, 35-38.

76. M. V. Koudriachova, N. M. Harrison and S. W. de Leeuw, *Phys. Rev. B*, 2002, **65**, 235423.

77. M. V. Koudriachova, N. M. Harrison and S. W. de Leeuw, *Phys. Rev. Lett.*, 2001, **86**, 1275.

78. A. Stashans, S. Lunell, R. Bergström, A. Hagfeldt and S.-E. Lindquist, *Phys. Rev. B*, 1996, **53**, 159.

79. Z. Yang, D. Choi, S. Kerisit, K. M. Rosso, D. Wang, J. Zhang, G. Graff and J. Liu, *J. Power Sources*, 2009, **192**, 588-598.

80. E. Baudrin, S. Cassaignon, M. Koelsch, J. P. Jolivet, L. Dupont and J. M. Tarascon, *Electrochem. Commun.*, 2007, **9**, 337-342.

81. Y. S. Hu, L. Kienle, Y. G. Guo and J. Maier, *Adv. Mater.*, 2006, **18**, 1421-1426.

82. B. N. Joshi, H. Yoon, M. F. Hest and S. S. Yoon, *J. Am. Cer. Soc.*, 2013, **96**, 2623-2627.

83. D. O. Scanlon, C. W. Dunnill, J. Buckeridge, S. A. Shevlin, A. J. Logsdail, S. M. Woodley, C. R. A. Catlow, M. J. Powell, R. G. Palgrave and I. P. Parkin, *Nature Mater.*, 2013, **12**, 798-801.

84. P. Hasin, M. A. Alpuche-Aviles, Y. Li and Y. Wu, *J. Phys. Chem. C*, 2009, **113**, 7456-7460.

85. Y. Furubayashi, T. Hitosugi, Y. Yamamoto, K. Inaba, G. Kinoda, Y. Hirose, T. Shimada and T. Hasegawa, *Appl. Phys. Lett.*, 2005, **86**.

86. A. Dawar and J. Joshi, *J. Mater. Sci.*, 1984, **19**, 1-23.

87. B. Neumann, F. Bierau, B. Johnson, C. A. Kaufmann, K. Ellmer and H. Tributsch, P*hys. Status Solidi B*, 2008, **245**, 1849-1857.

88. N. U. T. O. III-Vs Rev., 2005, 18 (**2**), 17.

89. H. Gerischer and N. Sorg, *Electrochimica Acta*, 1992, **37**, 827-835.

90. J. Nowotny, T. Bak and M. A. Alim, *ECS Solid State Lett.*, 2014, **3**, Q71-Q75.

91. L. Sheppard, A. Atanacio, T. Bak, J. Nowotny, M. Nowotny and K. Prince, *J. Solid State Electrochem.*, 2009, **13**, 1115-1121.

92. J. F. Baumard and E. Tani, *J. Chem. Phys.*, 1977, **67**, 857-860.

93. N. Yamada, T. Hitosugi, J. Kasai, N. L. H. Hoang, S. Nakao, Y. Hirose, T. Shimada and T. Hasegawa, *J. Appl. Phys.*, 2009, **105**.

94. T. Hitosugi, A. Ueda, S. Nakao, N. Yamada, Y. Furubayashi, Y. Hirose, T. Shimada and T. Hasegawa, *Appl. Phys. Lett.*, 2007, **90**.

95. S. Okazaki, J. Ohkubo, S. Nakao, Y. Hirose, T. Hitosugi and T. Hasegawa, *Jpn. J. Appl. Phys.*, 2012, **51**.

96. M. Hojo and K. Okimura, *Jpn. J. Appl. Phys.*, 2009, **48**.

97. C. M. Maghanga, J. Jensen, G. A. Niklasson, C. G. Granqvist and M. Mwamburi, *Sol. Energy Mater. Sol. Cells*, 2010, **94**, 75-79.

98. C. M. Maghanga, G. A. Niklasson and C. G. Granqvist, *Thin Solid Films*, 2009, **518**, 1254-1258.

99. D. S. Bhachu, S. Sathasivam, G. Sankar, D. O. Scanlon, G. Cibin, C. J. Carmalt, I. P. Parkin, G. W. Watson, S. M. Bawaked, A. Y. Obaid, S. Al-Thabaiti and S. N. Basahel, *Adv. Funct. Mater.*, 2014, **24**, 5075-5085.

100. T. Miyagi, M. Kamei, I. Sakaguchi, T. Mitsuhashi and A. Yamazaki, *Jpn. J. Appl. Phys.*, 2004, **43**, 775.

101. A. V. Manole, M. Dobromir, M. Girtan, R. Mallet, G. Rusu and D. Luca, *Cer. Int.*, 2013, **39**, 4771-4776.

102. Y. Horie, K. Daizaka, H. Mukae, S. Guo and T. Nomiyama, *Electrochimica Acta*, 2016, **187**, 348-357.

103. L. Jiang, T. You and W.-Q. Deng, *Nanotechnology*, 2013, **24**, 415401.

104. L. Long, L. Wu, X. Yang and X. Li, *J. Mater. Sci. Tech.*, 2014, **30**, 765-769.

105. M. Gutierrez and A. Henglein, *J. Phys. Chem.*, 1993, **97**, 11368-11370.

106. F. X. Zhang, N. J. Guan, Y. Z. Li, X. Zhang, J. X. Chen and H. S. Zeng, *Langmuir*, 2003, **19**, 8230-8234.

107. X. Bao, M. Muhler, B. Pettinger, R. Schlögl and G. Ertl, *Catal. Lett.*, 1993, **22**, 215-225.

108. J. Serafin, A. Liu and S. Seyedmonir, *J. Mol. Catal. A: Chem.*, 1998, **131**, 157-168.

109. X. He, Y. Cai, H. Zhang and C. Liang, *J. Mater. Chem.*, 2011, **21**, 475-480.

110. L. Gao, W. Gan, S. Xiao, X. Zhan and J. Li, *Cer. Int.*, 2016, **42**, 2170-2179.

111. H. Tran, J. Scott, K. Chiang and R. Amal, *J. Photochem. Photobiol. A: Chem.*, 2006, **183**, 41-52.

112. B. Sun, S.-q. Sun, T. Li and W.-q. Zhang, *J. Mater. Sci.*, 2007, **42**, 10085-10089.

113. J. G. Yu, J. F. Xiong, B. Cheng and S. W. Liu, *Appl. Catal. B-Environ.*, 2005, **60**, 211-221.

114. L. S. Daniel, H. Nagai, N. Yoshida and M. Sato, *Catalysts*, 2013, **3**, 625-645.

115. Z. Liu, N. Destouches, G. Vitrant, Y. Lefkir, T. Epicier, F. Vocanson, S. Bakhti, Y. Fang, B. Bandyopadhyay and M. Ahmed, *J. Phys. Chem. C*, 2015, **119**, 9496-9505.

116. M. Hajivaliei, *Indian J. Pure & Appl. Phys.*, 2015, **53**, 311-315.

117. S. D. Ponja, S. K. Sehmi, E. Allan, A. J. MacRobert, I. P. Parkin and C. J. Carmalt, *ACS Appl. Mater. Interfaces*, 2015, **7**, 28616-28623.

118. B. Liu and E. S. Aydil, *J. Am. Chem. Soc.*, 2009, **131**, 3985-3990.

119. J. B. Baxter and E. S. Aydil, *Appl. Phys. Lett.*, 2005, **86**, 053114.

120. C. A. Wolden, J. Kurtin, J. B. Baxter, I. Repins, S. E. Shaheen, J. T. Torvik, A. A. Rockett, V. M. Fthenakis and E. S. Aydil, *J. Vac. Sci. Techol. A*, 2011, **29**, 030801.

121. M. Abd-Lefdil, R. Diaz, H. Bihri, M. A. Aouaj and F. Rueda, *Eur. Phys. J. Appl. Phys.*, 2007, **38**, 217-219.

122. W. Baur, *Naturwissenschaften*, 1955, **42**, 295-296.

123. M. Schuisky, A. Hårsta, A. Aidla, K. Kukli, A. A. Kiisler and J. Aarik, *J. Electrochem. Soc.*, 2000, **147**, 3319-3325.

124. K. Fukushima, G. H. Takaoka and I. Yamada, *Jpn. J. Appl. Phys.*,, 1993, **32**, 3561.

125. S. Chambers, S. Thevuthasan, R. Farrow, R. Marks, J. Thiele, L. Folks, M. Samant, A. Kellock, N. Ruzycki and D. Ederer, *Appl. Phys. Lett.*, 2001, **79**, 3467-3469.

126. N. Erdman, O. Warschkow, M. Asta, K. R. Poeppelmeier, D. E. Ellis and L. D. Marks, *J. Am. Chem. Soc.*, 2003, **125**, 10050-10056.

127. R. Kennedy and P. Stampe, *J. Cryst. Growth*, 2003, **252**, 333-342.

128. L. B. Freund and S. Suresh, *Thin film materials: stress, defect formation and surface evolution*, Cambridge University Press, 2004.

129. D. M. Mattox, *Handbook of physical vapor deposition (PVD) processing*, William Andrew, 2010.

130. S. Heutz, C. Mitra, W. Wu, A. J. Fisher, A. Kerridge, M. Stoneham, A. Harker, J. Gardener, H. H. Tseng and T. S. Jones, *Adv. Mater.*, 2007, **19**, 3618-3622.

131. K. Choy, *Prog. Mater. Sci.*, 2003, **48**, 57-170.

132. R. Gordon, *J. Non-Cryst. Solids*, 1997, **218**, 81-91.

133. A. C. Jones and M. L. Hitchman, *Chemical vapour deposition: precursors, processes and applications*, Royal Society of Chemistry, 2009.

134. Y. Xu and X.-T. Yan, *Chemical Vapour Deposition: An Integrated Engineering Design for Advanced Materials*, 2010, 1-28.

135. H. O. Pierson, *Handbook of chemical vapor deposition: principles, technology and applications*, William Andrew, 1999.

136. T. P. Niesen and M. R. De Guire, *J. Electroceram.*, 2001, **6**, 169-207.

137. W. A. Roehm and E. A. Rogge, *Doctor blade and mounting for rotogravure printing machines,* 1955

138. C. J. Brinker and G. W. Scherer, *Sol-gel science: the physics and chemistry of sol-gel processing*, Academic press, 2013.

139. P. Nair, M. Nair, V. Garcıa, O. Arenas, Y. Pena, A. Castillo, I. Ayala, O. Gomezdaza, A. Sanchez and J. Campos, *Sol. Energ. Mater. Sol. Cells*, 1998, **52**, 313-344.

140. D. Gutiérrez-Tauste, X. Domènech, M. A. Hernández-Fenollosa and J. A. Ayllón, *J. Mater. Chem.*, 2006, **16**, 2249-2255.

141. H. Nagayama, H. Honda and H. Kawahara, *J. Electrochem. Soc.*, 1988, **135**, 2013-2016.

142. K. Wasa, M. Kitabatake and H. Adachi, *Thin film materials technology: sputtering of control compound materials*, Springer Science & Business Media, 2004.

143. E. Bauer and J. H. van der Merwe, *Phys. Rev. B*, 1986, **33**, 3657.

144. J. A. Floro, E. Chason, R. C. Cammarata and D. J. Srolovitz, *MRS bulletin*, 2002, **27**, 19-25.

145. Y.-W. Mo, D. Savage, B. Swartzentruber and M. G. Lagally, *Phys. Rev. Lett.*, 1990, **65**, 1020.

146. K. Byrappa and M. Yoshimura, *Handbook of hydrothermal technology*, William Andrew, 2012.

147. R. I. Walton, *Chem. Soc. Rev.*, 2002, **31**, 230-238.

148. K. Byrappa and T. Adschiri, *Prog. Cryst. Growth Charact. Mater.*, 2007, **53**, 117-166.

149. A. A. Peterson, F. Vogel, R. P. Lachance, M. Fröling, M. J. Antal Jr and J. W. Tester, *Energy & Environmental Science*, 2008, **1**, 32-65.

150. W. L. Suchanek and R. E. Riman, *Adv. Sci. Technol.* 2006, **3**, 184-193.

151. A. Rabenau, *Ang. Chem. Int. Ed. Eng.*, 1985, **24**, 1026-1040.

152. Parr Instrument Company, www.parrinst.com/products/non-stirred-pressure-vessels/.

153. Savillex Corporation, www.savillex.com.

154. M.-A. Einarsrud and T. Grande, *Chem. Soc. Rev.*, 2014, **43**, 2187-2199.

155. A. Reksten, *Hydrothermal Synthesis of $LaFeO_2$,* 2011.

156. S. Calvin, *XAFS for Everyone*, CRC Press, 2013.

157. M. Newville, *Rev. Mineralogy and Geochemistry*, 2014, **78**, 33-74.

158. G. Bunker, *Introduction to XAFS: a practical guide to X-ray absorption fine structure spectroscopy*, Cambridge University Press, 2010.

159. M. R. Antonio, I. Song and H. Yamada, *J. Solid State Chem.*, 1991, **93**, 183-192.

160. P. Viparelli, P. Ciambelli, J.-C. Volta and J.-M. Herrmann, *Appl. Catal. A: General*, 1999, **182**, 165-173.

161. A. Kafizas and I. P. Parkin, *J. Mater. Chem.*, 2010, **20**, 2157-2169.

162. M. Fehse, S. Cavaliere, P. E. Lippens, I. Savych, A. Iadecola, L. Monconduit, D. J. Jones, J. Roziere, F. Fischer, C. Tessier and L. Stievanot, *J. Phys. Chem. C*, 2013, **117**, 13827-13835.

163. T. D. Manning, I. P. Parkin, C. Blackman and U. Qureshi, *J. Mater. Chem.*, 2005, **15**, 4560-4566.

164. L. Sheppard, T. Bak, J. Nowotny, C. Sorrell, S. Kumar, A. Gerson, M. Barnes and C. Ball, *Thin Solid Films*, 2006, **510**, 119-124.

165. L. De Trizio, R. Buonsanti, A. M. Schimpf, A. Llordes, D. R. Gamelin, R. Simonutti and D. J. Milliron, *Chem. Mater.*, 2013, **25**, 3383-3390.

166. S. A. O'Neill, I. P. Parkin, R. J. Clark, A. Mills and N. Elliott, *J. Mater. Chem.*, 2003, **13**, 2952-2956.

167. W. E. Slink and P. B. DeGroot, *J. Catal.*, 1981, **68**, 423-432.

168. M. Horn, C. Schwebdtfeger and E. Meagher, *Z. Kristallogr. -Crystal. Mater.*, 1972, **136**, 273-281.

169. T. Ercit, *Mineralogy and Petrology*, 1991, **43**, 217-223.

170. B. N. Joshi, H. Yoon, M. F. A. M. van Hest and S. S. Yoon, *J. Am. Cer. Soc.*, 2013, **96**, 2623-2627.

171. R. Bouchet, A. Weibel, P. Knauth, G. Mountjoy and A. V. Chadwick, *Chem. Mater.*, 2003, **15**, 4996-5002.

172. R. Swanepoel, *J. Phys. E: Sci. Instr.*, 1983, **16**, 1214

.

173. M. Hirano and Y. Ichihashi, *J. Mater. Sci.*, 2009, **44**, 6135-6143.

174. J. Biedrzycki, S. Livraghi, E. Giamello, S. Agnoli and G. Granozzi, *J. Phys. Chem. C*, 2014, **118**, 8462-8473.

175. Y. Liu, J. M. Szeifert, J. M. Feckl, B. Mandlmeier, J. Rathousky, O. Hayden, D. Fattakhova-Rohlfing and T. Bein, *ACS Nano*, 2010, **4**, 5373-5381.

176. D. J. Norris, A. L. Efros and S. C. Erwin, *Science*, 2008, **319**, 1776-1779.

177. J. Arbiol, J. Cerda, G. Dezanneau, A. Cirera, F. Peiro, A. Cornet and J. R. Morante, *J. Appl. Phys.*, 2002, **92**, 853-861.

178. A. Kafizas, N. Noor, P. Carmichael, D. O. Scanlon, C. J. Carmalt and I. P. Parkin, *Adv. Funct. Mater.*, 2014, **24**, 1758-1771.

179. H. Kamisaka, T. Hitosugi, T. Suenaga, T. Hasegawa and K. Yamashita, *J. Chem. Phys.*, 2009, **131**, 034702.

180. X. Lue, X. Mou, J. Wu, D. Zhang, L. Zhang, F. Huang, F. Xu and S. Huang, *Adv. Funct. Mater.*, 2010, **20**, 509-515.

181. A. Zaleska, *Recent Patents on Engineering*, 2008, **2**, 157-164.

182. K.-C. Ok, Y. Park, K.-B. Chung and J.-S. Park, *J. Phys. D: Appl. Phys.*, 2013, **46**, 295102.

183. E. Burstein, *Phys. Rev.*, 1954, **93**, 632.

184. T. Moss, *Proc. Phys. Soc. B*, 1954, **67**, 775.

185. M. Sacerdoti, M. C. Dalconi, M. C. Carotta, B. Cavicchi, M. Ferroni, S. Colonna and M. L. Di Vona, *J. Solid State Chem.*, 2004, **177**, 1781-1788.

186. A. Froideval, C. Degueldre, C. U. Segre, M. A. Pouchon and D. Grolimund, *Corrosion Sci.*, 2008, **50**, 1313-1320.

187. C. Edusi, G. Hyett, G. Sankar and I. P. Parkin, *Chem. Vap. Dep.*, 2011, **17**, 30-36.

188. C. Edusi, G. Sankar and I. P. Parkin, *Chem. Vap. Dep.*, 2012, **18**, 126-132.

189. A. Mills, A. Lepre, N. Elliott, S. Bhopal, I. P. Parkin and S. A. O'Neill, *J. Photochem. Photobiol. A-Chem.*, 2003, **160**, 213-224.

190. S. Ponja, S. Sathasivam, N. Chadwick, A. Kafizas, S. M. Bawaked, A. Y. Obaid, S. Al-Thabaiti, S. N. Basahel, I. P. Parkin and C. J. Carmalt, *J. Mater. Chem. A*, 2013, **1**, 6271-6278.

191. V. Palenskis, *World J. Condensed Matter Phys.*, 2013, **3**, 73.

192. R. O. Ansell, T. Dickinson, A. F. Povey and P. M. A. Sherwood, *J. Electrochem. Soc.*, 1977, **124**, 1360-1364.

193. E. Magni and G. Somorjai, *J. Phys. Chem.*, 1996, **100**, 14786-14793.

194. S. P. Vanka, G. Luo and N. G. Glumac, *J. Crystal Growth*, 2004, **267**, 22-34.

195. S. Sathasivam, A. Kafizas, S. Ponja, N. Chadwick, D. S. Bhachu, S. M. Bawaked, A. Y. Obaid, S. Al-Thabaiti, S. N. Basahel and C. J. Carmalt, *Chem. Vap. Dep.*, 2014, **20**, 69-79.

196. N. Chadwick, S. Sathasivam, A. Kafizas, S. M. Bawaked, A. Y. Obaid, S. Al-Thabaiti, S. N. Basahel, I. P. Parkin and C. J. Carmalt, *J. Mater. Chem. A*, 2014, **2**, 5108-5116.

197. W. Choi, H. Sung, K. Kim, J. Cho, S. Choi, H.-J. Jung, S. Koh, C. Lee and K. Jeong, *J. Mater. Sci. Lett.*, 1997, **16**, 1551-1554.

198. Y. Li-Zi, S. Zhi-Tong and W. Chan-Zheng, *J. Solid State Chem.*, 1994, **113**, 221-224.

199. K. Von Rottkay and M. Rubin, *MRS Proceedings* 449, Cambridge Univ. Press, 1996.

200. T. Yamaki, T. Sumita and S. Yamamoto, *J. Mater. Sci. Lett.*, 2002, **21**, 33-35.

201. C. Powell and A. Jablonski, *Nucl. Instrum. Methods in Phys. Res. A: Accelerators, Spectrometers, Detectors and Associated Equipment*, 2009, **601**, 54-65.

202. J. F. Watts and J. Wolstenholme, *An Introduction to Surface Analysis by XPS and AES,* Wiley-VCH, 2003, 224.

203. C. Rhodes, S. Franzen, J.-P. Maria, M. Losego, D. N. Leonard, B. Laughlin, G. Duscher and S. Weibel, *J. Appl. Phys.*, 2006, **100**, 054905.

204. A. J. Gardecka, G. K. L. Goh, G. Sankar and I. P. Parkin, *J. Mater. Chem. A*, 2015, **3**, 17755-17762.

205. S. X. Zhang, D. C. Kundaliya, W. Yu, S. Dhar, S. Y. Young, L. G. Salamanca-Riba, S. B. Ogale, R. D. Vispute and T. Venkatesan, *J. Appl. Phys.*, 2007, **102**.

206. Z. Yuan, N. H. Dryden, J. J. Vittal and R. J. Puddephatt, *Chem. Mater.*, 1995, **7**, 1696-1702.

207. C. W. Dunnill, K. Page, Z. A. Aiken, S. Noimark, G. Hyett, A. Kafizas, J. Pratten, M. Wilson and I. P. Parkin, *J. Photochem. Photobiol. A: Chem.*, 2011, **220**, 113-123.

208. Y. Lu, G. L. Liu and L. P. Lee, *Nano letters*, 2005, **5**, 5-9.

209. R. Olesinski, A. Gokhale and G. Abbaschian, *J. Phase Equilib.*, 1989, **10**, 635-640.

210. L. Weber, *Metall. Mater. Trans. A*, 2002, **33**, 1145-1150.

211. D. K. Burge, H. E. Bennett and E. J. Ashley, *Appl. Opt.*, 1973, **12**, 42-47.

212. J. Szczyrbowski, G. Bräuer, M. Ruske, H. Schilling and A. Zmelty, *Thin Solid Films*, 1999, **351**, 254-259.

213. X. Hu, C. Hu and J. Qu, *Materials Research Bulletin*, 2008, **43**, 2986-2997.

214. M. Romand, M. Roubin and J.-P. Deloume, *Journal of Solid State Chem.*, 1978, **25**, 59-64.

215. N. Özer, M. D. Rubin and C. M. Lampert, *Sol. Energ. Mater. Sol. Cells*, 1996, **40**, 285-296.

216. R. Nainani, P. Thakur and M. Chaskar, *J. Mater. Sci. Eng. B*, 2012, **2**, 52-58.

217. B. Wen, C. Liu and Y. Liu, *Inorg. Chem.*, 2005, **44**, 6503-6505.

218. D. Sarkar, C. K. Ghosh, S. Mukherjee and K. K. Chattopadhyay, *ACS Appl. Mater. Interfaces*, 2012, **5**, 331-337.

219. W. Zhou, H. Liu, J. Wang, D. Liu, G. Du and J. Cui, *ACS Appl. Mater. Interfaces*, 2010, **2**, 2385-2392.

220. W. Zhou, H. Liu, J. Wang, D. Liu, G. Du, S. Han, J. Lin and R. Wang, *Phys. Chem. Chem. Phys.*, 2010, **12**, 15119-15123.

221. X. Wang, S. Li, H. Yu, J. Yu and S. Liu, *Chem.–A Eur. J.*, 2011, **17**, 7777-7780.

222. C. Wang, E. Yifeng, L. Fan, S. Yang and Y. Li, *J. Mater. Chem.*, 2009, **19**, 3841-3846.

223. V. Subramanian, E. E. Wolf and P. V. Kamat, *J. Am. Chem. Soc.*, 2004, **126**, 4943-4950.

224. M. Jakob, H. Levanon and P. V. Kamat, *Nano Letters*, 2003, **3**, 353-358.

225. S. Banerjee, S. K. Mohapatra, P. P. Das and M. Misra, *Chem. Mater.*, 2008, **20**, 6784-6791.

226. G. Munuera, A. R. Gonzalezelipe, J. P. Espinos and E. Lopezmolina, *Surf. Interface Anal.*, 1990, **15**, 693-697.

227. D. Simon, C. Perrin and P. Baillif, *Electron spectrometry study (ESCA) of niobium and its oxides. Application to the oxidation at high temperature and low oxygen pressure,* Orleans Univ., 1976.

228. C. M. Chan, S. Trigwell and T. Duerig, *Surf. Interface Anal.*, 1990, **15**, 349-354.

229. M. Bahl, *J. Phys. Chem. Solids*, 1975, **36**, 485-491.

230. K.-W. Cheng, Y.-T. Lin, C.-Y. Chen, C.-P. Hsiung, J.-Y. Gan, J.-W. Yeh, C.-H. Hsieh and L.-J. Chou, *Appl. Phys. Lett.*, 2004, **88**.

231. M. Wu, G. Lin, D. Chen, G. Wang, D. He, S. Feng and R. Xu, *Chem. Mater.*, 2002, **14**, 1974-1980.

232. H. Cheng, J. Ma, Z. Zhao and L. Qi, *Chem. Mater.*, 1995, **7**, 663-671.

233. S. D. Burnside, V. Shklover, C. Barbé, P. Comte, F. Arendse, K. Brooks and M. Grätzel, *Chem. Mater.*, 1998, **10**, 2419-2425.

234. P. D. Cozzoli, A. Kornowski and H. Weller, *J. Am. Chem. Soc.*, 2003, **125**, 14539-14548.

235. A. Pottier, C. Chanéac, E. Tronc, L. Mazerolles and J.-P. Jolivet, *J. Mater. Chem.*, 2001, **11**, 1116-1121.

236. J.-P. Jolivet, M. Henry and J. Livage, *Metal oxide chemistry and synthesis: from solution to solid state*, Wiley-Blackwell, 2000.

237. R. K. Sharma and M. Bhatnagar, *Sensors and Actuators B: Chemical*, 1999, **56**, 215-219.

238. H. Usui, S. Yoshioka, K. Wasada, M. Shimizu and H. Sakaguchi, *ACS Appl. Mater. Interfaces*, 2015, **7**, 6567-6573.

239. A. M. Ruiz, G. Dezanneau, J. Arbiol, A. Cornet and J. R. Morante, *Chem. Mater.*, 2004, **16**, 862-871.

240. V. Guidi, M. Carotta, M. Ferroni, G. Martinelli and M. Sacerdoti, *J. Phys. Chem. B*, 2003, **107**, 120-124.

241. P. W. Voorhees, *J. Stat. Phys.*, 1985, **38**, 231-252.

242. H. G. Yang and H. C. Zeng, *J. Phys. Chem. B*, 2004, **108**, 3492-3495.

243. H. A. Huy, B. Aradi, T. Frauenheim and P. Deák, *J. Appl. Phys.*, 2012, **112**, 016103.

244. L. Yan, K. Huang, Y. Chen and Y. Xing, *ECS Electrochemistry Letters*, 2014, **3**, F27-F29.

245. S.-Y. Huang, P. Ganesan and B. N. Popov, *Appl. Catal. B: Env.*, 2010, **96**, 224-231.

246. A. J. Atanacio, T. Bak and J. Nowotny, *J. Phys. Chem. C*, 2014, **118**, 11174-11185.

247. M. Fallah, M.-R. Zamani-Meymian, R. Rahimi and M. Rabbanib, *Appl. Surf. Sci.*, 2014, **316**, 456-462.

248. M. C. Carotta, M. Ferroni, D. Gnani, V. Guidi, M. Merli, G. Martinelli, M. C. Casale and M. Notaro, *Sensors and Actuators B-Chemical*, 1999, **58**, 310-317.

249. K. Ding, Z. Miao, B. Hu, G. An, Z. Sun, B. Han and Z. Liu, *Langmuir*, 2010, **26**, 10294-10302.

250. M.-K. Lee, C.-M. Shih, S.-C. Fang, H.-F. Tu and C.-L. Ho, *Jpn J. Appl. Phys.*, 2007, **46**, 1653.

251. J. Baumard and E. Tani, P*hys. Status Solidi (a)*, 1977, **39**, 373-382.

252. X. Feng, *Nanocarbons for Advanced Energy Storage*, John Wiley & Sons, 2015.

253. L. Yongfeng, L. Yanzhen, Y. Yonggang, W. Yuefang and W. Maozhang, *J. Nanosci. Nanotechnol.*, 2012, **12**, 3066-3069.

254. J. J. Shao, W. Lv and Q. H. Yang, *Adv. Mater.*, 2014, **26**, 5586-5612.

255. J. Forrest, K. Dalnoki-Veress, J. Stevens and J. Dutcher, *Phys. Rev. Lett.*, 1996, **77**, 2002.

256. E. Kim, Y. N. Xia and G. M. Whitesides, *Nature*, 1995, **376**, 581-584.

257. V. Y. Prinz, V. Seleznev, A. Gutakovsky, A. Chehovskiy, V. Preobrazhenskii, M. Putyato and T. Gavrilova, *Physica E: Low-dimensional Systems and Nanostructures*, 2000, **6**, 828-831.

258. H. Yang, N. Coombs, I. Sokolov and G. A. Ozin, *Nature*, 1996, **381**, 589-592.

259. J. Shen, Y. Hu, C. Li, C. Qin and M. Ye, *Small*, 2009, **5**, 82-85.

260. X. Qi, K. Y. Pu, H. Li, X. Zhou, S. Wu, Q. L. Fan, B. Liu, F. Boey, W. Huang and H. Zhang, *Angew. Chem. Int. Ed.*, 2010, **49**, 9426-9429.

261. Z. Hong, M. Wei, T. Lan and G. Cao, *Nano Energy*, 2012, **1**, 466-471.

262. H. Cölfen and M. Antonietti, *Angew. Chem. Int. Ed.*, 2005, **44**, 5576-5591.

263. K. Lv, H. Zuo, J. Sun, K. Deng, S. Liu, X. Li and D. Wang, *J. Hazard. Mater.*, 2009, **161**, 396-401.

264. Z. Liu, Z. Jian, J. Fang, X. Xu, X. Zhu and S. Wu, *Int. J. Photoenergy*, 2012, DOI: 10.1155/2012/702503.

265. M. Ivanda, S. Music, S. Popovic and M. Gotic, *J. Mol. Struct.*, 1999, **481**, 645-649.

266. T. Bezrodna, T. Gavrilko, G. Puchkovska, V. Shimanovska, J. Baran and M. Marchewka, *J. Mol. Struct.*, 2002, **614**, 315-324.